Microwave near-field probes to detect electrically small particles

by

Zhao Ren

A thesis
presented to the University of Waterloo
in fulfillment of the
thesis requirement for the degree of
Doctor of Philosophy
in
Electrical and Computer Engineering

Waterloo, Ontario, Canada, 2013

I hereby declare that I am the sole author of this thesis. This is a true copy of the thesis, including any required final revisions, as accepted by my examiners.

I understand that my thesis may be made electronically available to the public.

Abstract

Microwave near-field probes (MNPs) confine evanescent fields to regions that are substantially smaller than the wavelength at the operation frequency. Such probes are able to resolve subwavelength features, thus providing resolution much higher than the classical Abb limit. These abilities of MNPs are primarily due to the evanescent nature of the field generated at the tip of the probes. In the past, MNPs with ultra-high resolution were designed by tapering a resonant opening to provide high field concentration and high sensitivity. The limitations of these MNPs were subject to low surface roughness and practical realization challenges due to their geometrical features and vibration control constraints.

Metamaterials with their ability to enhance evanescent fields, lead to the speculation that they could potentially increase the sensitivity of near-field probe. Periodically arranged metamaterial unit elements such as split-ring-resonators (SRRs) can create negative permeability media. Placing such material layer in the proximity of a probe leads to enhancement of the evanescent waves. Guided by this remarkable feature of metamaterials, I proposed an MNP consisting of a wire loop concentric with a single SRR. The evanescent field behavior of the probe is analyzed using Fourier analysis revealing substantial enhancement of the evanescent field consistent with metamaterial theory predictions. The resolution of the probe is studied to especially determine its ability for sub-surface detection of media buried in biological tissues. The underlying physics governing the probe is analyzed. Variations of the probe are developed by placement of lumped impedance loads.

To further increase the field confinement to smaller region, a miniaturized probe design is proposed. This new probe consists of two printed loops whose resonance is tunable by a capacitor loaded in the inner loop. The sensing region is decreased from $\lambda/20$ to $\lambda/55$, where λ is the wavelength of the probes unloaded frequency.

The magnetic-sensitive nature of the new probe makes it suitable for sensing localized magnetostatic surface resonance (LMSR) occurring in electrically very small particles.

Therefore, I proposed a sensing methodology for detecting localized magnetostatic surface (LMS) resonant particles. In this methodology, an LMS resonant sphere is placed concentrically with the loops. A circuit model is developed to predict the performance of the probe in the presence of a magnetic sphere having Lorentz dispersion. Full-wave simulations are carried out to verify the circuit model predictions, and preliminary experimental results are demonstrated. The Lorentzian fit in this work implies that the physical nature of LMSR may originate from spin movement of charged particle whose contribution to effective permeability may be analogous to that of bound electron movement to effective permittivity in electrostatic resonance. Detection of LMSR can have strong impact on marker-based sensing applications in biomedicine and bioengineering.

Acknowledgements

I would like to express my deepest and utmost gratitude to my supervisor Dr. Omar M. Ramahi. He is a true human being with love deepness, a true scientist with innate scientific intuition, a true warrior with fearlessness toward science. I still remember the first day I knocked his door asking for a position in his group, as I was totally defeated for my first year life in Canada. His rapport and encouragement toward a stranger (me) completely got me, and I felt so glad that he could consider me as a potential candidate in his group. Throughout my Ph.D. life, his scientific instinct sowed invisible seeds in my mind, which have been nurtured with his unflinching patience and courage. Until the last year of my Ph.D., the hibernated seeds turned into a bud. At that moment, I realized how much he has expected from me as a researcher, a future scientist, more importantly as a young mother, a human being, and how much he expected from me to find the truly me inside, not for others, but for myself. From that moment on, I reborn, and everything else in my life reborn. He stroke my sleeping heart and shed the light in front of me. He taught me to break the chain of perfectionism. He taught me to take the lead not to follow. His philosophy towards science and life ignites me to think deeper, deeper, and deeper... I owe a mountain of gratefulness for his forgiveness and boundless love toward my mistakes, naiveness, and troubles. My truly thank to him will last forever in the bottom of my heart as a precious treasure lightens my future path.

I express my sincere appreciation to my committee member Prof. Safavi-Naeini for his peerless discussion and generosity in sharing his deep knowledge with me after the defense. His frankness and unlimited rapports nourished my mind and intrigued a garden of thoughts.

I convey my special acknowledgement to my committee member Prof. Simarjeet Saini for his invaluable feedbacks on my experimental research in my defense.

I would like to take this opportunity to thank my committee member Prof. Joseph

Sanderson for serving my Ph.D. committee. Every conversation with him was such a pleasant experience. His endless gracefulness and thoughtfulness always warm me.

I convey my unparalleled honor and gratitude to Professor Federico Capasso for serving my external committee examiner. I was so deeply touched by his beautiful mind and unbelievable humbleness. I was wordless in front of him, however, it would be the most memorable moment in my life!

I would like to deliver my special thanks to my previous supervisor Professor Kostadinka Bizheva for offering me a chance to begin my study in University of Waterloo. Her guidance in my English and presentation skills are always beneficial to my academic performance.

I would like to give my sincere gratitude to my previous colleague Dr. Ali Kabiri. He is the most inspiring mentor who always give unlimited encouragement. He is an admirable young scientist.

Many special thanks to my previous colleague Dr. Muhammed S. Boybay. I am much indebt to him for his coaching and ideas given in early years of my Ph.D.. His modesty and thoughtfulness will always be an example for me throughout my life.

My sincere acknowledgement to my previous group member Babak Alavikia, Leila Yousefi, Mohammed Bait Suwailam, Nael Suwan, Hussein Attia, and Bing Hu, who brought the warmest memories of my Ph.D. times as a family. My sincere individual thanks to my current colleagues, Thamer Almoneef, Khawla Alzoubi, Ahmed Ashoor, Vahid Nayyeri, Abdulbaset Ali, Mohammed AlShareef, Ali Albishi, Miguel Ruphuy, Humayra Naosaba, and Abdulaziz Alqahtani for friendly discussions and inspiring conversations that always drive me to think and learn.

My heartful thanks to my dear parents, I own a mountain of gratitude to them for their vast love and unwavering support in my Ph.D. study. They taught me the goodness of life and the basics of being as a person. They always lead me to become better as a person, a

wife, a mother, a daughter, and a friend. I thank them more that I could give to. Their endless love shines upon me wherever I go, and whatever I am going to be.

Wordless thanks to my husband Xiaojian for his unfailing love in my life from the first day we met to the hardest time we had. Every moment, even the bitterness, tastes like honey. He is the warmest harbor and shelter when I feel insecure and hopeless. He is my beloved husband, loyal friend, and soul mate.

My tender thanks goes to my angel daughter Fiona. She always brings the most joyful moment at home and turns my most depressed times into colorful world. Her marvelous independence at the age of two compels me to be stronger and stronger as a mother. I feel so blessed I could meet her in this world. Being her mother is such a proud.

I would like to take this chance to thank my manager Steve Carr at Engineering Computing Help Desk for guaranteeing me a part-time position for almost three years, providing me extra financial support for my student life. His kindness and helpfulness in my work always encourage me to explore more outside my academic life. Also special thanks to my help desk co-workers, Ahmed and Fei Chen for their limitless encourage for my Ph.D. work, also Ryan and Ahdam for their unselfish supports in the shifts.

Last but not the least, I thank the omnipresent Lord: I believe you are watching us and making every people a better person. You provide endless love to this world. I never feel so close to you, my Lord...

Z. R.

Dedication

This is dedicated to the one I love.

Table of Contents

List of Figures

List of Abbreviations

MNP	Microwave Near-field Probe
LMS	Localized Magnetostatic Surface
LMSR	Localized Magnetostatic Surface Resonance
SRR	Split Ring Resonator
EM	Electromagnetic
LHM	Left-handed Materials
DNG	Double Negative
SNG	Single Negative
ENG	ϵ-negative
ENZ	ϵ-near-zero
PCB	Printed Circuit Board
FMR	Ferromagnetic resonance/Ferrimagnetic Resonance
FM	Ferromagnetic/Ferrimagnetic
PVC	Polyvinyl Chloride
PLD	Power Loss Density
SQUID	Superconducting Quantum Interference Device
YIG	Yttrium Iron Garnet
CVG	Polycrystalline calcium-vanadium substituted YIG

GG Gadolium Substituted Garnet

Chapter 1

Introduction

1.1 Evolution of microwave near-field probes (MNPs)

The origin of near-field probing concept probably dates back to 1928 when Synge first described his near-field imaging idea with a microscopic method in a letter to Albert Einstein. His original idea was to use the scattered field (dark field) of an object (i.e., a particle) as a light source to go beyond the diffraction limit. As suggested by Einstein, Synge published his idea with a more practical but abstract experimentation that used an opaque screen with a sub-wavelength hole placed very close to a flat transparent sample. The image was obtained by scanning the sample point-by-point, producing higher resolution image. The scanning principle has become an important constituent in many modern technologies, such as television and scanning electron microscopy [1]. The scattered field near the aperture or a small particle was essentially evanescent waves having high-spacial frequency (wavenumber = $2\pi/\lambda$), leading to sub-wavelength resolution [2].

Synge's idea was decades ahead of its time before the required technology for his instrumentation could come out [1, 2]. In 1957 [3], Frait proposed an apparatus that was in fact

a microwave microscope to study ferromagnetic resonance. He modified the conventional ferromagnetic resonant cavity that averages over the sample properties in it by placing the sample outside of cavity but very closed to a small hole created in a thin face of the cavity (Fig. 1.1(a)) [2]. In this way, higher wavelength components would be applied on to the sample rather than all wavelengths. In 1962, independent work and similar apparatus composition (a microwave cavity with a small opening) was developed by Soohoo [4]. Frait and Soohoo's work were considered as the first experimental realization of near-field imaging in the microwave regime as the dimensional requirements of probe size and probe-sample distance were less rigorous in comparison to those at optical frequencies [4, 5].

The non-resonant approach in microwave microscope started in 1965 by Bryant and Gunn who employed a tapered coaxial line (Fig. 1.1(b)) to measure the local resistivity of semiconductor crystals from 0.1-100$\Omega \cdot cm$ [2, 5, 6]. Their work was the first time that near-field probe-sample interactions was represented in terms of resistivity measurement within a hemisphere of $1mm$ radius [6]. In 1972, Ash and Nochols proposed another resonant approach microscope composed of a hemisphere resonator with a small aperture at the flat end. Their microwave microscope was able to resolve a grating with line width of $\lambda/60$ at around $10GHz$ [7]. Ash and Nochols' invention was the first to demonstrate deep subwavelength resolution, and regarded as the most profound contribution to development of near-field instruments [5]. In 1989, Fee *et al.* proposed another non-resonant microwave microscope that measured the reflected signal from an open ended coaxial line (Fig. 1.1(c)) [8]. This MNP was able to detect subwavelength features of $\lambda/4000$ at around 2.5GHz. Their extended proposal of sharpened tip at the end of the transmission line influenced later works in micro-structure detection.

In late 1990s, the resonant concept and sharpened end approach began to merge (Fig. 1.1(d)), leading to the significant advancement of high resolution MNPs. In 1996, Wei *et al.* proposed a resonant scanning tip microwave near-field microscope that demonstrated high field concentration and strong energy delivery at the sharpened tip. The tip was

enclosed by the electric shielding that suppressed signal to noise ratio, yielding a spatial resolution of $\lambda/10^5$ [9]. In 1997, Gao *et al.* improved the imaging technique to quantitative impedance mapping under a quasi-static theoretical model. Their technique produced enhanced resolution up to $\lambda/10^6$, leading to a new imaging paradigm [10] (Up to now, this is still the highest resolution reported in the literature for MNPs.). In 1999, Tabib-Azar *et al.* employed a resonant microscope line ended with a tapered tip at $1GHz$, and attained a spatial resolution of $\lambda/750000$ in sensing a microelectromechanic chip [11]. In 1999, they also imaged the biological sample in terms of a conductivity map using the same microscope [12]. Sensing other materials, such as semiconductors, dielectrics, composites and plants were investigated as well [13].

An important issue in microwave near-field sensing is the variation in probe-sample (or standoff) distance. Such disturbance was found to induce topographical scanning artifacts [1], which has been addressed in many MNP works associated with near-field imaging [5]. Thus, probe-sample distance in nanometer range and advanced vibration control in critical for high resolution near-field probes. In this work, the affect of standoff distance to probe reflection coefficient is not the most significant obstacle. Methods to reduce the affect of the standoff distance will be introduced in Chapter 2.

Regardless of the above illustrious landmarks in the evolution of ultra-high resolution MNPs, it was noticed that these high performance MNPs require low surface roughness and excellent vibration control to maintain the reported capabilities. There also exist a variety of other MNP designs to accommodate these practical realization challenges with some compromise in resolution. These applications are often found in industrial or engineering research where durability, reliability and reproductivity are of concern. For instance, flangeless open-ended coaxial waveguide theory was fully developed after Bryant and Gunn's experiment [14, 15]. Moreover, open-ended waveguide, tapered waveguide, dielectric slab loaded waveguide, or dielectric waveguide was thoroughly investigated in Ghasr's work in 2005 [16] and further developed to a standing alone system as a differential probe in

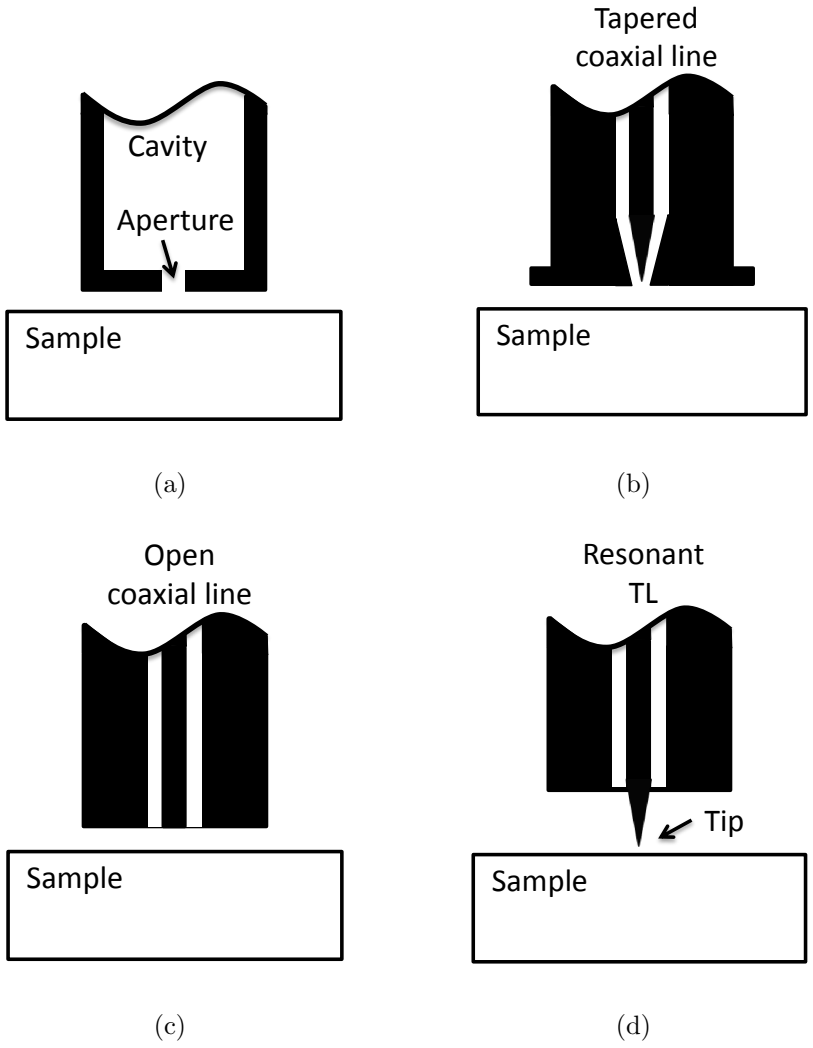

Figure 1.1: Some typical designs of MNPs. (a) Cavity terminated with aperture; (b) Tapered coaxial line; (c) Open ended coaxial line; (d) Resonant transmission line ended with a small tip.

2006 [17].

1.2 State of the Art

1.2.1 Metamaterials

In the dawn of this century, Sir John Pendry challenged the traditional limitations of lens performance with a class of superlenses having negative refractive index [18]. His idea of negative permittivity and/or permeability materials engrossed innumerable minds and lead to a tide of metamaterial research, such as super resolution imaging [18–20], cloaking [21,22], optical circuits [23], magnetic plasmons [24], amongst others. These ideas were fundamentally based on tailoring the values of electromagnetic (EM) constitutive parameters (permittivity and permeability) to guide EM waves into extraordinary behaviors in all frequency scenarios where Maxwell equation governs.

In fact, the ignition point of metamaterial tide occurred at a much earlier time through very thorough theoretical work by the notable physicist, Veselago. In 1968 [25], he first proposed the selection of the negative sign of permittivity and permeability, forming the left-handed materials (LHMs) where the wavevector, electric field, and magnetic field obey left-handed rules. Several evolutionary effects in LHMs were proposed in Veselago's work. He expounded that phase velocity is opposite to energy flux direction, meaning that energy moves forward as phase travels backward. He also elaborated the wave propagation from ordinary media to LHMs using Snell's Law, reaching several conclusions on wave propagation in a flat slab, a convex lens and a concave lens made of LHMs. The flat slab (named as Veselago's lens) is being well-known after Pendry's proposal of perfect lens in 2000 [18].

Veselago and Pendry's ideas lead to speculations on classical definition of the constitutive parameters of an isotropic medium. These parameters are referred to as complex

permittivity ($\epsilon = \epsilon_0\epsilon_r$) and complex permeability ($\mu = \mu_0\mu_r$), where ϵ_0 and μ_0 are values in vacuum, and ϵ_r and μ_r are relative quantities. ϵ and μ are measures of material reacting to electric or magnetic field, and their total reaction to EM field is represented by complex refractive index, n, described as

$$n = n' - jn'' \tag{1.1}$$

where $'$ represents real part of n that contributes to the propagation and defines speed of EM waves ($c = 1/n'$), and $''$ represents imaginary part of n that reflects the absorption loss of the material. In complex domain, n is represented by complex operator $(*)^{\frac{1}{2}}$ as follows

$$n = (\epsilon\mu)^{\frac{1}{2}} \tag{1.2}$$

where

$$\epsilon = \epsilon' - j\epsilon'' = r_\epsilon e^{j\theta_\epsilon} \tag{1.3}$$

$$\mu = \mu' - j\mu'' = r_\mu e^{j\theta_\mu} \tag{1.4}$$

n can be expanded as ϵ and μ in the following forms

$$n = (r_\epsilon r_\mu)^{\frac{1}{2}} e^{j\frac{\theta_\mu + \theta_\epsilon}{2}} \tag{1.5}$$

where r and θ correspond to the magnitude and phase, and their subscripts are referred to ϵ and μ. The real parts, ϵ' and μ' indicate electric or magnetic propagation. Their signs are subject to no physical restriction ($\omega \neq 0$). The imaginary parts, ϵ'' and μ'', reflect electric or magnetic loss that are positive values [26]. Take the simplest case as an example, in a lossless isotropic left-handed medium, $\epsilon'' = \mu'' = 0$, and $\epsilon' = \mu' = -1$, according to Eq. 1.3 and Eq. 1.4, $\theta_\epsilon = \theta_\mu = 180°$. It is natural to draw the conclusion from Eq. 1.5 that $n = 1e^{j\pi} = -1$. This means that one does not need to select the sign of n in LHM, which was misunderstood in the very early work on metamaterials [18], but was later re-evaluated [27]. As previously mentioned, due to negativeness in real refractive index, the resulting phase velocity ($v_p = \omega/\beta$, where ω is angular frequency, and $\beta = Im(j\omega\sqrt{\epsilon\mu})$, is propagation constant) and group velocity ($v_g = d\omega/d\beta$) are both negative [25, 28].

The existence of negative ϵ' and negative μ' validates energy conservation. In a passive medium, energy conservation validates as follows [25, 26, 28].

$$W = \frac{\partial(\epsilon\omega)}{\partial\omega}|E|^2 + \frac{\partial(\mu\omega)}{\partial\omega}|H|^2 > 0 \tag{1.6}$$

where $|*|$ represent magnitude quantity, and $\partial(*)/\partial\omega$ is partial derivative with respect to ω. The law of energy conservation states that LHMs need to be dispersive to produce positive total energy, implying that either $\partial(\epsilon\omega)/\partial\omega$ or $\partial(\mu\omega)/\partial\omega$ is less than zero to maintain the summation of electrical and magnetic energy to be positive.

In terms of real constitutive parameters, materials can be simply classified as positive materials ($\epsilon' > 0$, $\mu' > 0$), $\epsilon-$negative (ENG, $\epsilon' < 0$), $\mu-$negative (MNG, $\mu' < 0$), double negative materials (DNG, $\epsilon' < 0$, $\mu' < 0$). When μ or ϵ close to 0, they are called ϵ-near-zero ($\epsilon' \approx 0$), and $\mu-$near-zero ($\mu' \approx 0$) [29], where ENG and MNG are also called single-negative (SNG) media.

The substances that support negative ϵ or μ are of great interests to control electromagnetic waves. In fact, Veselago had analyzed the substances that are in principle possible in 1968 [25]. He expounded that gyrotropic material possess negativeness in real permittivity or permeability under a circular polarized excitation. A remarkable point he made was that there is no single substance that would yield isotropic and negative permeability due to the fact that *"magnetic sources are not charges but dipoles"*. He also explained if magnetic sources could arise from charges, *"a gas of such charges"* would have the form of $\mu_p = 1 - \omega_M^2/\omega^2$, where the subscript p stands for plasma, ω_M is a hypothesized magnetic plasma angular frequency, ω is the angular frequency. Such conclusion can be elaborated by referring to the origin of effective plasma permittivity derived from the Lorentz force on a moving charged particle (a monopole), where the effective plasma permittivity is expressed as $\epsilon_p = 1 - \omega_E^2/\omega^2$, and ω_E is the plasma angular frequency [30]. The hypothesis of the existence of such magnetic substance has been stated by Dirac in 1931 [31]. Veselago also pointed out that Dirac's argument is approximation which may

explain the lack of successful experiments in finding Dirac's monopole [25]. However, one point can be developed from Veselago's conclusion is that it might be possible to construct homogenized isotropic materials having negative permeability under Lorentzian dispersion model [27, 32, 33]. Pendry's early work on constructing electrically small structures [34] is an example. Their work does not limited to exploration of negative materials, but also provides insights on exploiting candidate materials for recently proposed magnetostatic resonance in electrically small isotropic particles with arbitrary shapes [35, 36]. The magnetostatic resonance is named as localized magnetostatic surface resonance (LMSR) in this work. It is important to address here that such LMSR should not be considered as the magnetic counter part of surface plasmon (as misinterpreted in Ref. [37]). In fact, it is the magnetic counter part of surface phonon due to absence of magnetic charge. Further details will be expanded and elaborated in Chapter 1.2.2.

The artificial materials with negative permittivity or permeability are called metamaterials. "Meta" comes from the Greek word "after", denoting a change of condition. It implies formation of new materials from engineered electrically small particles (meta-particles) [38]. A vast arrays of studies have been initiated to design metamaterials from microwave to optical frequencies. In microwave frequency range, printed circuit board (PCB) based inclusions are dominated to mimic MNG properties, including but not limited to split ring resonators (SRRs) [34], spiral elements [39], fractal Hilbert curve unit cells [40, 41], rose curve elements [42]; to mimic ENG properties, complementary SRRs [43, 44], wire rods or plates [32, 45], and meander lines [46] had been investigated. In terahertz or optical range, nano-technologies are favored to assemble periodically arranged nano-wires and nano-particles (self-assembled materials) [47, 48], fishnet structure [49], circle aligned paired-nanoparticles [50], amongst others.

As ideas based on tailoring the EM properties appeared, numerous applications based on metamaterials proliferated, leading to many profound impacts in nowadays technologies. One inspired application of metamaterial concept to this work's interest is near-field

enhancement in imaging beyond diffraction limit [18,51]. This application in principle is to enhance the evanescent wave in the near-field to construct a super-resolution image where the evanescent wave would be completely lost using a conventional lens with positive EM properties (Fig. 1.2). Enlightened by the above work, Boybay and Ramahi proposed a theoretical work on sensitivity enhancement using DNG and SNG media with light loss in 2009 [52], where DNG and SNG were first applied to near-field sensing in microwave regime. They also numerically demonstrated the sensitivity enhancement of a waveguide loaded with a $0.85mm$ thick SNG in terms of phase variation at $1mm$ statndoff distance [52]. Later on, an experimental verification on enhanced sensitivity was demonstrated using a small loop probe inserted in a periodically arranged SRR medium in Ref. [53].

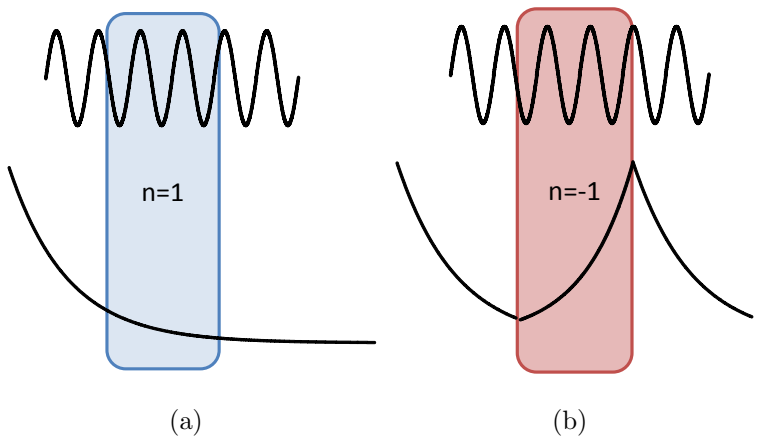

Figure 1.2: Near-field enhancement. (a) Convential lens with $n = 1$; (b) Super lens with $n = -1$

Inspired by these early works, I will propose a new MNP facilitated with a single meta-particle (i.e., an SRR) to achieve near-field enhancement of a low performance sensor. Details will be presented in Chapter 2. The sensing ability of the probe will be characterized by loss controllable liquid, and tested in biological tissue (i.e., ground chicken). Human tissue phantom is also investigated to sense the presence of abnormal lesion by

applying an electrically very small probe different from an SRR probe, which would pave the way for thereafter resonant particle labeled tumor sensing study in Chapter 5. The resonant particle is based on magnetostatic resonance which will be introduced in following Section 1.2.2. To detect such phenomenon in electrically very small volumes, a miniaturized probe with increased field confinement will be proposed and designated as two-loop resonator probe. The sensing mechanism will be expounded in Chapter 4 along with probe design details.

1.2.2 Localized magnetostatic surface resonance

Localized magnetostatic surface resonance (LMSR), was first proposed in the name of magnetostatic resonance through theoretical work on its eigenmodes in electrically very small arbitrary isotropic geometries having negative real permeability [35, 36]. According to EM duality, such magnetic phenomenon can be roughly considered as magnetic counter part of electrostatic resonance. However, there are some constraints on these pairing terminologies, as electrostatic resonance generally refers to resonant structures that are electrically very small with negative real permittivity; it is not associated to physics behind its occurrence, for instance free electron movement in alkali particles [54], bounded electron movement in ironic crystal particles, such as NaCl [54], or Bloch waves in metamaterial resonators [55]. These physics are closely associated to supporting materials, say natural material or metamaterials made by periodically structures.

Electrostatic resonances are typically referred localized surface excitations. The origin of surface excitation perhaps dates back to 1949 when Fröhlich derived polarization oscillation frequency in small spherical dielectric crystals whose permittivity function is based on one-oscillator Lorentz model [56,57]. This oscillation frequency, also referred to as Fröhlich frequency, occurs when the dielectric constant of a sphere, ϵ, and its surrounding medium, ϵ_b, satisfy the equality $\epsilon = -2\epsilon_b$ [56]. The resonance exhibited (also referred to as Fröhlich

modes) when the equality is satisfied, is essentially the lowest surface mode derived from classical electromagnetics. This phenomenon was later referred to as surface phonon [56] or electronic resonance [54]. In 1957, Ritchie's prediction of surface plasmon existence in metal thin film lead to the emergence of the next family of surface excitation, called localized SP, in electrically very small metal spheres whose permittivity is described by Drude model [58].

Surface phonon and surface plasmon are two common electrostatic resonances occurring in natural materials at optical frequencies. Their names phonon and plasmon refer to quantized lattice wave and quantized plasma (charge density) wave which imply the physics behind these two phenomena [56]. According to Drude-Lorentz-Sommerfeld equation for the dielectric function [54],

$$\epsilon = \epsilon_f + \delta\epsilon_b = 1 - \frac{\omega_{pe}^2}{\omega^2 + i\gamma_e\omega} + \sum_j \frac{S_j\omega_{pj}^2}{\omega_j^2 - \omega^2 - i\gamma_j\omega} \tag{1.7}$$

where ϵ_f is free electron contribution, $\delta\epsilon_b$ is Lorentz oscillator contribution due to bounded electron movements, surface plasmon is due to free electron movement which is reflected in Drude susceptibility, the second term of Eq. 1.8; while surface phonon is due to bounded electron movement described by multiplicity of Lorentz oscillators in the last term [54]. Subscript e is appended to free electron parameters, and p is appended to plasma frequency. Parameter γ is damping factor, S is oscillator strength, and j refers to jth oscillator. The summation in the last term Eq. 1.8 allows the formulation to apply at a board range of frequencies [56]. As mentioned in Section 1.2.1, due to absence of magnetic monopole, LMSR is not the magnetic counter part of surface plasmon, but the counter part of surface phonon. Therefore, the magnetic dispersion of LMSR is expected to have Lorentzian dispersion described as follows.

$$\mu = 1 + \sum_j \frac{F_j \omega_{mj}^2}{\omega_j^2 - \omega^2 - i\gamma_{mj}\omega} = 1 + \sum_j \frac{F_j}{\left(\frac{\omega_j}{\omega_{mj}}\right)^2 - \left(\frac{\omega}{\omega_{mj}}\right)^2 - i\gamma_{mj}\frac{\omega}{\omega_{mj}^2}} \tag{1.8}$$

where subscript m refers to magnetic quantities, and F corresponds to magnetic oscillator strength. This dispersion have been widely used in mimicking magnetic dispersion of magnetic materials [59] and metamaterials [27, 32–34].

Up to now, the physics and existence of LMSR is unknown. No experimental reports had demonstrated LMSR, and no detection mechanism was proposed to sense the LMSR in electrically small particles. The reason behind the absence of research may be due to lack of significant magnetic dispersion at optical frequencies [26]. A few recent works on non-linear dielectric liquids have demonstrated magneto-static behavior at discrete points along their surfaces at optical frequencies [60, 61], whereas the electrically very small liquid form particles are not trivial to construct. Solid form metamaterial with low magnetic loss would be suitable due to proliferated metamaterial types at microwave frequencies, such as garnet [62, 63], hexaferrite [64–66], ferrites films [67, 68], and magnetic metallic grains [67–71]. These materials possess significant magnetic dispersion that yields negativeness of real permeability at frequencies after that of ferromagnetic or ferrimagnetic resonance (FMR). FMR was proposed by Griffiths in 1946 [72]. It is a resonant phenomenon happening at frequency where maximum magnetic absorption occurs. In 1948, shape dependency of FMR was also investigated in ferromagnetic spheres by Kittle [26, 73]. Such resonance was later on categorized as homogeneous magnetostatic ocillation [26, 74]. The inhomogeneous magnetostatic ocillations were found later in ferromagnetic spheres by Walker in 1957 [75]. Walker's work was followed by extended study on ferrite spheres, disks and rods by Dillon [76–79]. It is very interesting to notice that the purpose of these earlier works were attempted to study the absorption behavior in magnetostatic oscillations modes. Henceforth, the characteristic equation is associated with rotation parameters (off diagonal imaginary values) in permeability tensor [75]. In a recent work on helical

mode resonance, negative quantities of permeability tensor diagonal values were explicitly addressed in small ferrimagnetic disks by Kamenetskii in 2010 [80, 81] to provide physical solution to magnetostatic potential. In Kamenetskii's work the electrically very small disks were axially magnetized (magnetization perpendicular to circular surface), suggesting helicity along axial direction. This fact would be very crucial to distinguish the phenomenon observed in the experiments. Up to now, the physics of LMSR is unknown. No reports have demonstrated the potential applications on LMSR. Therefore, this work shall only focus on detecting electrically small resonant particles having effective negative permeability, designated as LMS resonant particles.

In this work, I shall focus on detection of LMS resonant particle with negative permeability in the direction of alternating field. An electrically very small near-field loop resonator will be constructed to detect LMSR. The detection methodology will be proposed, and the Lorentzian dispersion will be applied to predict possible experimental results. The detection of electrically small resonant particle with negative permeability in this work can have strong impact on marker-based sensing applications in biomedicine and bioengineering. Details will be presented in Chapter 4.

1.3 Outline of thesis

In Chapter 1, a literature review on development of MNPs and state of the art metamaterial science had been presented to provide motivation of MNP design from these inspirational works on metamaterials. Followed by the introduction of recently proposed magnetostatic resonance [35, 36], a literature review on these new magnetic concepts had been provided to demonstrate the motivation of near-field detection of such magnetic resonance. The remaining of this dissertation will be outlined as follows.

Chapter 2 will focus on proposal of a new near-field probe based on evanescent wave en-

hancement concept implemented by single metamaterial unit structure, single SRR, placed next to a simple loop resonator. A spectrum analysis based on spatial harmonics at the probe plane will be illustrated, suggesting the predicted evanescent wave enhancement in comparison with the loop resonator without insertion of SRR. Numerical simulations will be carried out to validate the SRR probe design and verified by experiments. The probe will be tested and characterized in the presence of a small metallic abnormality buried in lossy medium. The resolution of the probe will be demonstrated.

The sensing scenario for a biological medium can be further extended to the human tissue environment, such as breast tissue. In Chapter 3, an anatomically realistic breast phantom will be constructed for near-field sensing using a narrow band probe to avoid dispersion. Two different sizes of tumor will be embedded at five different locations respectively. Variations of probe reflection coefficient will be observed. Such probing scenario can be beneficial to magnetic marker labeled tumor sensing in the future.

In Chapter 4, the SRR probe will be improved by a miniaturization design to confine the magnetic field to a smaller region. A circuit model will be proposed for the miniaturized probe. To perform the detection of electrically small particles with negative permeability, the model will be re-solved after loading an isotropic magnetic sphere placed concentrically with the loops using magnetostatic boundary condition at the sphere surface. A detection methodology will be proposed and expounded using this circuit model. The effect on insertion of a resonant sphere will be discussed under magnetostatic resonance condition in premise of negative real permeability. The sensing signature of two resonances in probe reflection coefficient is theoretically predicted and validated by full-wave numerical simulations. Experiments will be presented using ferrimagnetic particles having effective negative real permeability in direction of a microwave excitation.

At the end, suggested future work will be proposed in Chapter 5, the contributions in this dissertation work will be concluded in Chapter 6.

Chapter 2

Microwave Split-Ring-Resonator Probe

MNPs can be constructed differently with the primary objective of creating a detection element (tip or probe) that is highly sensitive to the morphology and composition of materials placed next to it. As mentioned in Chapter 1, some near-field probes are transmission line resonators terminated with a probing aperture [4, 82], or simple open-ended transmission lines [14, 15]. Other probe types include transmission lines or resonators ended with a sharpened tip or a small loop [8, 12, 13, 83]. The electromagnetic field of above MNPs is highly confined to the close proximity of the small aperture, the sharp tip or loop, but decays as field travels away from the probing end. Therefore, their applications are actually constrained to samples with low surface roughness and to laboratory environment where the standoff distance (distance between the object to be detected and the probe) is controlled in the order of micrometers by vibration-control equipment [12]. Advancement in metamaterials has offered a new perspective in constructing near-field probes, especially in the range of microwave frequencies, as the unit cells of the metamaterials can be made by printed circuit technology.

2.1 Design idea

Earlier theoretical work on double negative media (DNG) and single negative media (SNG) showed that such media can enhance the sensitivity of generic near-field probes by increasing the evanescent field energy in the close proximity of the probe [52]. A μ-negative SNG medium was realized for a probe made of an electrically small loop [84]. The SNG medium was realized using a stack of split-ring resonators (SSRs) [34, 84]. The effective permeability of the SRR medium was characterized using transmission reflection extraction method [85], assuming the composite medium is made of infinite number of SRR particles placed periodically as shown in the inset of Fig. 2.1. The resonant frequency of the SRR medium depends on not only the periodicity of the unit cells but also the coupling between them. Figure 2.1 shows a typical effective permeability of infinitely periodic stacks of SRR particles. The effective permittivity of the composite medium is dependent on the polarization of the incident field, which is assumed to be perpendicular to the plane of the SRR particles. However, it was noticed that only a small region in the SNG volume was excited and only this region contributed to the enhancement in the detection [84]. Inspired by this observation, a probe with only a *single* SRR is constructed. Compared to a loop without an SRR, the evanescent field in the close proximity of the probe is expected to enhance.

2.2 Probe design

SRR is the most common element or particle used to design metamaterials having either enhanced positive permeability or negative permeability. In Fig. 2.2, the SRR is made of two concentric loops with splits on opposite sides. The time varying magnetic flux of an external excitation penetrates the area encircled by the inclusions, and produces an induced surface current on the metal traces. Due to the splits, the current is forced to flow between the loops, creating resonance at a wavelength much larger than the size of the

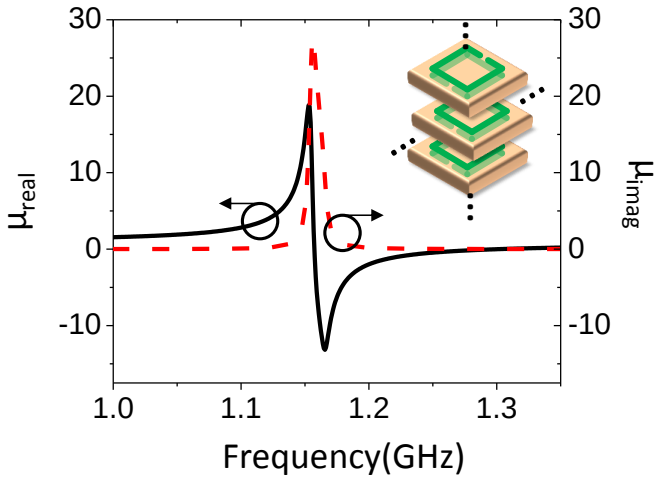

Figure 2.1: A demonstration of effective permeability of periodically arranged SRRs.

loops.

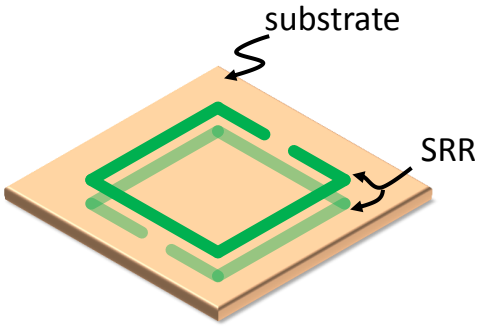

Figure 2.2: A rectangular broad-side coupled SRR printed on a substrate.

Unlike works where the interest is in constructing single or double negative medium, the interest here is on the resonance behavior rather than the frequency over which the effective permeability is either positive or negative. Therefore, in this chapter, the resonance behavior of a single SRR is exploited. At the resonance, the SRR achieves maximum electrical energy in distributed capacitance between the loops, and maximum magnetic en-

ergy in loop enclosures. To this end, the SRR is an open resonator which makes it highly susceptible to its neighborhood environment. Hence it is proposed to detect changes in its vicinity [86].

In sub-surface detection techniques, a compromise is made when choosing the operation frequency. The lower the frequency is the deeper the penetration of the field inside the medium under study, however, the wider the distribution of the field at the probing end (larger dimension of the probe), implying less detection resolution. On the other hand, the higher the frequency, the lower the field penetration, but the higher the concentration (smaller dimension of the probe) and consequently higher the detection resolution. Therefore, the selection of frequency is not of great interest here. The main objective of this work is to demonstrate that one single meta-particle with appropriate excitation would act as a sensitive sensor.

In this work, the resonant frequency of the probe is chosen at around $1GHz$ where penetration of microwave is in the order of centimeters in high loss media, such as meat and human tissue [87, 88]. The probe introduced here is composed of a single SRR and a rectangular loop as shown in Fig. 2.3. The primary purpose of the rectangular loop is to excite the SRR with a magnetic field polarized in z-direcion. The loop is square shape with dimension of $20mm \times 20mm$. The SRR designed in this work is typically referred to as a broad-side coupled [89] with two rectangular metallic traces on the top and bottom of a low-loss substrate, as shown in Fig. 2.3(a). The substrate is Rogers Duroid 4350 with dielectric constant of 3.48, loss tangent of 0.004 at $10GHz$. The thickness of the substrate is $0.762mm$. The size of the metallic traces of the SRR is $10mm \times 10mm$ with an opening of $1mm \times 1mm$. The substrate dimension is $16mm \times 16mm$. The tail of the loop excitation is $87.5mm$ measured from the gap of the loop to the end of the tail. The morphology and the operating frequency of the SRR were chosen as an example to demonstrate the sensitivity enhancement. Other frequencies can also be chosen with appropriately designed SRRs.

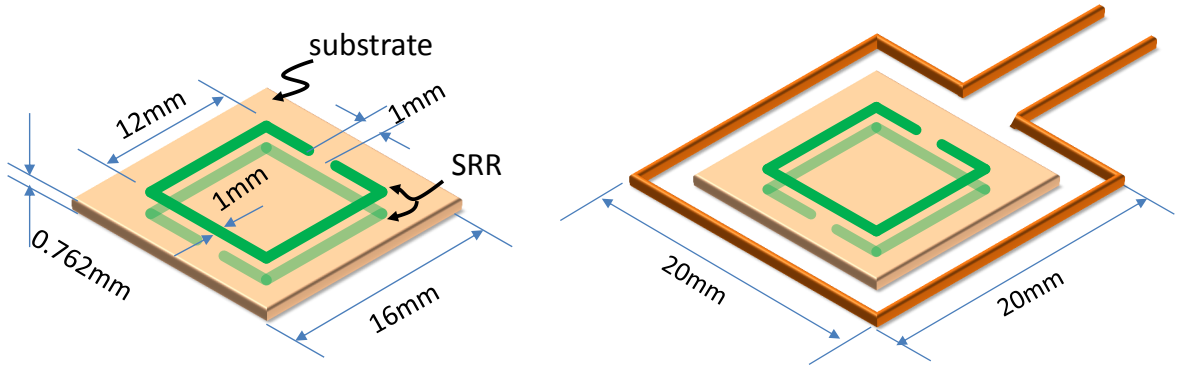

(a) (b)

Figure 2.3: SRR probe design. (a) The geometry and dimensions of the SRR. (b) The SRR is excited by the H field generated by a rectangular loop.

2.3 Theory of evanescent wave enhancement

The effect of attaching an SRR to a classical square loop probe can be analyzed by studying the spectrum of the field in the close proximity of the probe. Spectral or Fourier analysis reveals the strength of each spatial harmonic on a selected plane and the presence or absence of evanescent fields which are critical in near-field detection. To this end, the spectrum of the z-component of the magnetic field (H_z) is calculated over the x-y plane parallel to the plane of the SRR. The spectrum is given by the Fourier transformation

$$F(k_x, k_y) = \int_{-\infty}^{\infty} \int_{-\infty}^{\infty} H_z(x, y) e^{-j(k_x x + k_y y)} \, dxdy \tag{2.1}$$

where k_x and k_y are the components of the wave vector in the x and y directions, respectively. Each (k_x, k_y) combination represents a spatial harmonic and $F(k_x, k_y)$ represents its magnitude or strength. The distribution of H_z was calculated using the full-wave simulator Microwave Studio CST 2012. If the spatial components, k_x and k_y, are normalized by $k_0 = \omega\sqrt{\mu_0 \epsilon_0}$, where μ_0 and ϵ_0 are the permeability and permittivity of free space, respectively, and $\omega = 2\pi f$ corresponds to frequency of interest. The dispersion relationship

is expressed as

$$\left(\frac{k_x}{k_0}\right)^2 + \left(\frac{k_y}{k_0}\right)^2 = 1 - \left(\frac{k_z}{k_0}\right)^2 \tag{2.2}$$

At $k_z = 0$, the dispersion relationship reduces to $(k_x/k_0)^2 + (k_y/k_0)^2 = 1$, which describes a unit circle as shown in Fig. 2.4. The circle represents the cutoff condition for the propaga-

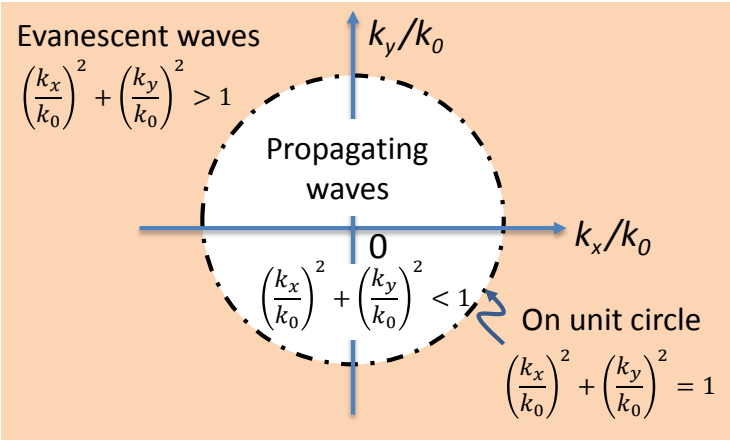

Figure 2.4: Spectrum analysis based on unit circle criterion.

tion in the z-direction. If k_z is real, the right-hand side of Eq. (2.2) is less than 1, indicating any spacial harmonics inside the unit circle represent waves propagating in the z-direction. On the other hand, if k_z is imaginary, the right-hand side of Eq. (2.2) is greater than unity, implying that any spacial harmonics outside the unit circle represents a field that evanesces in the z-direction. Therefore, the spectrum of the normalized spacial components unveils the distribution and strength of each spatial harmonic and its propagation or evanescence behavior.

Figure 2.5(a) and (b) show the H_z field distribution on an x-y plane positioned $864\mu m$ above the plane of the loop *without* the SRR and the corresponding amplitude of $F(k_x, k_y)$ in the $k_x - k_y$ plane, respectively. Fig. 2.5(b) is normalized spectrum with respect to loop operation frequency $3.93GHz$. Fig. 2.6(a) and Fig. 2.6(b) show the H_z field distribution

on an x-y plane positioned $864\mu m$ above the plane of the loop (SRR surface plane) *with* the SRR and the corresponding amplitude of $F(k_x, k_y)$ in the $k_x - k_y$ plane, respectively. Fig. 2.6(b) is normalized spectrum with respect to SRR probe operation frequency of $1.214GHz$. These calculations clearly demonstrate that the evanescent magnetic field in z-direction is significantly enhanced due to the insertion of the SRR. Hence, the sensitivity of the probe in z-direction is expected to increase.

It is also interesting to observe the spectrum of the SRR probe in presence of a perturbation, for instance, metallic cubes with size of $1mm$ and $0.5mm$ placed in the center of the loops. By comparing the spectrum before (Fig. 2.7 (a)) and after the perturbation (Fig. 2.7 (b) and (c), where (b) for cube size of $1mm$ and (c) for cube size of $0.5mm$), one can observe that the evanescent waves with higher wavenumber (k_x and k_y) are increased due to perturbation of metallic cubes.

2.4 Applications in lossy medium sub-surface detection

From the above spectrum analysis, it can be concluded that the evanescent wave gathered in the near-field would be beneficial to detect a target placed in the close proximity of the probe. In the following sections, a target will be detected in a background medium using the SRR probe. Such detection is referred to as sub-surface detection that resembles several important engineering applications such as detection of biological anomalies in human tissue [90], detection of land mines in soil [91], and detection of steel in concrete [92]. These techniques require durability of the probe as the background deteriorates the signal due to absorption loss.

To have host medium with controllable permittivity, sodium chloride (NaCl) solution is used as its conductive loss can be controlled by varying the salinity of the solution

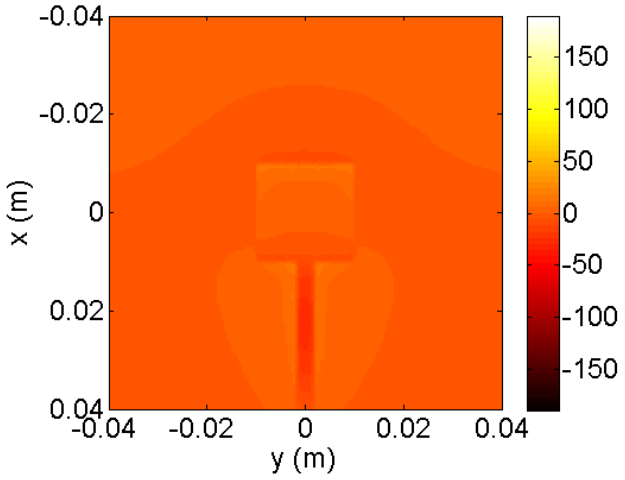

(a)

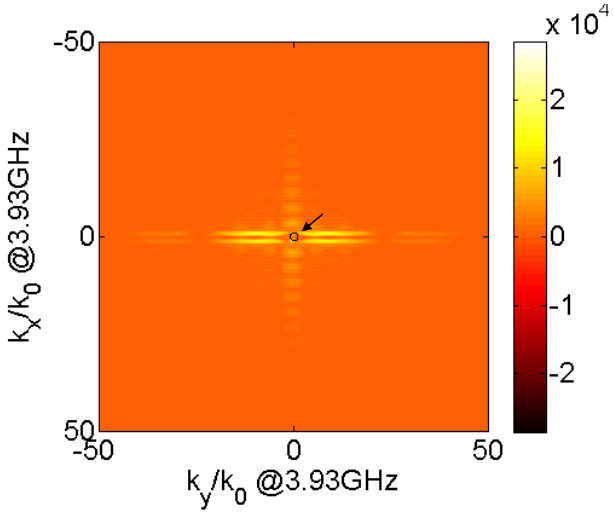

(b)

Figure 2.5: Field distribution and its spectrum for a loop probe. (a) The field distribution of H_z. (b) The spectrum of H_z in normalized k_x-k_y plane. The Fourier transform of the data presented in (a) is used to generate the spectrum.

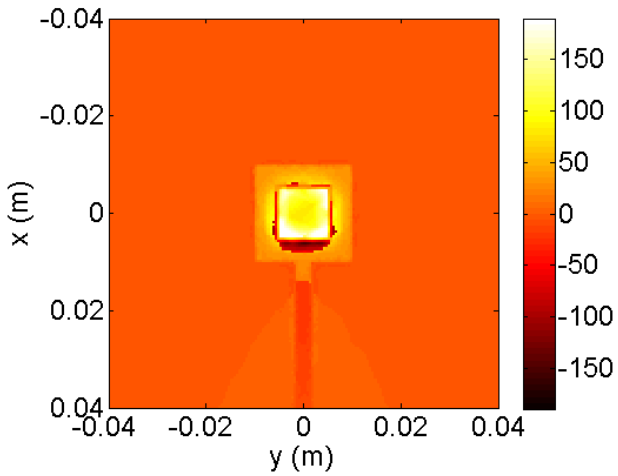

(a)

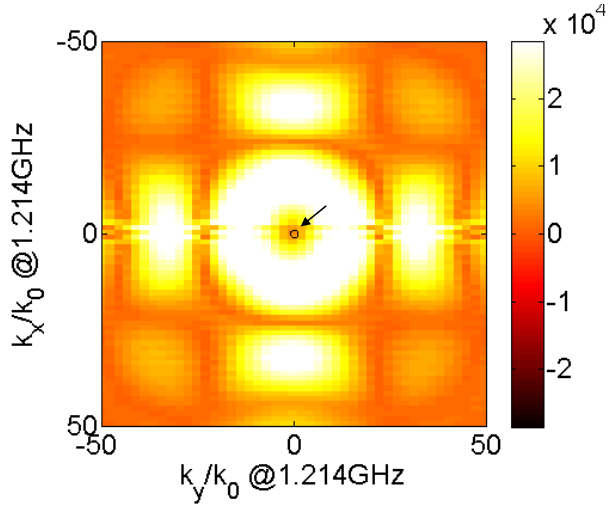

(b)

Figure 2.6: Field distribution and its spectrum for the same loop probe loaded with SRR (the SRR probe). (a) The field distribution of H_z. (b) The spectrum of H_z in normalized k_x-k_y plane. The Fourier transform of the data presented in (a) is used to generate the spectrum.

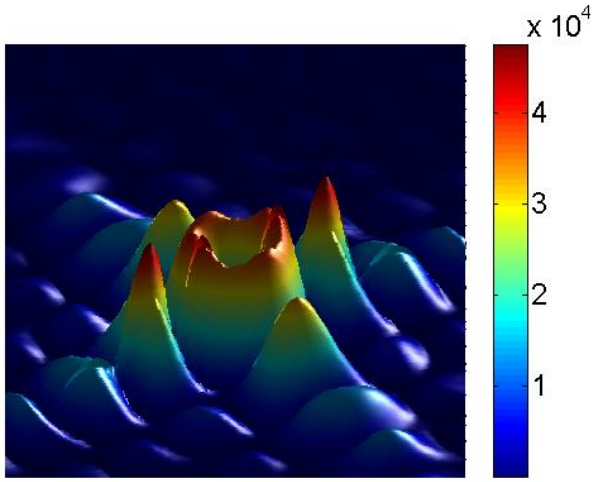

(a)

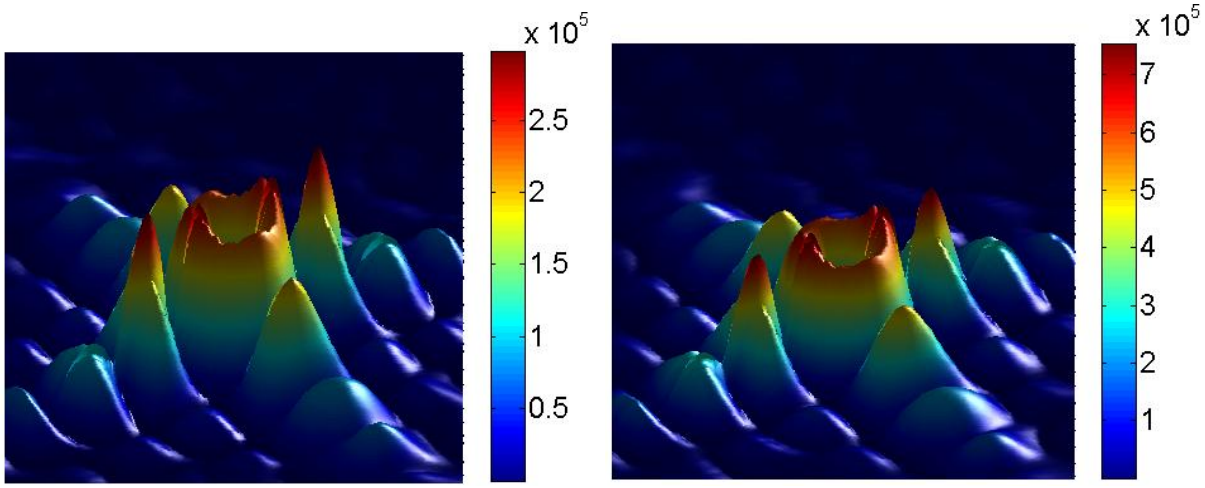

(b) (c)

Figure 2.7: Field spectrum three-dimensional plot of H_z in normalized $k_x - k_y$ plane before and after presence of metallic cubes with different sizes. (a) The spectrum for SRR probe. (b) The spectrum for cube size of $1mm$. (c) The spectrum for cube size of $0.5mm$.

according to Klein and Swift's model [93] at microwave frequencies. Their model was improved from Debye dispersion model (Eq. (2.3)) for practical use, as some parameters (i.e., static permittivity, ϵ_s) can be calculated by measurable quantities, such as salinity (S) and temperature (T).

$$\epsilon = \epsilon_\infty + \frac{\epsilon_s - \epsilon_\infty}{1 + (j\omega\tau)^{1-\alpha}} - j\frac{\sigma}{\omega\epsilon_0} \tag{2.3}$$

where ϵ_∞ is permittivity at infinite frequency, σ is conductivity, τ is relaxation time, and α is empirical parameter that describes the distribution of relaxation times. At lower frequencies, $\alpha = 0$. The expressions of the parameters in Eq. (2.3) associated with S and T are enumerated as follows.

$$\begin{aligned}\epsilon_s = (87.134 - 1.949 \times 10^{-1}T - 1.276 \times 10^{-2}T^2 + 2.491 \times 10^{-4}T^3) \\ \times(1 + 1.613 \times 10^{-5}ST - 3.656 \times 10^{-3}S \\ +3.21 \times 10^{-5}S^2 - 4.232 \times 10^{-7}S^3)\end{aligned} \tag{2.4a}$$

$$\begin{aligned}\tau = (1.768 \times 10^{-11} - 6.086 \times 10^{-13}T + 1.104 \times 10^{-14}T^2 - 8.111 \times 10^{-17}T^3) \\ \times(1 + 2.282 \times 10^{-5}ST - 7.638 \times 10^{-4}S - 7.76 \times 10^{-6}S^2 + 1.105 \times 10^{-8}S^3)\end{aligned} \tag{2.4b}$$

$$\sigma(T, S) = \sigma(25, S)e^{-\Delta\beta} \tag{2.4c}$$

$$\Delta = 25 - T \tag{2.4d}$$

$$\sigma(25, S) = S(0.182521 - 1.46192 \times 10^{-3}S + 2.09324 \times 10^{-5}S^2 - 1.28205 \times 10^{-7}S^3) \tag{2.4e}$$

$$\begin{aligned}\beta = 2.033 \times 10^{-2} + 1.266 \times 10^{-4}\Delta + 2.464 \times 10^{-6}\Delta^2 \\ -S(1.849 \times 10^{-5} - 2.551 \times 10^{-7}\Delta + 2.551 \times 10^{-8}\Delta^2)\end{aligned} \tag{2.4f}$$

From Eq. (2.3) to Eq. (2.4f), loss control of NaCl solution can be implemented by varying liquid salinity to produce different values of imaginary permittivity. The detection of abnormalities in such loss controllable medium would help to characterize the capability of a probe in sub-surface sensing with respect to background medium loss. The corresponding conclusions would assist the estimation of biological sub-surface detection (i.e., in ground chicken).

2.4.1 Probe design Validation

To validate the probe design through experimental measurements and numerical simulation, an SRR and an excitation loop were designed using the dimensions presented earlier. The magnitude and phase of the reflection coefficient (S_{11}) were measured using an HP 8722ES vector network analyzer. The measurements were made over the $1GHz$ to $1.5GHz$ frequency range, with an IF bandwidth of $3kHz$. The probe was fixed on to a polyvinyl chloride (PVC) board (Fig. 2.8) to insure immobility during testing. The S_{11} was measured and compared with full wave simulation results obtained from CST Microwave studio 2012 as demonstrated in Fig. 2.9. The slight deviations between simulation and measurement in the levels of the magnitude and phase are attributed to the several assumptions, including mismatch of probe dimension in fabrication, and the lossless property of PVC medium used in the full wave simulation.

Figure 4.8 shows that at the resonant frequency, approximately 90% of the energy is delivered to the probe. Using numerical simulation, the radiation efficiency of the entire probe system was found to be negligible. This implies that most of the energy transmitted to the probe is dissipated as heat in the probe or probe medium. Under the assumption of the lossless property in PVC material, the power loss density (PLD) was calculated numerically and is shown in Fig. 2.10. The calculated PLD is defined as the time derivative of the incremental energy dW, dissipated in an incremental volume, dV, with incident power of 1 W, in Eq. (2.5). As expected, energy dissipation is confined to the substrate of the SRR as shown in Fig. 2.10.

$$PLD = \frac{d}{dt}(\frac{dW}{dV}) \tag{2.5}$$

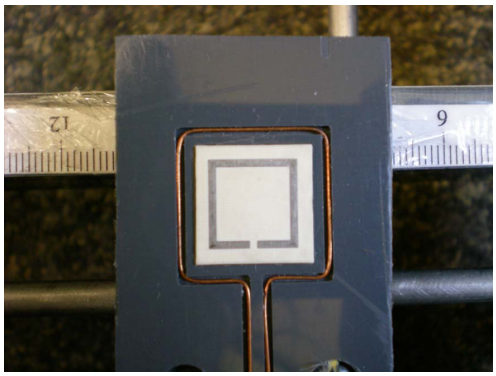

(a)

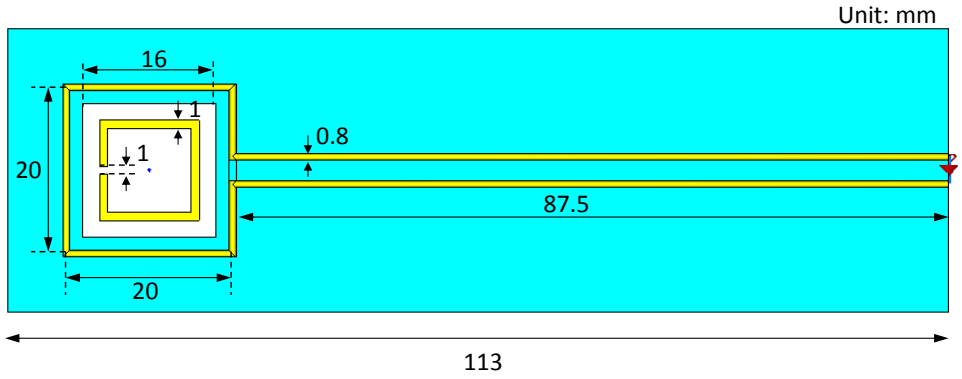

(b)

Figure 2.8: (a) The unloaded probe with PVC fixture at the bottom. (b) The schematic of the structure in numerical simulation.

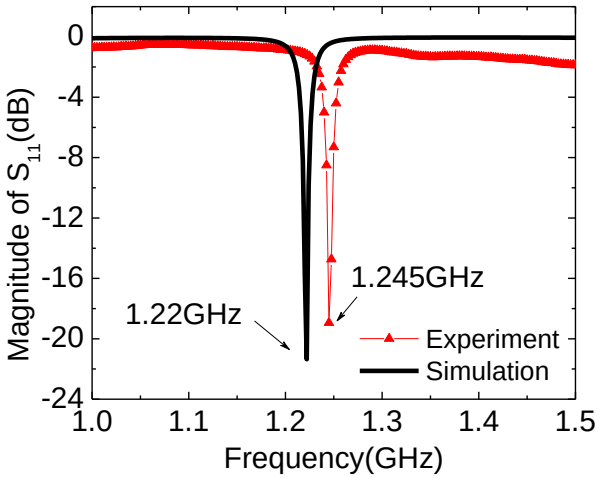

(a)

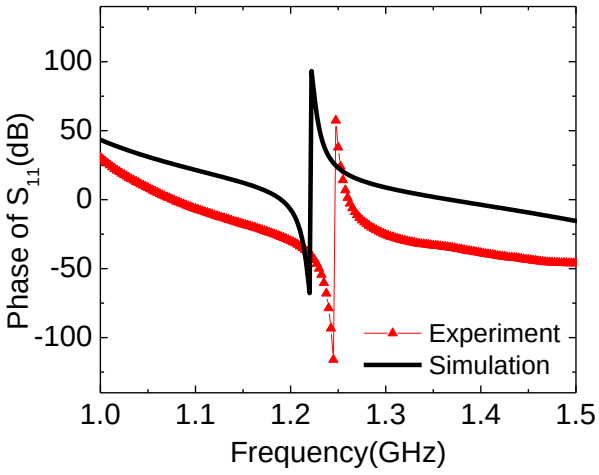

(b)

Figure 2.9: The S_{11} of the unloaded probe is measured experimentally and compared with numerical results. (a) Magnitude of S_{11} in dB. (b) Phase of S_{11} in degrees.

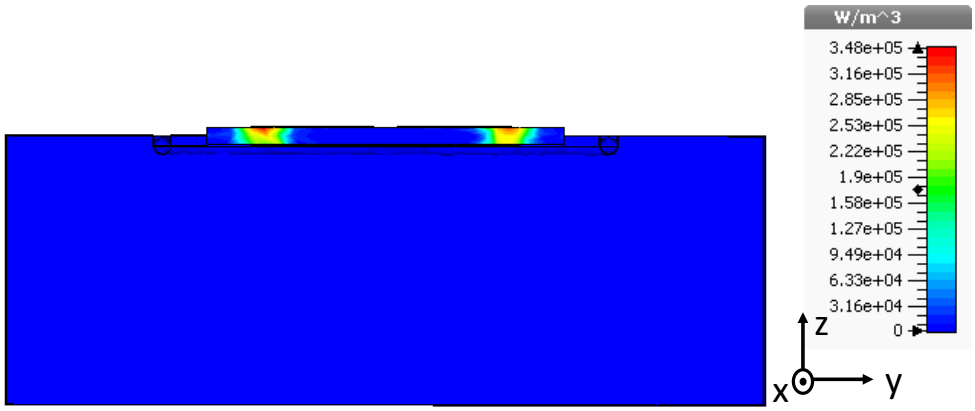

Figure 2.10: Power loss density over the cross section of the experimental setup. The power is being lost in the substrate between the two rings of the SRR.

2.4.2 Pre-detection calibration

Before sensing the abnormality in host medium, another important step is to examine the probe performance by loading the host medium, as any passive resonator design would surfer from deterioration of quality factor (Q-factor) [94]. This pre-detection calibration procedure is important because the resonant frequency of the SRR can change from that of the unloaded probe to the response when the probe is loaded with the host medium. The main interests of this work is sub-surface detection as opposed to characterization of material (which may be possible for future study). Therefore, host medium is considered to be lossy which is significantly more challenging than lossless host media due to field decay. In presence of a small abnormality in the lossy target medium, a more prominent change in the phase of the S_{11} was observed in comparison to the change in its magnitude. This occurs because the amplitude of S_{11} is mostly affected by the surface resistance of the host medium material [95]. An electrically-small buried object does not have significant effect on the surface resistance. Therefore, the detection was based on monitoring the phase shift according to the definition described above.

To attain maximum sensitivity for a specific host medium, the probe was calibrated for that specific host medium in the sense that the frequency selected for the operation of the probe corresponds to the resonant frequency of the SRR in the presence of the host medium. At resonant frequency, phase measurement has maximum sensitivity and dynamic range. In addition to microwave properties, any change in the standoff distance which is defined as the distance between the probe and host medium, also affects the phase response. A differential probe can be adopted as suggested in Ref [17, 96]. An equivalent approach is adopted here. First, a phase scan is taken without the buried object, then perform another scan with the buried object. By subtracting the two phase scans, a phase map over the scanning distance can be obtained. The maximum phase change indicates the presence of the buried object and its lateral location.

2.4.3 Saline water experiment

To demonstrate the increased sensitivity of the new probe system, experimental results of the loop with and without single SRR were compared. The NaCl solution was placed in an acrylic container with thickness of $6.35mm$. The buried target is an Aluminum block with dimensions of $3.24mm \times 3.24mm \times 3.24mm$. The block was attached to a scaled plastic rod to easily monitor and record vertical displacement. Fig. 2.11 shows the setups used for the experiment. The scanning stage is in the lower part, the acrylic box is placed above, and the aluminum cube is merged into the 1% NaCl solution.

By applying the improved model by Klein and Swift [93] for saline liquid as mentioned in Section 2.4, relative permittivity of the saline water from $0.5GHz$ to $2GHz$ was calculated. In addition, relative permittivity of the saline liquid was measured by using an open-ended coaxial line (RG-8). Kraszewski calibration method [97] was applied where distilled water was used as the standard calibration liquid. Kraszewski calibration method was improved by adding the loss of the coaxial line into the characteristic impedance of the coaxial

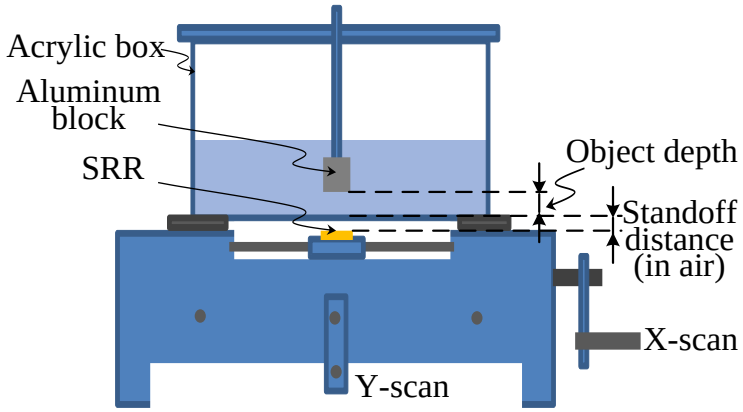

(a)

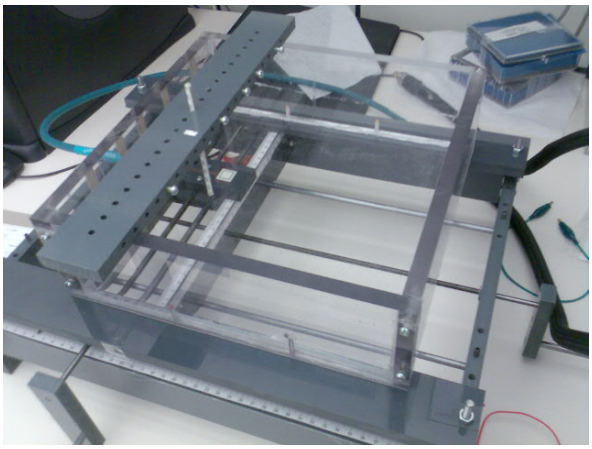

(b)

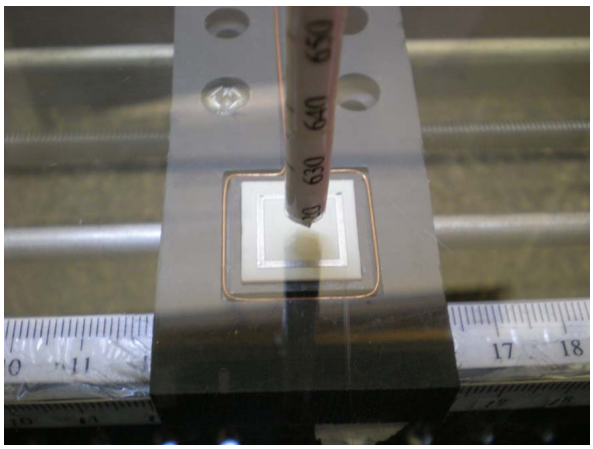

(c)

Figure 2.11: Configuration of the experimental setup. (a) The schematic of the experimental setup. (b) The entire scanning stage and the sample box. (c) The probe with PVC fixture at the bottom.

line. As a result, the mismatch between the coaxial line measurement and the model of Klein and Swift is less than 4% for real part of complex permittivity, and less than 7% for imaginary part of complex permittivity, as shown in Fig. 2.12. The mismatch is not of high importance in this work, as the objective here is merely to have a reasonable measure of the loss of the saline water in order to understand the effectiveness of the probe in detecting objects buried in lossy media. The primary objective is to detect the object buried in the host medium whose constitutive and loss characteristics may not be known in advance.

Figure 2.11(a) is a schematic of experimental setup, where the probe is positioned $1mm$ away from the bottom of the acrylic container. The Aluminum cube depth is the vertical distance between the bottom of the liquid container and the cube (Fig. 2.11(a)), and is controlled by a scaled rod (Fig. 2.11(c)). Following the calibration procedure mentioned in Section 2.4.2, the operation frequency was determined to be $1.218GHz$. At this frequency, the measured relative permittivity of 1% saline solution is $76 - j24$. By scanning the probe over the bottom of the box, a phase map was obtained. To eliminate the effect of standoff distance fluctuations, background phase change was recorded before immersing the Aluminum block into the solution. Figure 2.14 and Fig. 2.15 illustrate the phase changes obtained after subtracting the phase background noise for different object depths.

As the cube moved closer to the probe, maximum phase change of the SRR-enhanced probe increased as shown in Fig. 2.14 and Fig. 2.15. However, the probe without the SRR gave practically no phase change. A maximum phase change of 8° was observed for the probe with SRR as shown in Fig. 2.14(a) when the cube's depth was $1mm$ while no obvious phase change was observed for the probe without SRR. A phase discrepancy from the two sides of the main lobe in Fig. 2.14 and Fig. 2.15 is due to uncertainty in the measurements of the distance between the probe and the bottom of the container. It is important to note that for the case of cube's depth of $1mm$, the total distance between the probe and cube is approximately $8.35mm$.

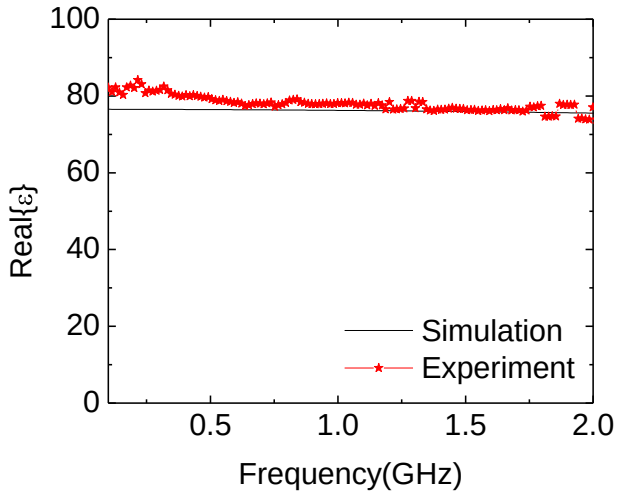

(a)

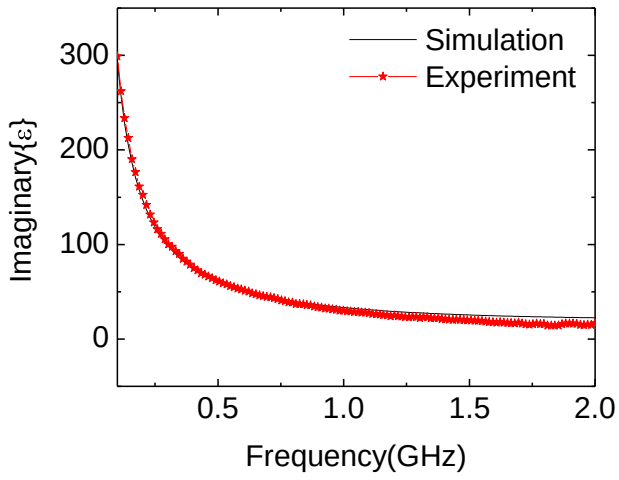

(b)

Figure 2.12: 1% saline solution characterization (a) Real part of the relative permittivity. (b) Imaginary part of the relative permittivity.

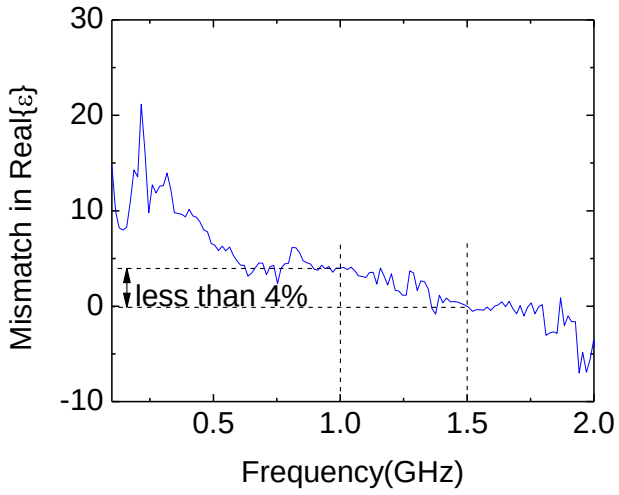

(a)

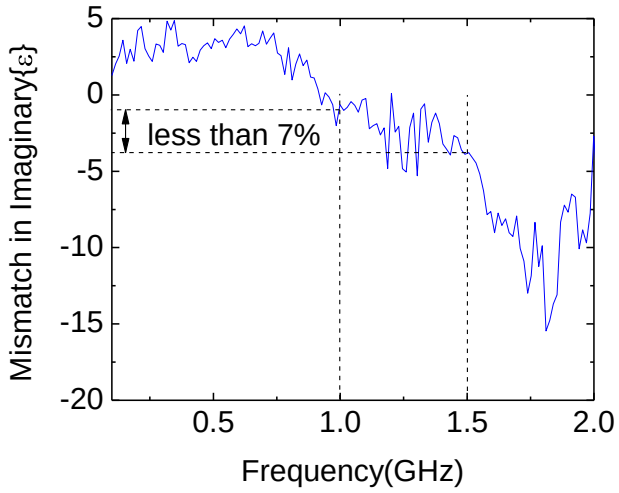

(b)

Figure 2.13: Mismatch of theoretical and experimental results for characterization of 1% saline solution. (a) Mismatch for real part of relative permittivity. (b) Mismatch for imaginary part of relative permittivity.

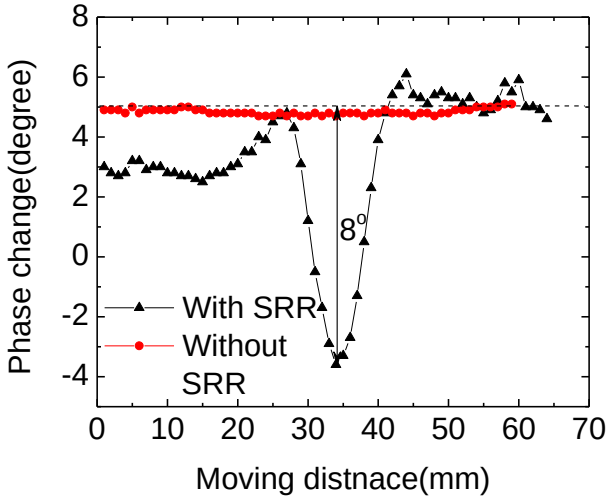

(a)

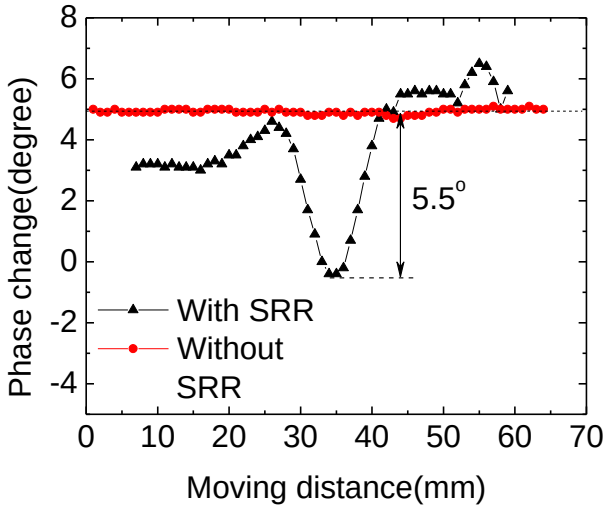

(b)

Figure 2.14: Comparison of phase change for probe with and without SRR. The Aluminum block is placed at 35mm and scannings were performed for different object depths. (a) Object depth is 4mm. (b) Object depth is 3mm.

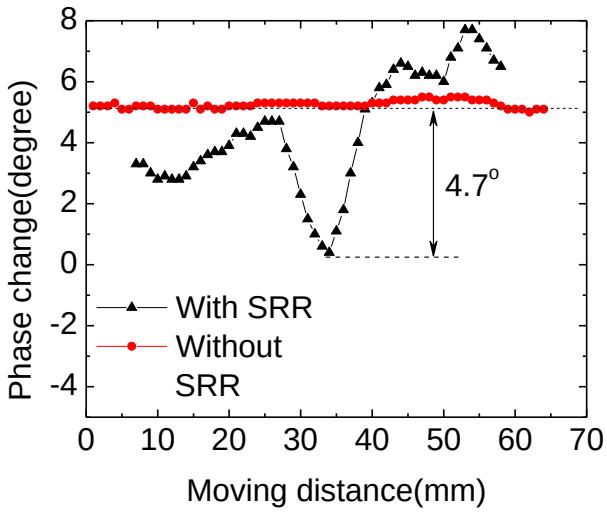

(a)

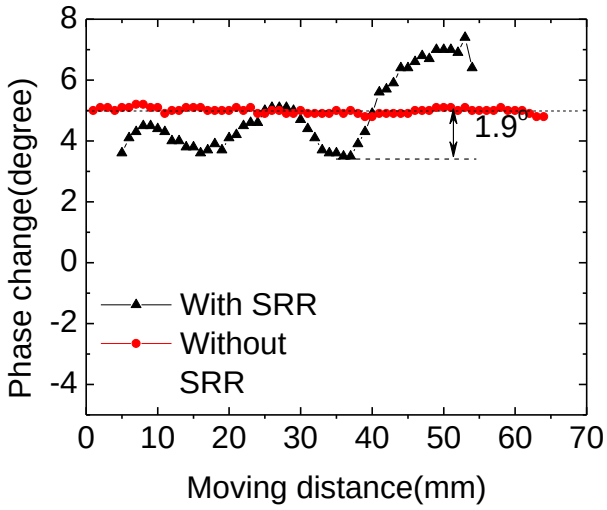

(b)

Figure 2.15: Comparison of phase change for probe with and without SRR. The Aluminum block is placed at $35mm$ and scannings were performed for different object depths. (a) Object depth is $2mm$. (b) Object depth is $1mm$.

When the loss of the host medium increases, the probe sensitivity is expected to decrease. To investigate the detection depth in different lossy media, measurements is conducted using pure distilled water and 1%, 2% and 3% NaCl solutions. The measured complex permittivities at the resonance frequency corresponding to the four media were $78.5 - j4.8$, $76.5 - j24$, $75.9 - j50.4$ and $73.3 - j71.9$, respectively. The depth of the Aluminum cube is controlled by adjusting the height of the rod (Fig. 2.11(c)). Fig. 2.16 shows the phase change with respect to the cube's depth. Notice that even for the very lossy medium of 3% NaCl solution with a loss tangent of approximately unity, the probe was able to sense the presence of the cube with depth of $1 - 2mm$ despite a standoff distance of $1mm$ (air) and container thickness of $6.35mm$.

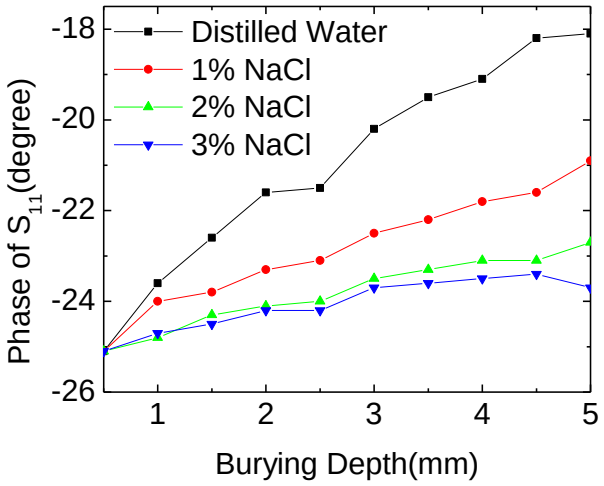

Figure 2.16: The phase due to the presence of the aluminum block in different testing media at maximum sensitivity.

2.4.4 Ground chicken experiments

To continue testing the proposed SRR probe in lossy medium, the biological tissue, ground chicken is considered for potential applications in food industry, such as food quality assurance [98]. The ground chicken was placed in a lexman box whose thickness is about $0.8mm$. The probe is placed underneath the box less than $1mm$ away, as demonstrated in 2.17(a). Before moving the aluminum cube close to the probe, ground chicken with desired thickness needed to be pressed to have a smooth surface for sliding the aluminum cube hanged over the chicken layer. The probe was calibrated to the new resonance frequency after the prepared box was positioned on top of the probe with a standoff distance less than $1mm$ between the SRR and the bottom of the box. An aluminum cube with size of $6.24mm$ was used as the sensing target, and the phase changes were recorded while the cube was moved laterally. A phase change of 15° was observed (Fig. 2.17(b)) with respect to the phase detected when the cube was moved away from the probe.

2.5 Conclusion

A near-field probe made of a single SRR and a rectangular loop that serves as the excitation source was proposed in this chapter. Numerical and experimental studies were conducted to analyze the performance of the probe in lossy saline water and ground chicken. Experimental results indicate that the SRR enhances the evanescent field strength stored in the near-field region of the probe, thus substantially improving the sensitivity of the probe in comparison to the probe without SRR. The effective standoff distance used in the experiments is a total of acrylic container bottom layer (i.e., $6.35mm$ in saline water experiment, and $0.8mm$ in chicken experiment) and air gap between the container and the probe (i.e., $1mm$ in saline solution experiment, and less than $1mm$ in chicken experiment). Compared to probes with sharp tip, the proposed probe is durable and low cost, which can be suitable

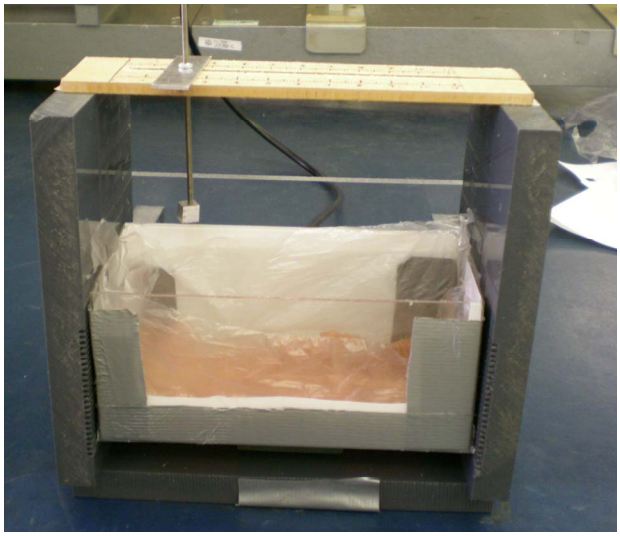

(a)

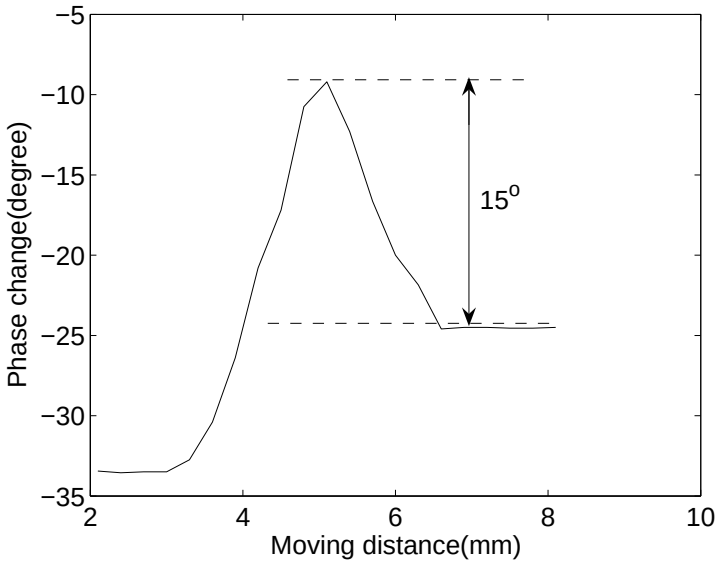

(b)

Figure 2.17: The experiment with the rectangular probe with SRR. (a) The system setups; (b) The phase change over the moving distance for 6.24mm cube and 2mm thickness of ground chicken.

in industrial applications.

Chapter 3

One Loop Resonator Probe

In previous chapter, characterization of SRR probe for sensing a small metallic cube inside loss controllable saline solutions and hidden behind lossy ground chicken was presented. Basically, the sensing concept used in this work is to perceive the variation in probe's S_{11} in the presence of an abnormality buried or hidden in host medium. Aforementioned sensing concept requires a more sensitive probe when detecting abnormality in complex and inhomogeneous host medium, for instance human tissue. In this chapter, a human breast tissue is being considered as the host medium. A more challenging abnormality - tumorous lesion - is embedded in the breast tissue at different locations. This study would be of great interests for early breast cancer detection.

3.1 Microwave breast abnormality detection modalities

Breast cancer is one of the most common types of cancer in women. According to the report by American Cancer Society in 2010, the death rate caused by breast cancer in

women was as high as 19.2% [99]. Detection of breast cancer in its early stage, where the tumor size is mostly less than $2cm$, saves women's lives with a five year survival rate of 95% [100]. Screen-film mammography(SFM) is the only routinely used technology that has strong clinical evidence for effectiveness in breast cancer screening [101]. However, ionizing radiation from annually SFM increases the risk of developing breast cancer in women who are predisposed to this disease [102]. Ultrasound (US) is an inexpensive screening technique, whereas, the decision on identification of a lesion requires skilled radiologists and technologists [102]. Magnetic resonance imaging (MRI), as a diagnostic adjunct to SFM and US, has high sensitivity in breast imaging, but suggests a higher rate of false-positive than mammography [102], and is subject to large screening expenses. Early breast cancer detection requires non-ionized, periodic, cost-effective, and mass screening. This suggests microwave screening or sensing as an outstanding candidate in the early stage breast cancer examination.

Attempts on breast cancer imaging using microwave sensing are considerably extensive, including tomography [103, 104], holography [105], and radar techniques [104, 106]. Microwave tomography employs narrow-band scanning signals that transmit through the breast tissue to reconstruct the dielectric properties of the breast. It generally leads to ill-posed nonlinear inverse scattering problems [104, 107] which are computationally expensive but can be accurately simplified through linearizing approximations using priori knowledge of normal breast [108]. Microwave holography which is originally from electromagnetic holography [109, 110] utilizes delay of the transmitted signal to recover three dimensional locations of the significant scatters in the tissue. Theoretically, its resolution is not subject to the wavelength of the source but is limited by the signal to noise ratio of the received back-propagating waves [105, 109]. Radar technologies, in general, apply a wide band incident wave which reflects back from significant scattering surface to retrieve the structural profile from back-scattered waves in the breast rather than attempting to reconstruct the complete dielectric property profile [104, 111].

Amongst these approaches, tumors are identified by different responses of breast tissue to scattered field [104, 108], reflected field [112, 113] or tissue's dielectric properties [114]. With development of nanotechnology, there are also growing interests in microwave thermal therapy, such as microwave hypothermia and microwave ablation [115]. Due to structural complexity of human breast, most of the evaluations on previous techniques are limited to two dimensional or simplified breast models, resulting in insufficient involvement of physics on tissue-wave interaction from electromagnetics perspective. Therefore, the feasibilities of new ideas on microwave cancer detection or treatment techniques were not trivial to evaluate in realistic breast tissue. With advancement in numerical breast phantoms [106, 107, 116], microwave techniques started to have effective computational tools for evaluating new detection or treatment concept for breast cancer. A profound influence on development of numerical breast phantoms came from a latest study reported by Hagness group [117]. The phantom is an anatomically realistic three dimensional (3D) numerical model with accurate dielectric properties derived from T1-weighted MRI images using a piecewise-linear mapping method between MRI voxel intensity and dielectric properties. Aforementioned numerical phantom can be incorporated with individual microwave probe design in numerical simulation software, such as CST Microwave Studio where the dielectric properties of breast tissue are expressed by single-pole Cole-Cole parameters or approximated by single-pole Debye parameters at a wide band frequency [117]. These breast phantoms make numerical simulations more realistic in concept validation of microwave probe design.

3.2 Probing mechanism

Since most of the microwave detection techniques suffer from tissue dispersion at board frequency range [118], a narrow band sensing approach is proposed in this work. In this scenario, the feasibility of a new probing scheme is validated with the assistance of afore-

mentioned anatomically realistic breast tissue using full-wave numerical simulations. With the knowledge built on microwave near-field probes in Chapter 2, an electrically small narrow band probe will be presented, which is essentially a surface receiving coil in MRI [119]. A numerical breast phantom will be constructed. The detection capacity of the probe will be tested with a tumor ($5mm$ and $10mm$) embedded at different locations in the breast phantom.

3.3 Construction of numerical breast phantom

The MRI data of the breast phantom is obtained from the website of University of Wisconsin [117]. The breast ID number is 012204 in classification category II. The size of the phantom data file is approximately $33MB$ with voxel size of $0.5mm \times 0.5mm \times 0.5mm$. The actual number of tissue types in terms of dielectric constant in this breast phantom is 502259 (about $0.5MB$). Due to computational limitation, the dielectric constant was rounded into integer to reduce the number of tissue types. As a result, the number of tissue types was decreased to 64. Fig. 3.1 demonstrates the three-dimensional breast phantom (breast ID number: 012204) using CST Microwave Studio 2010. To mimic the tumor detection, $5mm$ and $10mm$ tumors are embedded into the normal breast phantom, respectively. The dielectric constant of the tumor is 50 with conductivity of $1s/m$. The position of the tumor is randomly selected since the interest here is to sense the change of S_{11} in the presence of a random tumor.

3.4 Sensing using narrow band probe

The narrow band probe is designed using a microstrip loop and four capacitors placed on the traces. This probe is essentially a surface receiving coil for MRI [119, 120]. The design

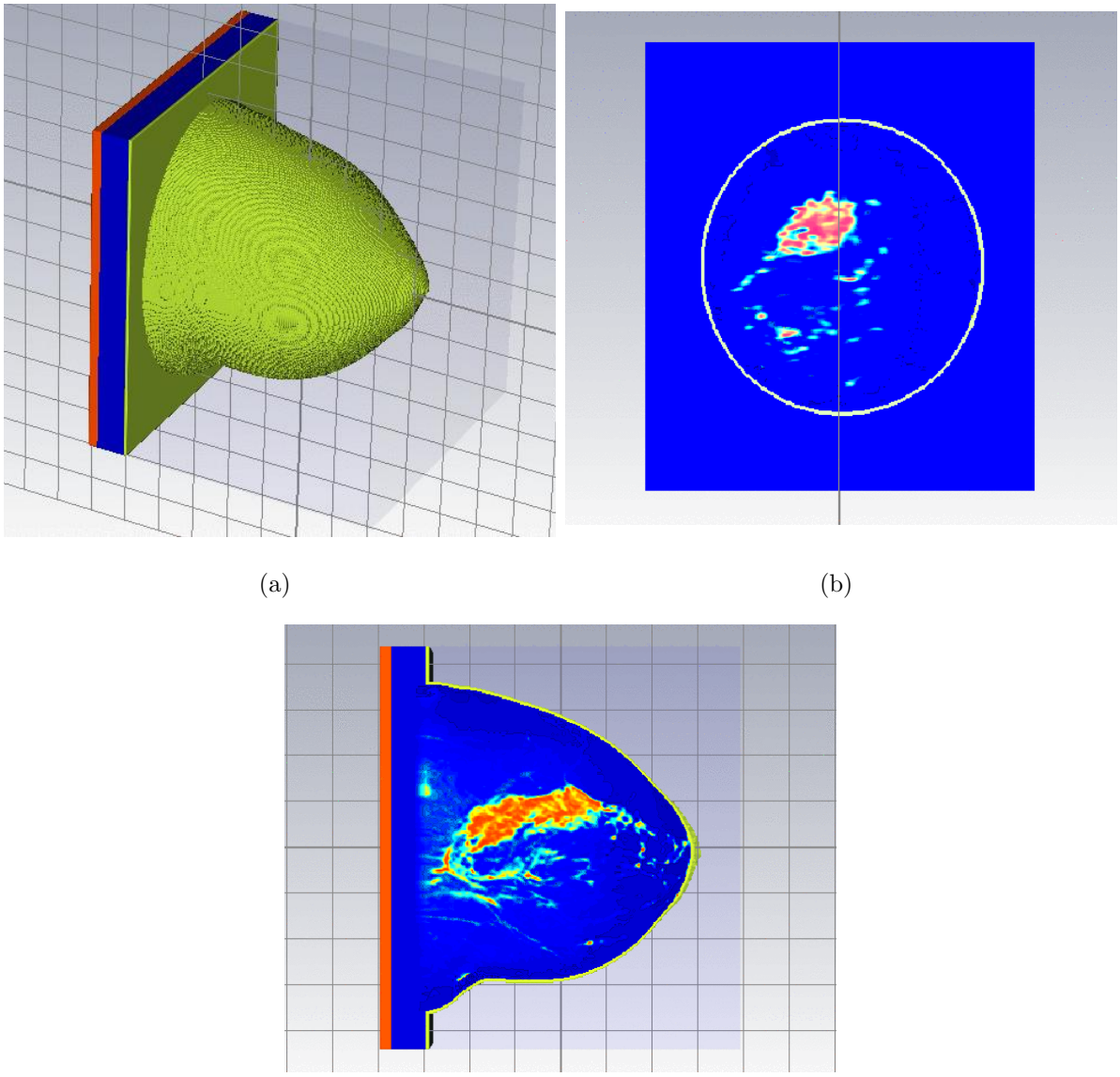

(a) (b)

(c)

Figure 3.1: The three-dimensional realistic numerical breast phantom model (breast ID: 012204) using CST Microwave Studio 2010. (a) Three-dimensional view. (b) X cross section. (c) Z cross section.

of the probe is demonstrated in Fig. 3.2. The dimension of the probe is $50.8mm \times 50.8mm$ with metallic trace width of $3.175mm$. The capacitors are placed in the cuts with size of $1mm$ in width. The capacitors on two flanked sides have the same capacitance of $8.2pF$. The one in parallel with the port has value of $67pF$. The other capacitor placed on the trace opposite to the port is $5.7pF$. Figure 3.3 represents the S_{11} of the unloaded probe. The simulated resonant frequency of the probe is measured at $293.5MHz$. The band width of $2.1MHz$ at $-3dB$ level.

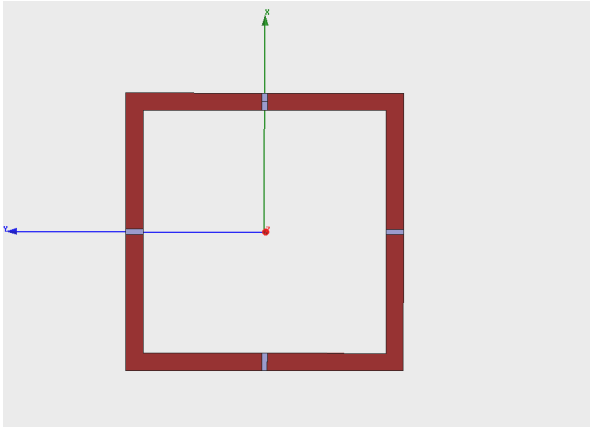

(a)

Figure 3.2: Narrow band antenna design.

$10mm$ and $5mm$ tumor were tested separately at five locations inside the breast phantom. The positions are abbreviated as P1-P5, respectively. Figure 3.4 and 3.5 illustrate the cross section of the breast phantom with different tumor locations for tumor size of $5mm$. Note that tumor locations and the tumor shapes are not the main detection interests, and these parameters are selected to demonstrate the feasibility of using a sensitive probe for detecting the presence of a small tumor embedded in a breast tissue.

Figure 3.6 and 3.7 represent the variation of probe's S_{11} due to $10mm$ and $5mm$ tumor, respectively. As shown in both figures, even with the $5mm$ tumor, the probe exhibits

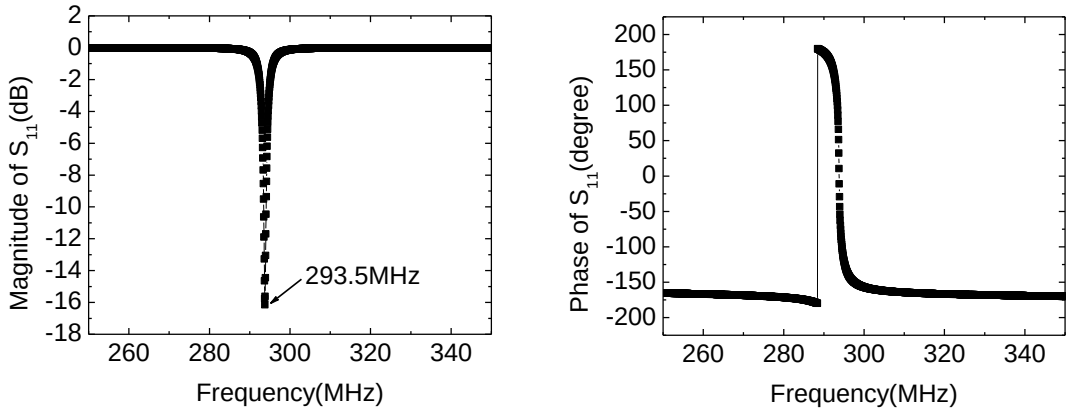

(a) (b)

Figure 3.3: S_{11} of unloaded probe. (a) Magnitude of S_{11} in dB. (b) Phase of S_{11} in degree.

approximately 6° phase change. Whereas, location information of $5mm$ tumor is basically indistinguishable, as the phase curves for position P1-P5 almost overlap to each other. The $10mm$ tumor yields appreciable variations in the phase when it's placed at different positions. Such variations are more than an order of magnitude larger than that of $5mm$ tumor.

The effect of standoff distance also is tested and shown in Fig. 3.8. Variations in magnitude of S_{11} are observed for different standoff distances, which is due to energy coupling between the probe and the tissue sample. To increase the coupling, some options, such as matching gels can also be considered in real applications in the future.

3.5 Discussion

In this chapter, an anatomically realistic human breast phantom was constructed. An electrically very small narrow band probe was presented to possibly detect the presence of a tumor with size of $5mm$ due to the permittivity, morphology, and location perturbation of

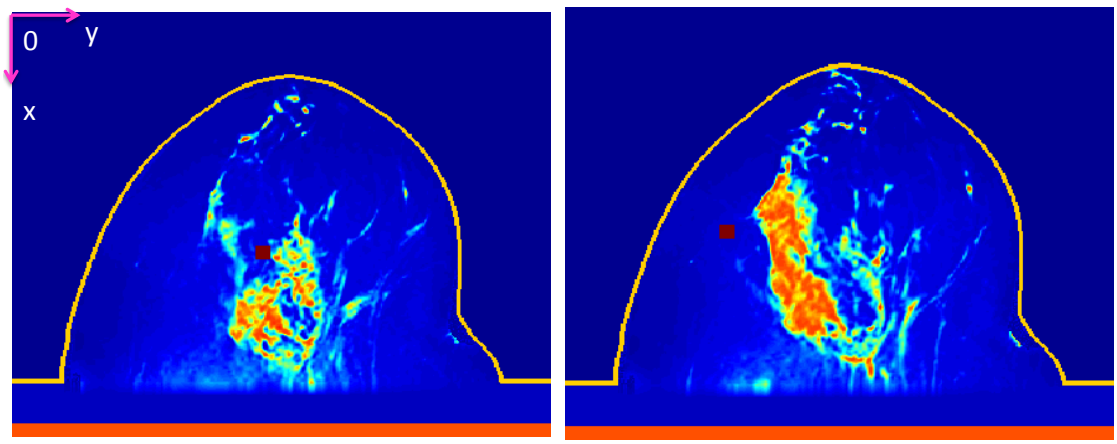

(a) (b)

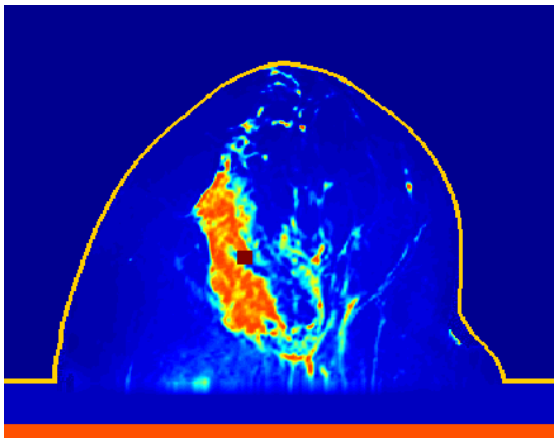

(c)

Figure 3.4: The tumor is located at random positions in the breast tissue with size of $5mm$. (a) Tumor located at P1 ($x = 90mm$, $y = 82.5mm$, $z = 82.5mm$). (b) Tumor located at P2 ($x = 82.5mm$, $y = 52.5mm$, $z = 77.5mm$). (c) Tumor located at P3 ($x = 92.5mm$, $y = 77.5mm$, $z = 77.5mm$).

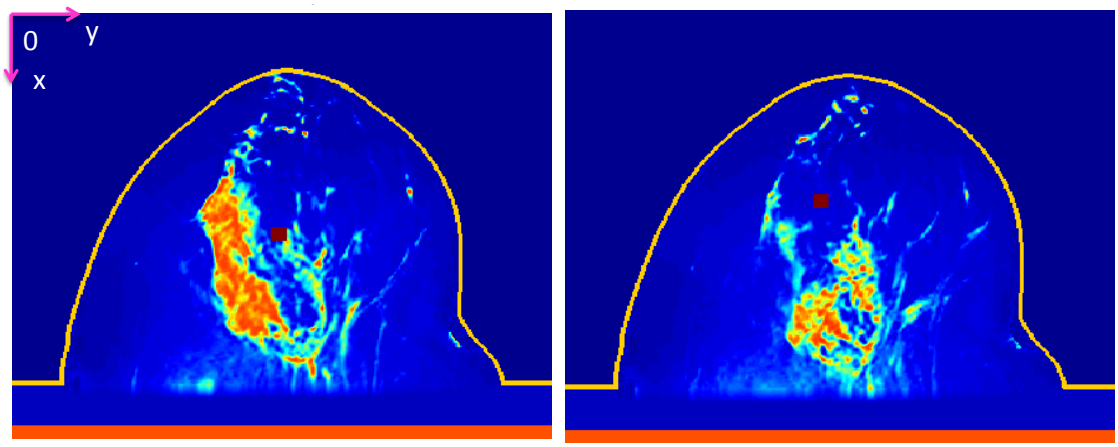

(a) (b)

Figure 3.5: The abnormality is located at random positions in the breast tissue with size of $5mm$. (a) Tumor located at P4 ($x = 82.5mm$, $y = 87.5mm$, $z = 77.5mm$). (b) Tumor located at P5 ($x = 70mm$, $y = 82.5mm$, $z = 82.5mm$).

the tumor to the normal tissue. However, the location perturbation is not often appreciable in terms of probe's S_{11} due to the complex wave-tissue interactions within the breast. This problem in tumor detection using a loop resonator can be tackled after introducing the technique of using LMS resonant particles as tumor marker. The sensing theory will be proposed in the future work.

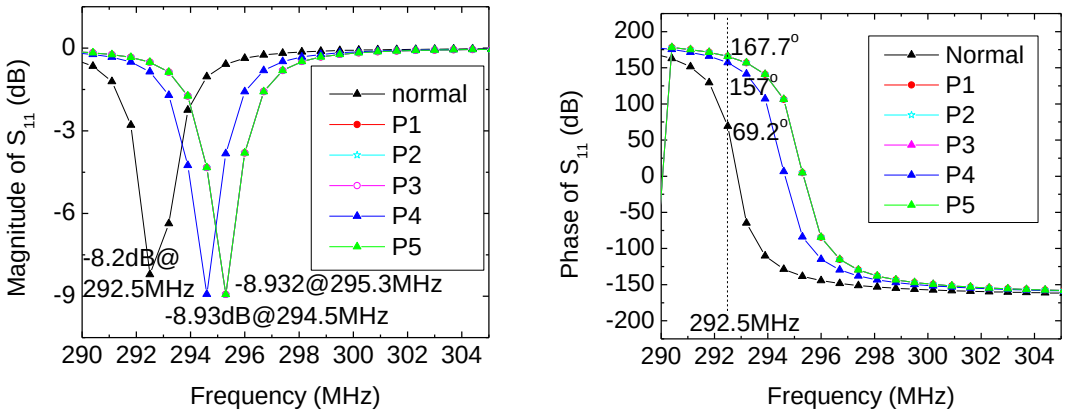

(a) (b)

Figure 3.6: Variations in probe's S_{11} before and after the $10mm$ tumor is embedded at different positions. Tumor locations are P1 ($x = 82.5mm$, $y = 52.5mm$, $z = 52.5mm$), P2($x = 82.5mm$, $y = 52.5mm$, $z = 77.5mm$), P3($x = 90mm$, $y = 82.5mm$, $z = 82.5mm$), P4($x = 82.5mm$, $y = 87.5mm$, $z = 77.5mm$), and P5($x = 70mm$, $y = 82.5mm$, $z = 82.5mm$). (a) Magnitude of S_{11} in dB. (b) Phase of S_{11} in degree.

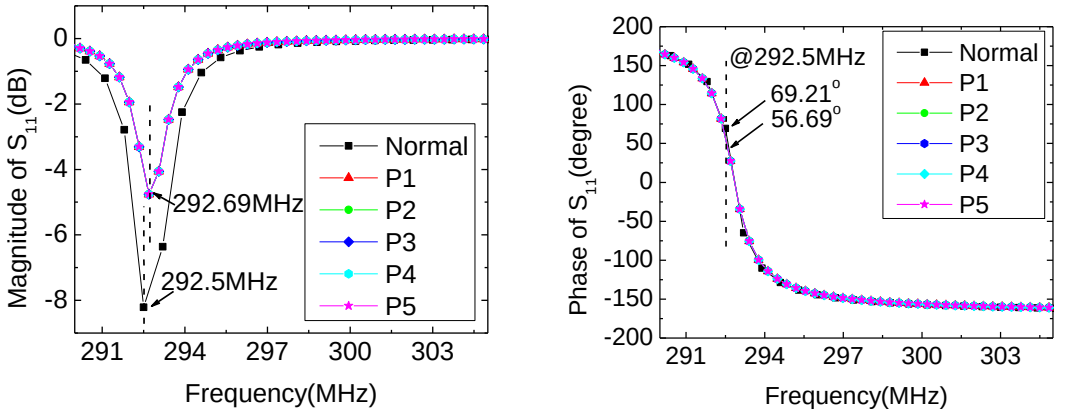

(a) (b)

Figure 3.7: Variations in probe's S_{11} before and after the $10mm$ tumor is embedded at the same five different positions as enumerated in the caption of Fig. 3.6.

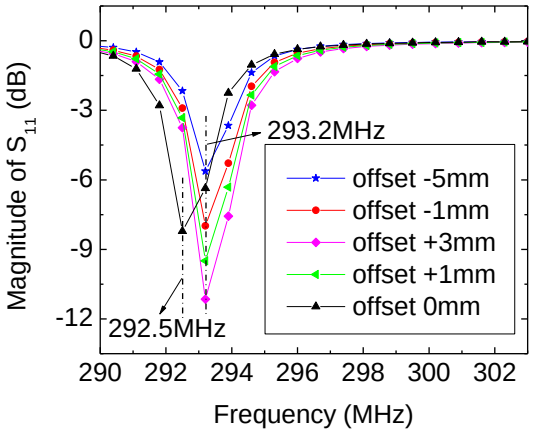

Figure 3.8: Probe response in magnitude of S_{11} at different standoff distance. "-" represents moving away from the tissue; "+" represents moving forward to the tissue. $0mm$ is corresponding to a distance of $2.5cm$ measured from the loop plane to the top of the normal breast tissue.

Chapter 4

Two Loop Resonator Probe

Having presented the SRR probe in Chapter 2, one can observe that such probe as an open resonator may be also sensitive to a magnetic perturbation due to the exposure of the magnetic flux created by the loops. To further confine the magnetic field concentration of the probe to smaller region, a miniaturized probe design will be proposed in this Chapter, designated as two loop resonator probe. The miniaturized design can be applied to detect localized magnetostatic surface (LMS) resonant particles, as resonant magnetic particles have many attractive possibilities in biomedicine and biomedical engineering, such as cell selection [121], drug delivery [122], and contrast agent [123].

The conventional magnetic markers used in aforementioned areas are commonly ferromagnetic, ferrimagnetic or superparamagnetic particles with size from a few nanometers to micrometers such that they can approach to different dimensions of biological entities such as a cell, a virus, a protein, or a gene [124]. Since these magnetic particles have magnetism forms of paramagnetism or superparamagnetism (in order of tens of nanometers or less), their movements can be under control in an external magnetic field. In cell separation or selection, wanted cells are labeled by ferro/ferrimagnetic nanoparticle or microspheres in biomaterial solutions or flows. The labeled cells can be collected by

applying static magnetic field or magnetic field gradient to the target media. The rest solutions can be therefore removed or flushed away [121, 124]. Similarly, in drug delivery, magnetically labeled drug carriers can be concentrated to the target lesion under external magnetic field gradient and ensure the effectiveness of the drug therapy [122, 124]. Some magnetic particles also have been used as contrast enhanced agent in magnetic resonance imaging (MRI) [123, 124], such as commercially available superparamagnetic nanoparticles. The underlying principle of contrast enhancement in MRI is that the presence of magnetic particles in pathologic tissue induces the local variations of magnetic susceptibility of the system, affecting the dephasing and shortening the spin-spin relaxation time, thus it can be effectively distinguished from normal tissue [123]. Another important application of conventional magnetic makers is artificially induced hypothermia. Magnetic particles can resonantly react to time-varying magnetic field, yielding thermal effect in local pathologic tissue. For instance, heating energy can be magnetically induced from the hysteresis property of ferromagnetic or ferrimagnetic (FM) particles under varying magnetic field [125]. The heat can be also transferred due to particle's Brownian rotation and atomic Néel process within individual particles whose size is under FM ones due to superparamagnetism [124, 125].

LMS resonant particles may considered as another class of magnetic markers, as the magnetostatic resonant behavior would yield many potential applications. Possible applications will be proposed in Chapter 5 at the end of this dissertation work. In this Chapter, the focus is on constructing of a magnetic sensitive probe to detect electrically very small LMS resonant particles as mentioned in the beginning of this Section.

As stated in Section 1.2.2, LMSR occurs to electrically very small volume having negative real permeability. The previous work on LMSR [36] was proposed to find the eigen modes of an isotropic arbitrary shape volume under magnetostatic condition $\nabla \times H = 0$. The eigen modes were excited in premise of a particle with negative real permeability. To simplify the previous problem in finding the value of negative real permeability due

to specific geometry, spherical or ellipsoidal shapes are considered, as the values can be attained from those of electrostatic resonance using EM duality. Details on permeability dependent resonant condition will be listed in Appendix B. Using the negative permeability values found for resonance, visualization of LMSR will be demonstrated for an isotropic resonant sphere, leading to observation of energy confinement and strong scattered field in its close vicinity. By placing such a sphere in the center of the two loop resonator, the strong magnetic confinement at LMSR would increase the magnetic flux through the loops, leading to current alternations in the loops. This near-field coupling of the two loops will be formulated using linear transformer theory. The inductance changes due to the presence of the sphere will be solved using magnetostatic boundary condition at the sphere surface. The LMSR detection mechanism based on inductance variations will be expounded. A two resonance detection signature will be presented with full-wave numerical validations. This mechanism is expandable to other LMS resonant shapes, such as disks. Numerical simulations and experimental verifications will be presented for disk shapes.

4.1 Field demonstration of LMSR in isotropic spheres

To further observe magneto-static resonance in subwavelength forms, such as spheres, analytical solutions are formulated to demonstrate this phenomenon, as the formulation of the solutions can be obtained from Mie theory that have been considerably used to study small particle scattering. The solutions are presented in terms of scattering coefficients (a_n, b_n) and absorption coefficients (c_n, d_n). Details are elaborated in Appendix A along with the ones for coated spheres. From the expressions of the scattering and absorption coefficients, the LMSR conditions can be derived to find the required negative real permeability. These conditions are obtained for a single sphere and a sphere with coating as expressed in Eq. (A.22) and Eq. (A.23) in Appendix A.

Figure 4.1 demonstrates the LMSR of a single sphere with diameter of $1.4mm$, approximately $\lambda/185$, where $\lambda = 258.6mm$ is the wavelength in free space, corresponding to $f = 1.16GHz$. The sphere's relative permeability is -2, calculated from $\mu_1 = -2\mu_b$ (Eq. (A.22)), where μ_b is the permeability of the surrounding medium. In Fig. 4.1, the surrounding medium is assumed to be vacuum. Some magnetic loss of $0.1i$ was also considered. The enhanced scattered field and confined magnetic field are observed. As expected, the magnetic field inside the sphere is uniform ($\nabla \times H = 0$).

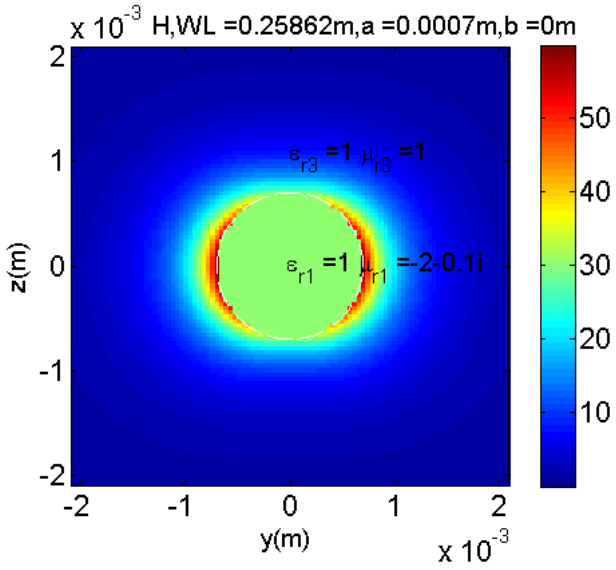

Figure 4.1: Scattered and internal magnetic field distribution for sphere in $y0z$ plane.

4.2 Probe design idea

From circuit point of view, SRR probe resonance (f) is determined by the self and mutual inductance (L) of the loops and the distributed capacitance (C) created by the parallel loop planes, $\omega = 2\pi f = 1/\sqrt{LC}$. To further shrink the loop area from SRR probe design, while

keeping the resonance at relatively low frequency, the capacitance is expected to increase to a desired value. Therefore, a capacitor is introduced to miniaturize the loop size. The capacitor is placed in the top SRR gap to replace the distributed capacitance created by the bottom one as shown in Fig. 4.2, adding the ability in selection of operation frequency. This new probe is a one-port device that consists of two printable concentric loops on a dielectric substrate as illustrated in Fig. 4.2.

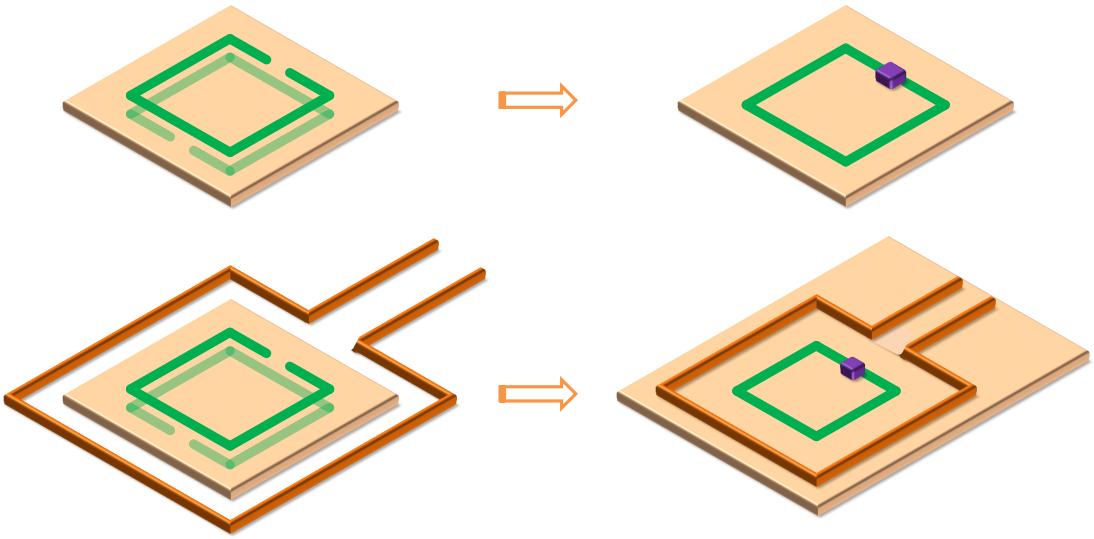

Figure 4.2: The idea of a two loop resonator.

4.3 Probe design

To maintain higher quality factor, the square shapes are still adopted. Figure 4.3 demonstrates the probe dimensions. The sizes of the outer and inner loop are $W_1 = 12mm$ and $W_2 = 7mm$. The loops' trace widths are $d_1 = 0.5mm$ and $d_2 = 0.2mm$. Copper lands dimensions are $d_3 = 1mm$ in width and $d_5 = 1.1mm$ in length, and their spacing d_4 is $1mm$. The spacing between feeding line of excitation loop is labeled as $d_6 = 2mm$. The

substrate used here is Rogers Duroid 5880. A hole with radius of $R_2 = 1mm$ is carved within the substrate to hold the sensing target at the center of the loops.

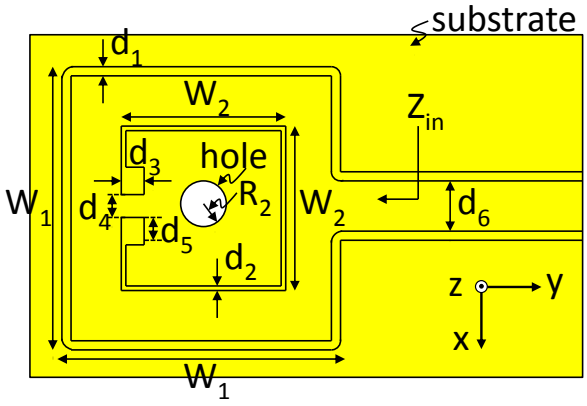

Figure 4.3: Design of two loop resonator probe.

To detect particles in order of a few millimeters or even smaller, the above probe size can be further miniaturized. The corresponding new dimensions are described in the same notations with different values. The new sizes of the outer and inner loop are $W_1 = 4mm$ and $W_2 = 2mm$. The new loops' trace widths are $d_1 = 0.462mm$ and $d_2 = 0.1mm$. The soldering pad are shrank to $d_3 = 0.5mm$ and $d_5 = 0.35mm$, their spacing d_4 is $0.3mm$. The feeding line gap d_6 is $0.2mm$.

4.4 Theoretical model

To understand the near-field coupling of the loops and ensure maximum energy transfer from the feed to the probe, I proposed a circuit model of the two loop resonator probe using linear transformer theory. From circuit perspective, the outer loop of the probe behaves as an excitation source while the inner one acts as a resonator whose capacitance can be tuned or selected. The probe resonance is created by the capacitor and the self and mutual

inductances of the loops. The source energy can be effectively transferred from the feeding loop to the inner loop through proper mutual inductive coupling between the two loops. This near-field coupling can be explained by the proposed circuit model in Fig. 4.4(b), where the loop self and mutual inductances are denoted as L_1, L_2 and M. The Ohmic losses for the loops are designated as R_1, R_2, and the currents flowing in them are labeled with I_1 and I_2.

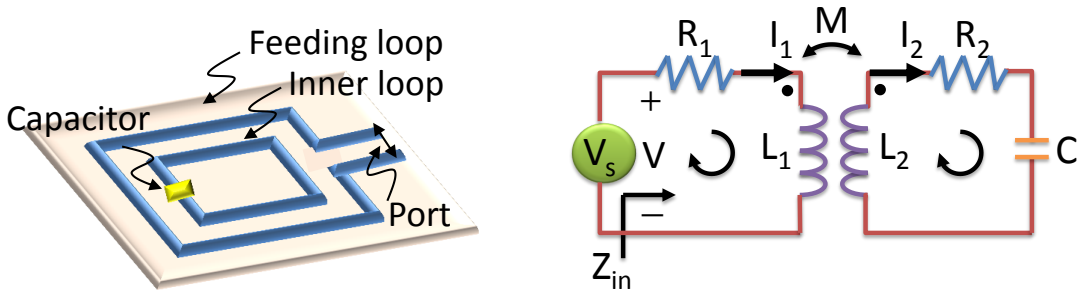

(a) (b)

Figure 4.4: Circuit model of two loop resonator probe. (a) Probe composed of two concentric loops. (b) Probe mutual inductive coupling model.

The size of the probe can be made very small compared to the wavelength, producing highly confined magnetic field within the small region surrounding the loops. Due to small size feature, quasi-static approximation can be used to calculate the loop inductances L_1, L_2 and M. Henceforth, the probe's input impedance, Z_{in}, can be derived as

$$Z_{in} = R_1 + j\omega L_1 + \frac{\omega^2 M^2}{R_2 + j\omega L_2 + (j\omega C)^{-1}} \tag{4.1}$$

where ω is the angular frequency of interest. The reflection coefficient is then calculated as $S_{11} = (Z_{in} - Z_s)/(Z_{in} + Z_s)$, where Z_s is the source impedance (probe's input impedance). To ensure effective coupling, the loop dimensions and their spacing can be optimized.

4.5 Applications in detecting LMSR

Employing the proposed miniaturized probe to LMSR is of importance due to the fact that few magnetic sensors work at room temperature in giga hertz in the literature. Magnetic sensitive sensors mainly contain but not limited to Superconduction Quantum Interference Device (SQUID), fluxgate magnetometer, Hall-effect magnetometer, and magnetoresistive devices. SQUID utilizes direct current (DC) or alternating current (AC) Josephson effect in superconductors [126,127]. Subtle change in external magnetic field [127,128] yields current inequality or variation in loop branches. This subtle change is captured by peripheral circuits at DC or AC frequencies. Micro-sized SQUID is applied in scanning microscopy to image magnetic strength on the surface due to its high sensitivity. Fluxgate magnetometer employs magnetization and demagnetization properties (B - H curve) of susceptible magnetic core. Such properties can be affected by the presence of an external magnetic field, leading to current mismatch in primary and secondary loops [129]. Hall-effect magnetometer measures high magnetic field via voltage difference across semiconductors or conductors. The voltage difference originates from imbalance electrons and holes accumulated at the edges of current carriers due to strong magnetic force [130]. Magnetoresistive sensor is made of some magnetic material whose electric resistance can be altered by applied magnetic field [131]. Such devices are massively produced as integrated circuits.

Amongst these magnetometers, SQUID is the most sensitive detector that measures magnetic field strength as low as 5 atto-Tesla. Commercially available SQUIDs are often operated at direct current or within the low microwaves regime [127,132]. However, SQUID system is bulky and costly because of its cooling system. Furthermore, high temperature SQUID is subject to high noise level [127]. Magnetometers are limited to measurements at DC or low frequencies fields due to temperature alternations [133], steady state requirement [130], or high frequency noise limitations [131]. Since few magnetic probes work at giga Hertz at room temperature, the two loop resonator proposed is of great importance

in LMSR detection.

4.5.1 Detection mechanism for isotropic Lorentzian dispersive sphere

When placing a magnetic sphere within the probe as seen in Fig. 4.5(c), the effective surrounding medium of the loops changes, leading to changes in the loop inductances. The magnetic perturbation leads to impedance change of the probe, as shown in Fig. 4.5(d). Such perturbation is most effective when the sphere's magnetic polarizability coincides with loop axis. The change in the loop inductances arising from the presence of the sphere, denoted as ΔL_1, ΔL_2 and ΔM in Fig. 4.5(d), can be calculated analytically (in spherical coordinate) assuming the inserted sphere is isotropic.

It's known that the self-inductance L can be represented by the integral of the magnetic vector potential Φ along a closed loop as $L_1 = \frac{\Phi_1}{I_1} = \frac{1}{I_1}\oint A_{\phi 1} \cdot dl_l$ [134]. In presence of an isotropic magnetic sphere with relative permeability μ_r concentrically placed inside the loop, as demonstrated in Fig. 4.6, the contribution to self inductance after insertion of the sphere can be represented in terms of different geometric contribution as $A_\phi + A_\phi^{1,2}$ according to the additivity of magnetic vector potential, where A_ϕ is the contribution due to the circular loop, and $A_\phi^{1,2}$ is the contribution due to the sphere, where the superscript $1, 2$ correspond to the region outside and inside the sphere, respectively. The magnetic vector potential due to a single circular loop concentric with a magnetic sphere is expressed as Eq. (4.2) for the region outside sphere, and as Eq. (4.3) for the region within the sphere [134].

$$A_\phi + A_\phi^1 = \frac{\mu_0 I \sin\alpha}{2} \sum_{n=1}^{\infty} \left[\frac{1}{n(n+1)} \left(\frac{r}{a}\right)^n + A_n \left(\frac{b}{r}\right)^{n+1} \right] P_n^1(\cos\alpha) P_n^1(\cos\theta) \quad (b < r < a) \tag{4.2}$$

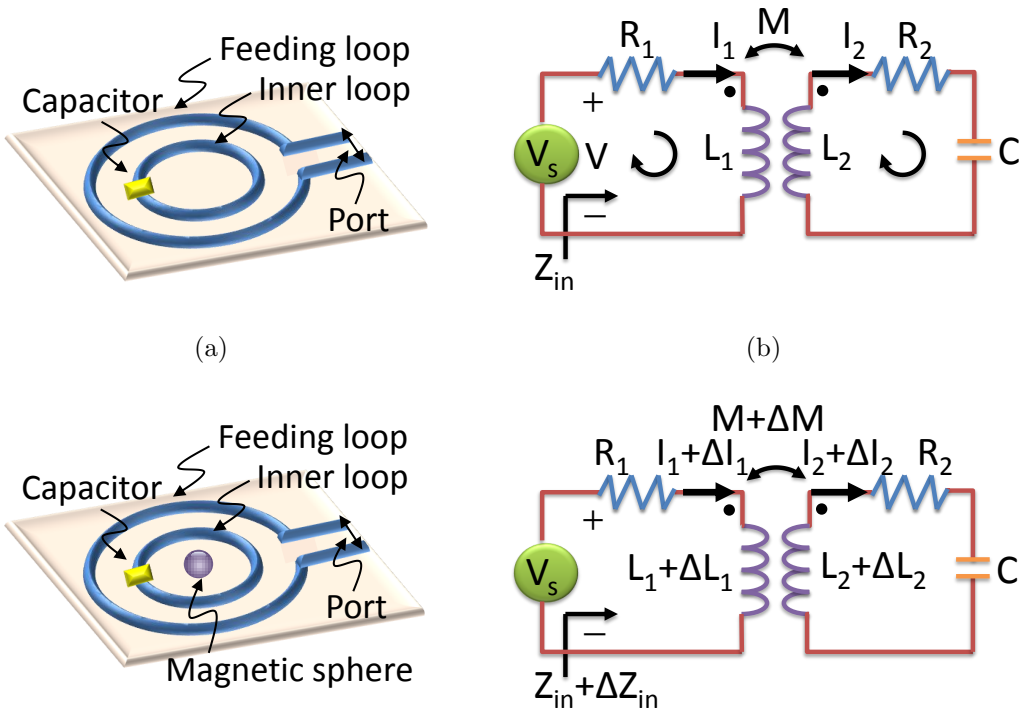

Figure 4.5: Detection mechanism. (a) Probe composed of two concentric loops. (b) Probe mutual inductive coupling model. (c) Probe loaded with magnetic sphere. (d) Parameter variations in mutual inductive coupling model.

$$A_\phi + A_\phi^2 = \frac{\mu_0 I \sin\alpha}{2} \sum_{n=1}^{\infty} \left[\frac{1}{n(n+1)} \left(\frac{r}{a}\right)^n + B_n \left(\frac{r}{b}\right)^n \right] P_n^1(\cos\alpha) P_n^1(\cos\theta) \quad (r < b) \quad (4.3)$$

where

- A_ϕ : magnetic vector potential of circular loop at any point (r, θ, ϕ)
- A_ϕ^1 and A_ϕ^2 : magnetic vector potential of the sphere at any point $(r > b, \theta, \phi)$ and $(r < b, \theta, \phi)$
- P_n^1 : legendre function of first order and degree n
- α : describes the position where the circular loop is located. If origin is at center of the loop, $\alpha = \pi/2$
- a_i,b : radius of circular loop and sphere
- $\left(\frac{b}{r}\right)^{n+1}$ and $\left(\frac{r}{b}\right)^n$: term outside the sphere and term inside the sphere
- A_n and B_n : coefficients
- μ_0 is the permeability in vacuum

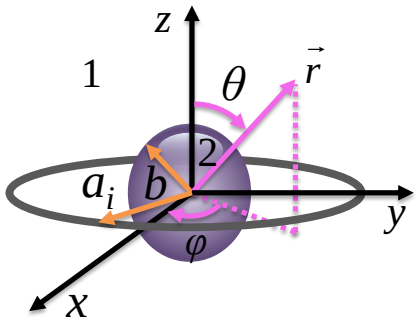

Figure 4.6: Sphere concentric with a circular loop.

Since the sphere is electrically very small, magnetostatic boundary conditions (BC) can be applied at the sphere surface where $r = b$.

B.C. I $\hat{n}\cdot(B_{b+}-B_{b-})=0$, so $B_n|_{b+}=B_n|_{b-}$. At the sphere's surface, the radial component of **B** is continuous.

B.C. II $\hat{n}\times(H_{b+}-H_{b-})=0$, so $H_t|_{b+}=H_t|_{b-}$. At the sphere's surface, the tangential component of **H** is continuous.

From BC I, the relationship between A_n and B_n reduces to

$$A_n = B_n \tag{4.4}$$

From BC II, the condition at the surface $r=b$ reduces to

$$(\mu_r-1)B_\theta+\mu_r B_\theta^1 = B_\theta^2 \tag{4.5}$$

Using

$$B_\theta = -\frac{1}{r}\frac{\partial}{\partial r}(rA_\phi) \tag{4.6}$$

The transverse magnetic field density can be calculated as

$$B_\theta = -\frac{1}{r}\frac{\mu_0 I\sin\alpha}{2}\sum_{n=1}^{\infty}\left[\frac{1}{n}\left(\frac{r}{a}\right)^n\right]P_n^1(\cos\alpha)P_n^1(\cos\theta) \tag{4.7}$$

$$B_\theta^1 = \frac{1}{r}\frac{\mu_0 I\sin\alpha}{2}\sum_{n=1}^{\infty}\left[nA_n\left(\frac{b}{r}\right)^n\right]P_n^1(\cos\alpha)P_n^1(\cos\theta) \tag{4.8}$$

$$B_\theta^2 = -\frac{1}{r}\frac{\mu_0 I\sin\alpha}{2}\sum_{n=1}^{\infty}\left[(n+1)B_n\left(\frac{r}{b}\right)^n\right]P_n^1(\cos\alpha)P_n^1(\cos\theta) \tag{4.9}$$

Substituting the expressions of transverse magnetic field density into Eq. (4.5), the second relationship of A_n and B_n can be obtained as

$$\mu_r n A_n = (\mu_r-1)\frac{1}{n}\left(\frac{b}{a}\right)^n-(n+1)B_n \tag{4.10}$$

Combining Eq. (4.4) and Eq. (4.10), the coefficient A_n and B_n can be derived as follows.

$$A_n = B_n = \frac{\mu_r-1}{n(n\mu_r+n+1)}\left(\frac{b}{a}\right)^n \tag{4.11}$$

Therefore, the self-inductance due to the presence of the sphere can be calculated from A_ϕ^1 by substituting A_n.

$$\Delta L = \frac{1}{I} 2\pi a A_\phi^1 \big|_{r=a_i}^{\alpha=\theta=\pi/2} \tag{4.12}$$

Therefore, the self-inductance change of the two loops can be expanded from Eq. (4.12) as

$$\Delta L_i = \sum_{l=0}^{\infty} \frac{\pi \mu_0 (\mu_r - 1)(2l+2)^2 b^{4l+3} \left[\frac{(2l+1)!!}{(2l+2)!!}\right]^2}{(2l+1)[(2l+1)\mu_r + 2l + 2] a_i^{4l+2}} \tag{4.13}$$

where a_i represents the radius of two different loops ($i = 1, 2$ for the outer and inner loops, respectively). $(2l+1)!! = 1 \cdot 3 \cdot 5 \cdots (2l+1)$ represents the factorial of odd numbers, and $(2l+2)!! = 2 \cdot 4 \cdot 6 \cdots (2l+2)$ corresponds to the factorial of even numbers.

Next, the calculation of the change in the mutual inductance is presented. In spherical coordinates, the mutual inductance M of two loops concentric with an isotropic magnetic sphere shown in Fig. 4.7, is expressed by the integrals of the ϕ component of the magnetic vector potential caused by loop 1 along the closed path of loop 2 as $M_{12} = \frac{\Phi_{12}}{I_1} = \frac{1}{I_1} \oint A_{\phi 1} \cdot dl_2 = \frac{1}{I_2} \oint A_{\phi 2} \cdot dl_1 = M_{21}$ [134].

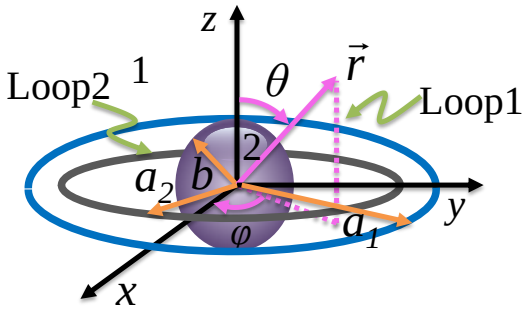

Figure 4.7: Sphere coaxial with two circular loops.

The change in the mutual inductance ΔM can be calculated from A_ϕ^1 (similarly to the above derivation) as

$$\Delta M = \frac{1}{I} 2\pi c A_\phi^1 \big|_{r=a_1}^{\alpha=\theta=\pi/2} \tag{4.14}$$

and expanded to

$$\Delta M = \sum_{l=0}^{\infty} \frac{\pi\mu_0(\mu_r - 1)(2l+2)^2 b^{4l+3}\left[\frac{(2l+1)!!}{(2l+2)!!}\right]^2}{(2l+1)[(2l+1)\mu_r + 2l + 2](a_1 a_2)^{2l+1}} \tag{4.15}$$

Note that ΔL_i and ΔM are size dependent. If the sphere is very small at probe operation frequency, it can be considered as a magnetic dipole. Then change in the inductance can be approximated using the leading term of the series in Eq. (4.16) and Eq. (4.17).

$$\Delta L_i = \pi\mu_0 \frac{\mu_r - 1}{\mu_r + 2} \frac{b^3}{a_i^2} \tag{4.16}$$

$$\Delta M = \pi\mu_0 \frac{(\mu_r - 1)b^3}{(\mu_r + 2)a_1 a_2} \tag{4.17}$$

Occurrence of LMSR in the sphere requires satisfying the equality $\mu_r = -2$ as stated in Section 4.1, where the surrounding medium is vacuum with relative permeability of 1. This equality yields a singularity in ΔL_i and ΔM causing S_{11} to approach unity. Therefore, under such equality, the probe exhibits open circuit behavior for non-dispersive magnetic isotropic LMS resonant spheres, since Z_{in} becomes infinite at each frequency according to Eq. (4.1). Notice that such possibility, i.e., a constant negative permeability over a wide range of frequencies, is unrealistic. A more realistic scenario, however, is to assume the sphere to be magnetically dispersive. Even under the assumption of magnetic dispersion, S_{11} exhibits a similar singularity to the non-dispersive sphere case, however, this time the singularity and the resulting $|S_{11}| = 1$ occur at *only* the LMS resonant frequency point. Interestingly, for the dispersive magnetic sphere, the probe exhibits two resonances on each side of the LMSR. In fact, such outcome can be predicted from Eq. (4.1), Eq. (4.16) and Eq. (4.17) under the approximation that the loops' inductance, capacitance and resistance are constant with frequency over the bandwidth of interest.

Another important conclusion made by observing Eq. (4.16) and Eq. (4.17) is that such LMSR detection signature is not limited to spherical particles as long as non-spherical

particles exhibit maximum magnetic polarizability in the direction normal to the loops' plane. This is because the inductance changes expressed in Eq. (4.16) and Eq. (4.17) are proportional to the particle's magnetic polarizability expressed as $(\mu_r - 1)b^3/(\mu_r + 2)$. Nevertheless, to validate these analytical predictions and to provide a more accurate estimation of S_{11}, full-wave simulation is provided in Section 4.6.

4.6 Numerical results of LMSR detection

The full-wave simulation is performed using CST Microwave Studio 2012 for the probe design illustrated in Fig. 4.3 as an example for validation. Fig. 4.8(a) provides the corresponding $|S_{11}|$ for a $1pF$ capacitor. At the resonant frequency of $1.09GHz$, more than 94% of the power is delivered to the probe while only 0.5% of the power radiates, indicating that most of the power delivered to the probe is dissipated within the probe due to ohmic loss of the conductor and dielectric loss of the substrate.

Since the size of the inner loop is approximately $\lambda/39$ at its resonant frequency, the magnetic field within the center region of the probe is approximately uniform (quasi-static field behavior). The size of the sphere chosen is $1.4mm$ in diameter, approximately $\lambda/195$ at the probe's unloaded frequency. The sphere's dispersion is modeled using a Lorentz model. The LMS resonant frequency is selected to coincide with the probe's resonant frequency of $1.09GHz$, where the relative permeability of the sphere is set to $-2 - i0.00017$ (some small loss was inserted in order to provide a degree of realism). According to Eq. (4.1) and the definition of S_{11}, an open circuit behavior ($|S_{11}| = 1$) is expected at the LMS resonant frequency. This open circuit point, highlighted as solid circle in Fig. 4.8(b), is seen to be flanked by two probe resonances, the first at approximately $1.08GHz$ and the second at $1.12GHz$. LMSR is observed to occur precisely when the maximum of $|S_{11}|$ between two valleys (probe resonances) is reached. The value of this maximum is numerically measured

to be $-0.015dB$ at $1.093GHz$ (see Fig. 4.8(b)). The corresponding relative permeability at this maximum is $-1.96 - 0.00016i$, very close to the expected $-2 - 0.00017i$.

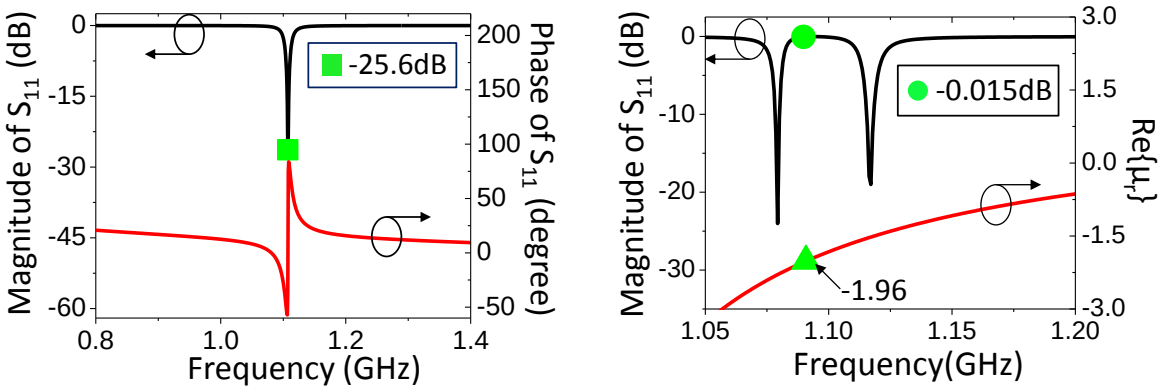

(a) (b)

Figure 4.8: Magnitude of S_{11} of the two loop resonator probe with and without sphere. (a) $|S_{11}|$ of the unloaded probe showing typical probe resonance behavior. (b) Two resonances surrounding the LMSR happens when the sphere with radius of $0.7mm$ is placed within the loops as in Fig. 4.5(c).

Next, the sphere's permeability profile is changed to shift the LMSR point ($Re\{\mu_r\} = -2$) away from the probe's resonant frequency. It can be observed that the open circuit point (highlighted with solid circle in $|S_{11}|$ curve) moves along with this LMSR point (highlighted with solid triangle in the $Re\{\mu_r\}$ curves), as shown in Fig. 4.9(a)-(c).

As the LMSR point moves further away from the probe's resonant frequency (the one without the presence of any sphere) to either lower frequency or higher one, the magnitudes of S_{11} of the two probe resonances are observed to depart from being equal. In fact, it is observed that as the LMSR shift either to the right (higher) or left (lower) from the original probe resonant frequency, the probe's resonance closer to the LMSR point will have lower dB magnitude than the second probe resonance, as shown in Fig. 4.9(d) and Fig. 4.10(a)-(b). If the LMSR point moves very far from the probe's original resonant frequency,

say at much higher frequency, then the probe's second (higher) resonance disappears, as demonstrated in Fig. 4.10(c)-(d). In other words, the probe does not yield any significant variation to non-resonant sphere having permeability other than $Re\{\mu_r\} = -2$.

According to above analysis and observations, it can be concluded that the two resonances in S_{11} profile, as shown in Fig. 4.9 and Fig. 4.10(a)-(b), can be used as an LMSR detection signature for spheres with small loss. The numerical simulation for a sphere with higher magnetic loss of $0.07i$ at probing frequency $1.09GHz$ was also conducted, similar behavior to the case with smaller loss was observed as shown in Fig. 4.11, which again demonstrates that the two resonance phenomenon can be considered as a signature for LMSR detection.

Another interesting observation is also made by plotting the magnetic field vectors within the sphere for each of the two resonant frequencies. The magnetic field vectors in the y-z planes that intersect the sphere right in the middle are shown in Figure 4.12(a) and (b) are for the lower and higher probe resonance frequencies, respectively (the frequencies and sphere dimensions are given in the figure caption). At the second resonant frequency, the magnetic field inside the sphere is enhanced in the same direction as that of the surrounding field, whereas at the probe's lower resonant frequency, the magnetic field inside is enhanced in the opposite direction.

As mentioned previously, two resonance behavior of S_{11} may possibly occur to other shapes. Here disk shape particles are also taken into account in numerical validations. The dimension of the disk is $0.508mm$ in diameter and $0.127mm$ in height. A little magnetic loss is added such that at open circuit point the corresponding magnetic loss is approximately $0.016i$. At the same point, the real permeability is -1.97 (a negative value).

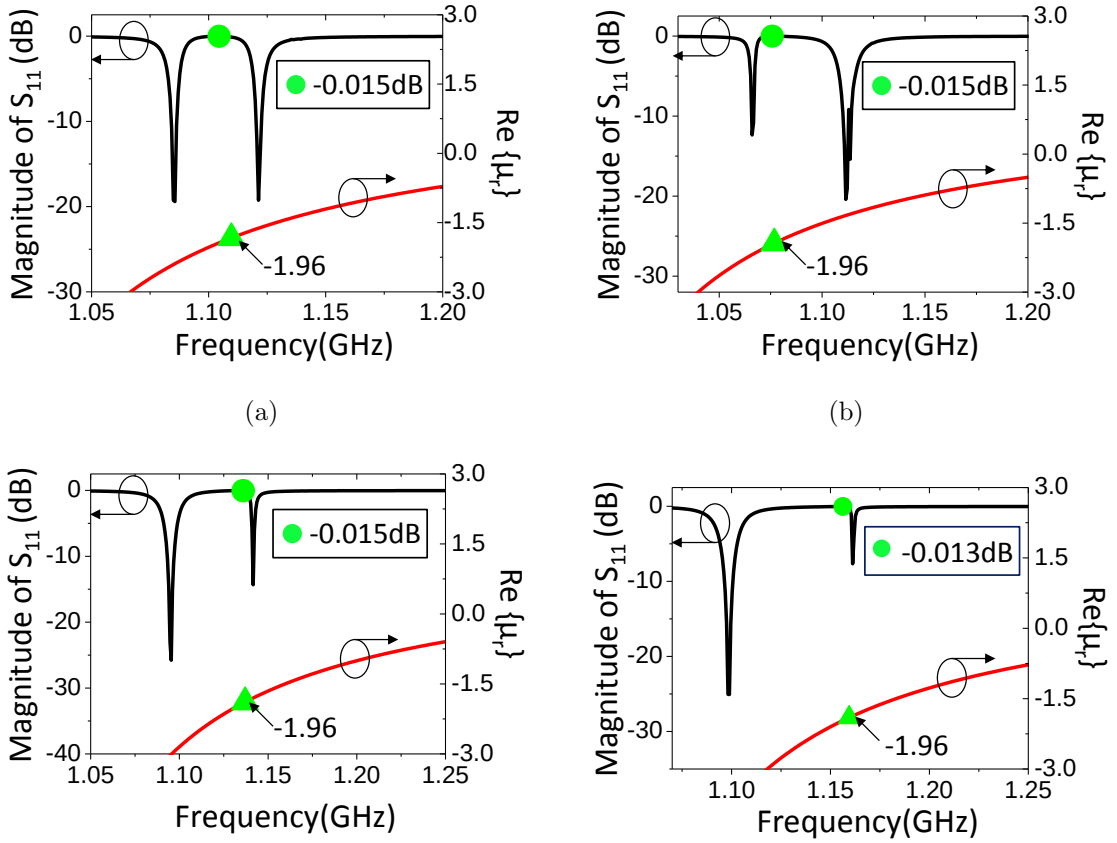

Figure 4.9: Magnitude of S_{11} for detection of low loss LMS resonant sphere under different permeability profiles. Values of open circuit point and the corresponding $Re\{\mu_r\}$ are presented in (a)-(d) where two resonance are prominent. The size of the sphere is $0.7mm$ in radius.

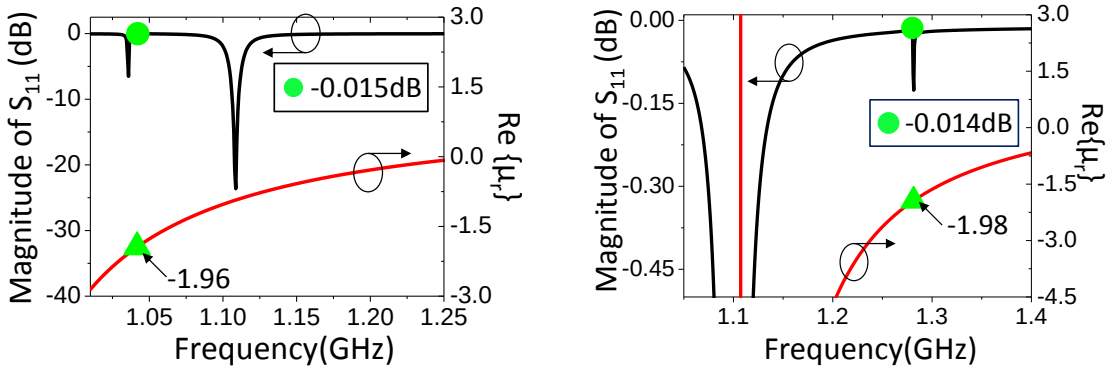

Figure 4.10: Magnitude of S_{11} for detection of low loss LMS resonant sphere under different permeability profiles. Values of open circuit point and the corresponding $Re\{\mu_r\}$ are presented in (a)-(b). (c) and (d) are obtained when permeability point $Re\{\mu_r\} = -2$ moves out of monitoring frequency range ($1GHz$ to $1.3GHz$). The size of the sphere is $0.7mm$ in radius.

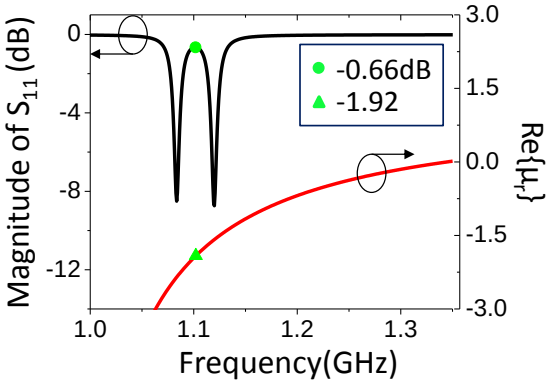

(a)

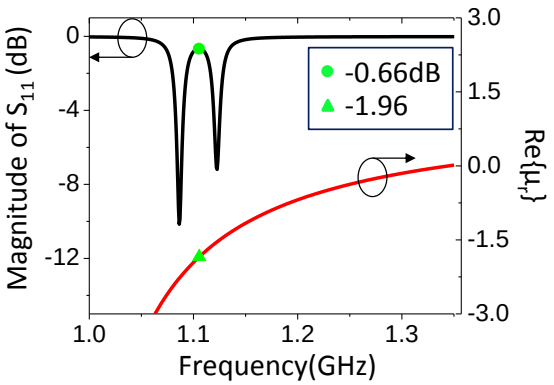

(b)

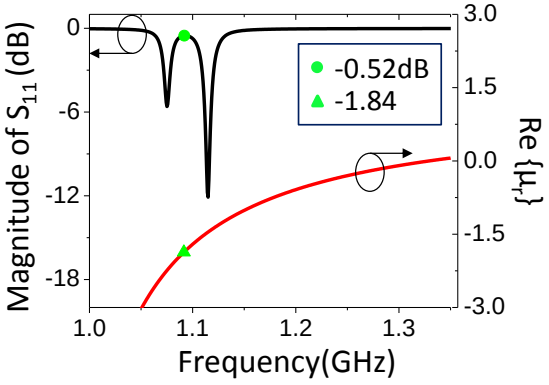

(c)

Figure 4.11: Magnitude of S_{11} for lossy LMS resonant sphere under different permeability profiles. Values of open circuit point and the corresponding $Re\{\mu_r\}$ are presented in (a)-(c). The size of the sphere is $0.7mm$ in radius.

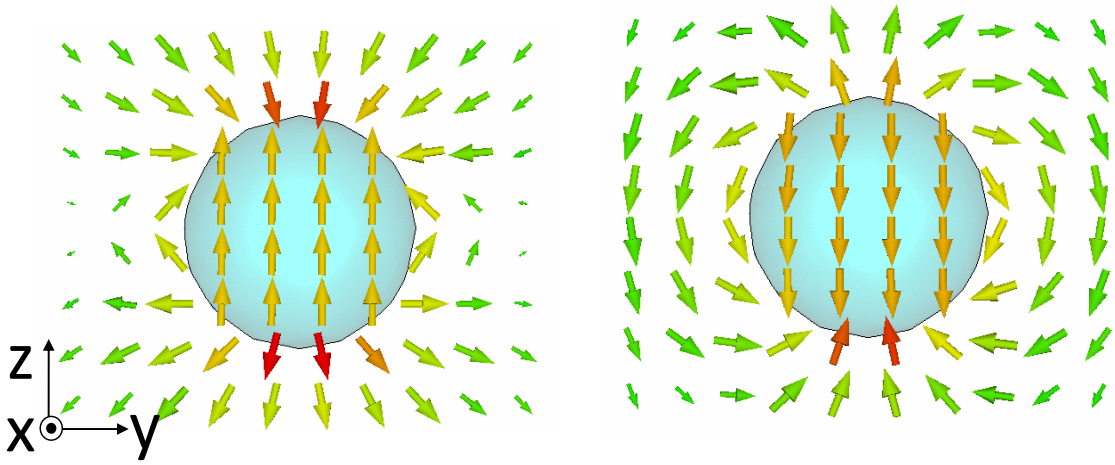

(a) (b)

Figure 4.12: Magnetic field vector distribution on the x=0 plane. (a) Magnetic field vector plot at first resonant frequency $1.09GHz$ with sphere radius of $0.7mm$. (b) Magnetic field vector plot at second resonant frequency $1.12GHz$ with sphere radius of $0.7mm$. (Substrate and color map have been hidden for clear demonstration of field vectors. Redness and blueness represents maximum positive and negative magnetic field magnitude, while greenness represents minimum magnetic field magnitude.)

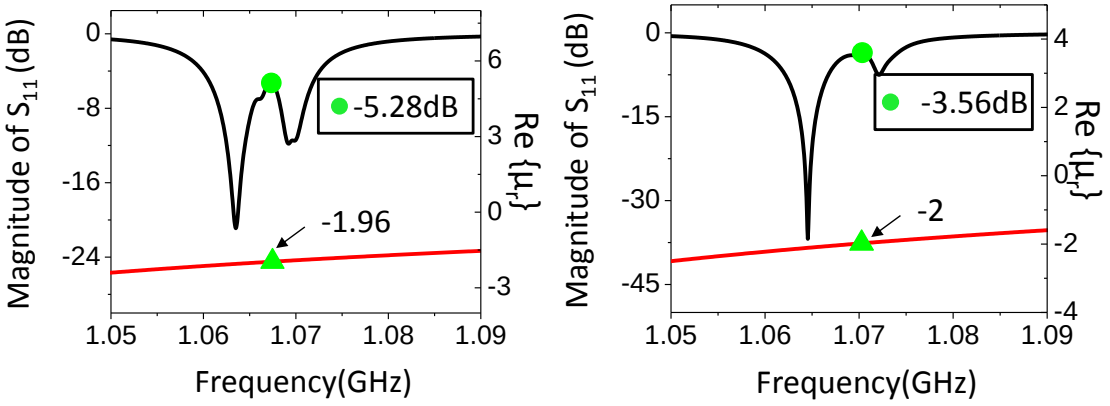

(a) (b)

Figure 4.13: Magnitude of S_{11} in dB for the lossy LMS resonant disk under different magnetic dispersion profile. Values of open circuit point and the corresponding $Re\{\mu_r\}$ are presented in (a)-(b). The size of the disk is $0.508mm$ in diameter and $0.127mm$ in height.

4.7 Experimental results of electrically small particle having effective negative permeability

As stated in Chapter 1, state of the art metamaterial science provides possibilities for constructing artificial materials with *effective* negative permeability. Moreover, natural materials such as non-linear dielectric liquids demonstrates magneto-static behavior at discrete points along the surface at optical frequency [60, 61]. However, as pointed out in Chapter 1.2.2, liquid form particles are not trivial to construct. At microwave frequencies, some magnetic materials such as ferrites [63, 68], metallic grains [69] and films [62, 135] exhibit effective negative real permeability in principle directions different than the direction of the static bias field. Amongst these magnetic materials, yttrium iron garnet (YIG), a type of ferrimagnetic material, has demonstrated low magnetic loss under a static magnetic

bias field [62, 63].

The materials selected to demonstrate LMSR are polycrystalline YIG and polycrystalline calcium-vanadium substituted YIG (CVG). Similar garnets, gadolinum substituted garnets (GG), are also selected to demonstrate the nonoccurrence of LMSR due to positive real permeability at the probing frequency. In the following sections, different materials will be characterized in coaxial air line and tested using proposed two loop resonator probe with smaller dimension (inner loop size is 2 mm) described in Section 4.5.

4.7.1 Material characterization

The materials used in the experiments contain commercially available YIG (linewidth$\leq$25 o.e., dielectric loss tangent$<$0.0002), CVG (linewidth$\leq$10 o.e., dielectric loss tangent$<$0.0002), and GG (linewidth$\leq$300 o.e., dielectric loss tangent$<$0.0002) from TransTech (Adamstown, MD, USA). To fit the bulk material into coaxial air line, the materials were ordered in shapes of toroid. The outer radius of the toroid is 3.5mm, and the inner one is 1.5mm. The toroid was placed at specific location inside coaxial air line, and characterized under static magnetic field as demonstrated in Fig. 4.14.

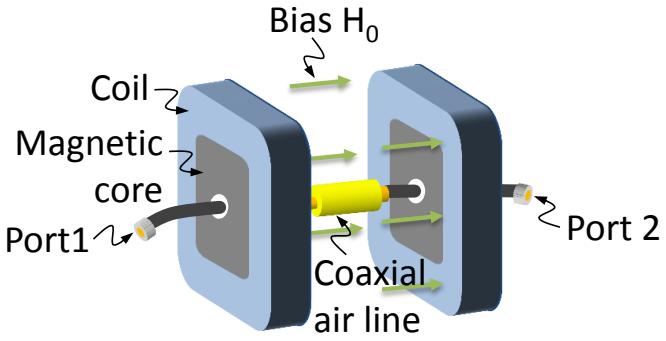

Figure 4.14: Bulk material characterization using coaxial air line

The static magnetic field was generated by a helmholtz coil composed of two coaxially

aligned solenoids and magnetic cores shown in Fig. 4.14. The coaxial air line was placed in the center between two coils such that the static magnetic bias field was parallel to the direction of the microwave propagation. The effective relative permeability (μ_r) was extracted using transmission reflection method [136]. Figure 4.15(a) and (b) illustrate the extracted relative real permeability of YIG and CVG, respectively, where the real part of μ_r exhibits negativeness around the operation frequency of two loop resonator, $2.74GHz$. The S_{11} of the probe at this frequency will be presented in Section 4.7.2. Figure 4.15 (c) suggests that under static bias magnetic field from 400 o.e. to 1000 o.e. GG exhibit positive μ_r.

4.7.2 LMS resonant disk results

Due to some commercial fabrication limitation, the polycrystalline particles were made in disk shapes with diameter of $0.256mm$ and height of $0.127mm$. The probe design is completed with a slotline balun to compensate the imbalanced currents produced by coaxial feed as demonstrated in Fig. 4.18(a). The capacitor's value is $0.8pF \pm 0.1pF$. The inner square loop is $2mm$ wide, $\lambda/55.6$, where λ represents probe's operation frequency ($2.74GHz$). The trace width of the inner square loop is $0.1mm$. The outer square excitation loop is $4mm$ wide with trace width of $0.5mm$. The probe provides approximately uniform magnetic field in the center region of the inner loop due to quasi-static approximation. The probe's S_{11} demonstrates 91.3% energy delivery to the near-field at probing frequency of $2.74GHz$ as seen in Fig. 4.18(b).

Figure 4.17 depicts the configuration of the experimental setup. The small disk sits in the hole caved in the center of the the loops, such that the alternating field is in axial direction of the disk (normal direction of the circular surface). The static bias magnetic field is in perpendicular to the alternating field, forming negative permeability in the direction of the alternating field.

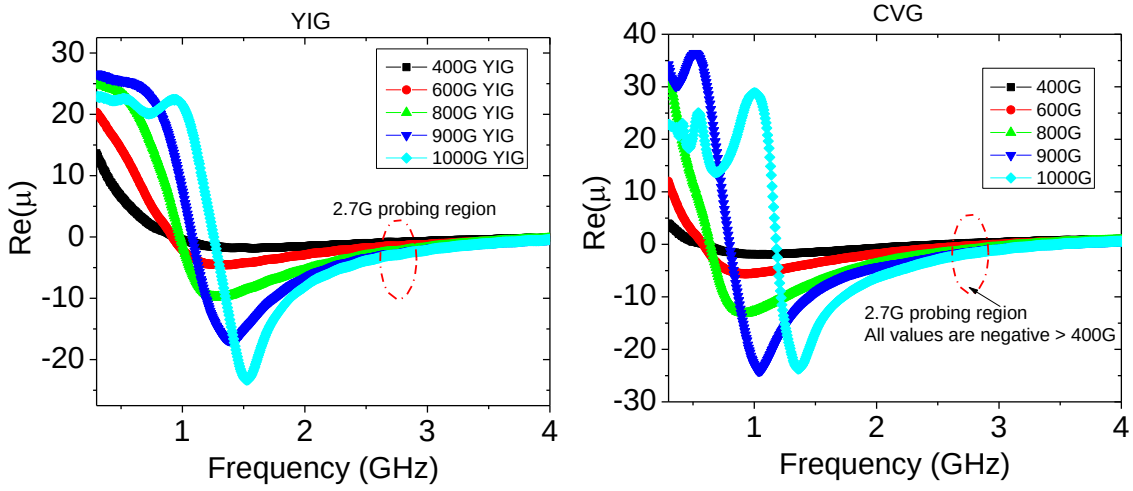

(a)

(b)

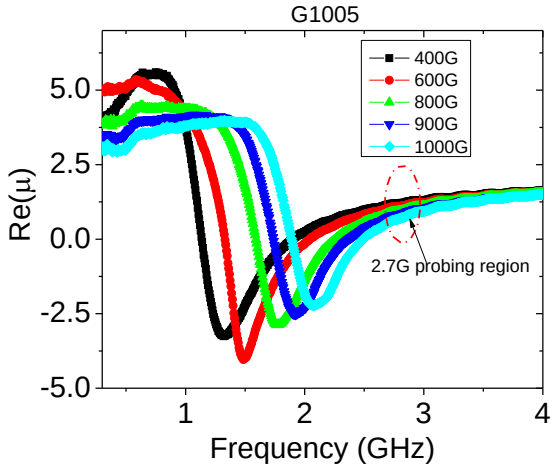

(c)

Figure 4.15: Characterized effective relative permeability in axial direction for selected materials. (a) Real relative permeability of YIG. (b) Real relative permeability of CVG. (d) Real relative permeability of GG.

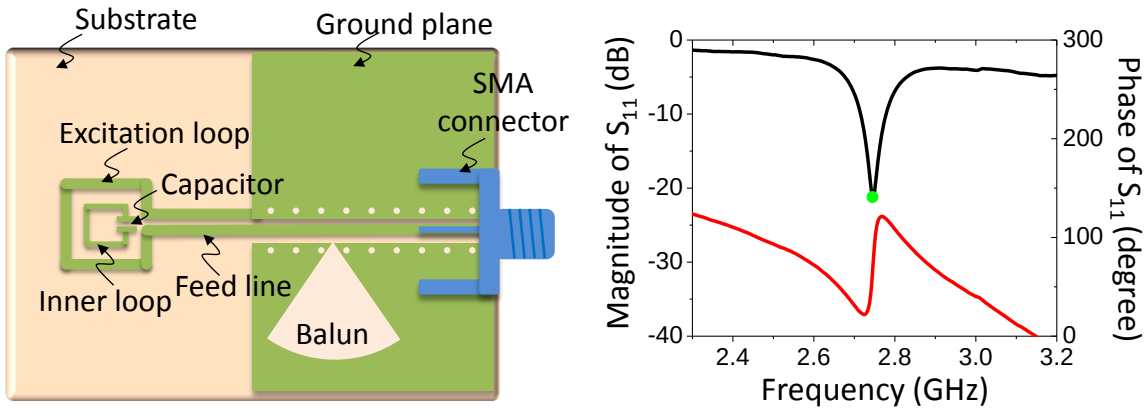

(a) (b)

Figure 4.16: Miniaturized probe design. (a) Probe layout. (b) Probe's S_{11}. The minimum magnitude labeled as solid circle is approximately -22 dB.

Figure 4.18 illustrates the change in magnitude of S_{11} before and after the magnetic bias is applied. As expected, without static magnetic bias field (Fig. 4.18(a)), the variation in $|S_{11}|$ is subtle due to positive permeability. However, with static magnetic bias (Fig. 4.18(b)), the predicted two resonance detection signature is observed due to the negative permeability provided by the bias field. The S_{11} indicating two resonances in Fig. 4.18(b) was obtained for YIG disk under bias of $977 o.e.$, and for CVG disk under $762 o.e.$. Under different magnetic bias, the open circuit points labeled as dash circle in Fig. 4.18(b) were moving the same trend as the simulated results. Within the capacity of the magnetic bias (up to $1200 o.e.$), material GG exhibits positive permeability within the monitoring bandwidth $2.6GHz$ to $2.9GHz$. Therefore, two resonance phenomenon is not observed throughout the bias tuning. The data of GG displayed in Fig. 4.18(b) is under bias field strength of $1100 o.e.$

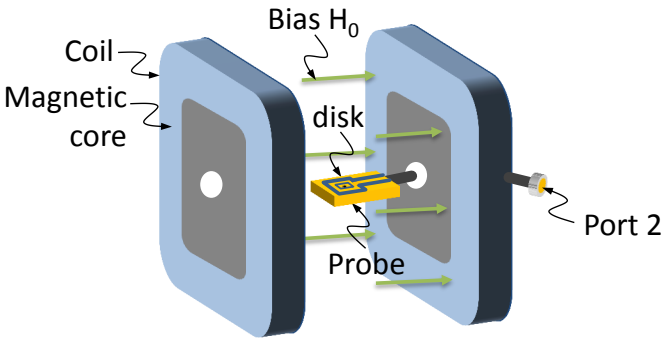

(a)

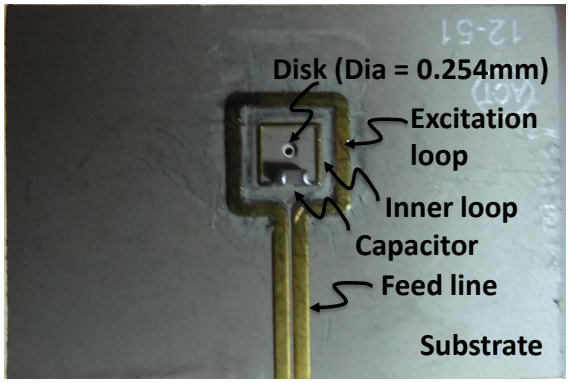

(b)

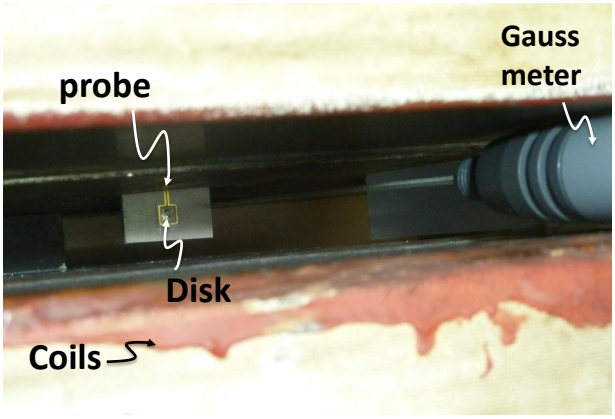

(c)

Figure 4.17: Detection of LMS resonant disk. (a) Schematic of experimental setup. (b) The close view of the probe with the disk sitting inside the hole. (c) Experimental configuration of LMSR detection.

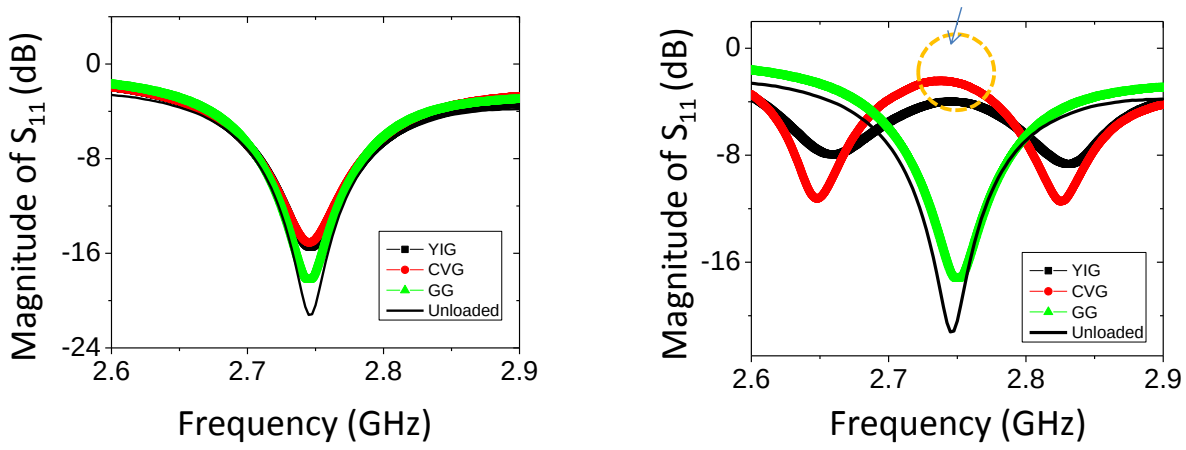

(a) (b)

Figure 4.18: Magnitude of S_{11} in dB. (a) Without static magnetic bias field. (b) With static magnetic bias field. The radius and the height of the disks is $0.127mm$. YIG disk is under bias of $977o.e.$, CVG is under bias of $762.o.e$, and GG is under bias of $1100o.e.$.

4.8 Discussion

This Chapter proposed detection of LMSR in electrically small particles at low microwave frequencies. The detection is based on a two loop resonator probe whose physical model can be explained by linear transformer theory. The two concentric inclusions are coupled by their mutual inductance that ensures effective energy transfer between these loops while being highly sensitive to magnetic energy variation in their close proximity. In presence of a low loss LMS resonant sphere, the simulated S_{11} of the probe exhibited two resonances. These two resonances can be used as a detection signature for sensing LMS resonant spheres without or with low magnetic loss. Such LMSR detection signature is not limited to spherical particles as long as non-spherical particles exhibit maximum magnetic polarizability in the detection direction normal to the loops' plane. This prediction was verified in numerical simulations where an LMS resonant disk was placed in the center of the probe.

Experimental results on ferrimagnetic disk having effective negative permeability in the direction of the alternating field also demonstrated the similar two resonance behavior in obtained S_{11}. The LMSR detection presented in this work could play an important role in marker based applications in biomedicine or bioengineering.

Chapter 5

Future work

5.1 LMS resonant marker sensing

As stated in this work, the occurrence of electrically small LMS resonant particle yields a strong magnetic polarizability in the direction of negative real permeability. This large magnetic polarizability on such electrically small resonant particle can be useful to control the movement of biological entities that labeled with these particle markers. This can be explained by the following equation that demonstrates the relationship of maximum forces on the particle, particle's magnetic polarizability, and external magnetic gradient. By using the identity $(B \cdot \nabla)B = \frac{1}{2}\nabla(B \cdot B) - B \times (\nabla \times B)$ in magnetostatic theory, this force is written as

$$F_m = (m \cdot \nabla)B = 4\pi\beta(H \cdot \nabla)B = 4\pi\beta\nabla(\frac{B \cdot B}{2\mu_0}) = 4\pi\beta\nabla(\frac{1}{2}B \cdot H) \tag{5.1}$$

where F_m is the force due to magnetic moment of the particle, m, which is determined by its magnetic polarizability β, $\nabla\frac{1}{2}B \cdot H$ represents the gradient of the magnetic field energy, and the surrounding biological medium is expected to have relative permeability of

μ_0. Eq. (5.1) suggests that maximum force can be achieved when the maximum magnetic polarizability of the particle accords with the applied magnetic field gradient. As a result, such force gives rise to translational action in direction of maximum force. Having given above theory, it is not difficult to conclude that if biological entities are labeled with LMS resonant markers, they can be separated from the ones without labeling by manipulating the external magnetic field. This conclusion can be also extended to the possibility of labeling multiple LMS resonant markers and control their movements using corresponding LMS resonant frequencies. Analogously, such theory can also be employed to drug delivery to ensure the effectiveness of drug treatment by localizing or immobilizing the drug carriers to target lesions. More interestingly, if LMS resonant markers are introduced in MRI environment, they would enhance the local inhomogeneity of pathological tissue and affect the relaxation time. Provided the potential promising applications of LMS resonant markers in biomedicine, it is not difficult to propose the sensing schemes for marker labeled biological entities. Such sensing can be done by using a magnetic probe placed close to target medium container. The targets with LMS resonant marker would quickly move to the destination at corresponding compellation frequency, whereas the ones without markers would stay stationary.

The proposed the potential applications of LMS resonant markers in biomedicine can be possibly extended to other applications as long as a target can be labeled by such particles. The mechanism and sensing scheme explained would have high impact on LMS resonant marker based applications in many interdisciplinary areas.

5.2 Near-field probe for LMS resonant marker assisted breast cancer detection

LMS resonant marker idea provides a new perspective for the breast cancer sensing topic. As mentioned in previous section, instead of the paramagnetic marker, one may use LMS resonant particle as a sensing agent, as the resonant one produces very strong magnetic field confinement at its resonance. Place such a sphere concentrically with an electrically small loop, the magnetic flux through the loop plane would be increased, leading to current alternations in the loop. The near-field coupling between the loop and the sphere can be also formulated by remedying the self-inductance variation of a single circular loop due to insertion of a concentrically placed magnetic sphere. Using the magnetic vector potential of a circular loop coaxial with an isotropic magnetic sphere demonstrated in Appendix C [134], I derived the new expression of self-inductance change in Eq. C.4. For electrically very small shapes, the variation of inductance can be approximated using the first term of the series in Eq. C.4 as follows.

$$\Delta L = \pi\mu_0 \frac{\mu_r - 1}{\mu_r + 2} \frac{b^3}{r_0^2 + a^2} \left[P_n^1 \left(\frac{r_0}{\sqrt{r_0^2 + a^2}} \right) \right]^2 \tag{5.2}$$

Interestingly, the new inductance change is also proportional to sphere's magnetic polarizability, yielding a similar singularity under magnetostatic condition ($\mu_r = -2$). Followed the approach presented in Chapter 3, a loop resonator probe can be designed accordingly at frequency of interest. Place such a loop probe close to the constructed breast phantom embedded with LMS marker labeled tumor, two resonances detection signature can be predicted and expected to have clearer identification when the tumor position lies in the axial direction of the detecting loop. This proposed future work would provide a new approach for sensing early stage breast cancer due to their small sizes under quasi-static approximation.

Chapter 6

Contributions

The construction of MNPs aims to provide subwavelength resolution to resolve the fine feature of the object. They are sensitive to variations in electromagnetic properties or/and morphologies of the sensing target. Most of the MNPs were designed to confine evanescent fields to openings or probing tips that are significantly smaller than the wavelength of the operation frequency, producing resolution much higher than the classical Abbé limit. These probes are subject to high precision variation control and low surface roughness. Highly durable probe with acceptable resolution would have promising future in microwave subsurface applications.

Inspired by state of the art advances, metamaterials and their proliferated applications, in microwave community, a new MNP composed of a single metamaterial element (i.e., an SRR) was proposed. The detection capability of this SRR probe was evaluated using loss controllable saline solutions. The permittivity of the solutions was characterized by open-ended coaxial line and compared with Klein and Swift's model. The Field spatial spectrum of the SRR probe was analyzed to demonstrate enhancement of evanescent wave after insertion of SRR element. For this particular experiment, a metallic cube of $\lambda/74$ was detected in saline solutions with loss tangent up to unity under an equivalent standoff

distance of $6.35mm$ acrylic and $1mm$ air. The SRR probe is also tested in biological environment (i.e., ground chicken). A metallic cube with size of $\lambda/39$ was detected with phase change of approximately 15° behind $2mm$ thick chicken layer.

The biological detection was extended to anatomically realistic breast tissue phantom using a one loop resonator probe loaded with lumped capacitors. The breast tissue phantom was constructed to provide anatomically accurate numerical breast model for studying accurate electromagnetic interactions between the probe and the human breast. Preliminary results were presented to demonstrate the concept of a resonant loop resonator in sensing a breast lesion of size $5mm$ and $10mm$ with appreciable phase variations.

To miniaturize the loop probe further down to millimeter size, lumped capacitor approach can be remedied to fine probe features to provide high field confinement for sensing electrically very small LMS resonant particles. Two loop resonator design was proposed along with its circuit model. In presence of an LMS resonant sphere concentric with the loops, the inductance variation of the loops due to the sphere were solved. A singularity point, designated as open circuit point, in probe S_{11} was predicted at LMSR ($\mu = -2$). The resulting two resonances in probe S_{11} was identified as LMSR detection signature, as non-resonant sphere ($\mu_r \neq$-2) was not able to yield significantly appreciable change. The predictions were validated with full-wave numerical simulations. Candidate materials with effective negative permeability were investigated and selected for experimental verification. Similar two resonance phenomenon was observed and in good agreement with the theory. The sensing methodology based on this detection signature can be extended to other LMS resonant geometries.

The proposed LMSR sensing methodology would have promising future in LMS resonant marker based applications in bioengineering or biomedicine. One associated theory based on maximum force produced by LMS resonant particles was proposed for cell separation application. The inhomogeneous susceptibility due to involvement of these LMS

resonant markers was proposed to provide more possible agents for enhanced imaging in MRI. A sensing theory based on detection of LMS resonant marker labeled lesion was proposed for early breast cancer detection. These proposed theoretical works and ideas would contribute to the future research on LMSR.

To summarize the contribution of this dissertation work, the following contributions were accomplished.

- A microwave near-field probe based on metamaterial single element (SRR probe) is proposed in this work.
- Spectrum analysis is developed to explain evanescent enhancement due to insertion of SRR element.
- The SRR probe is evaluated using loss controllable target media (saline solutions). Experimental resolutions are measured to demonstrate the enhancement predicted in spectrum analysis.
- The SRR sensing ability is extended to biological tissue such as ground chicken to prove its capacity in resolve a metallic abnormality in lossy biological context.
- The biological study is expanded to anatomically realistic numerical breast phantom to construct accurate interaction between electromangetic waves and human issue.
- A one loop resonator is developed to conduct tumor detection in numerical breast phantom. The phase of S_{11} demonstrates appreciable variations in presence of a tumorous lesion at different locations.
- To further miniaturize the probe and increase probe field confinement in small region, two loop resonator probe is proposed to detect electrically very small LMS resonant particles.

- The field confinement in sphere interior and scattered field enhancement in vicinity of an LMS resonant sphere is investigated and demonstrated in terms of field distributions.
- A circuit model of the two loop resonator probe is proposed and validated with full-wave simulation.
- The circuit model is improved for a spherical magnetic load by solving inductance change due to the load using magnetostatic boundary conditions at the sphere surface.
- A detection signature of two resonances is predicted theoretically, and a sensing methodology is proposed based on the predictions.
- The sensing methodology is verified with full-wave numerical simulations.
- Candidate materials with effective negative real permeability is investigated and selected to demonstrate LMSR phenomenon in electrically small disks.
- The selected bulk materials are characterized using coaxial airline. The small disk particles are tested with proposed two loop resonator probe. Two resonance detection signature is validated in experiments and in good agreement with proposed sensing theory.
- A theory based on maximum force produced at LMSR is proposed for cell separation in biomedical application for future research.
- A sensing theory based on LMS resonant marker labeled tumor is proposed for early breast cancer detection.

The proposed works in this dissertation and proposed ideas for future research would have great impact to many biomedical and biomedicine applications. Publications related to this dissertation work are listed as follows.

- Z. Ren, A. Kabiri, and O. M. Ramahi, "Detection of Localized Magnetostatic Surface Resonant Spheres," *submitted*.

- Z. Ren, A. Kabiri, and O. M. Ramahi, "A Probe for Detecting Magnetostatic Surface Resonant Spheres," in *Proc., the 2013 IEEE International Symposium on Antennas and Propagation and USNC-URSI National Radio Science Meeting*, Orlando, FL, U.S.A, July 2013.

- Z. Ren, A. Kabiri, and O. M. Ramahi, "Magetostatic Surface Resonance in Anisotropic Spherical and Ellipsoidal Shapes, accepted for presentation *in META13, the 4th International Conference on Metamaterials, Photonic Crystals and Plasmonics*, Sharjah, U. A. E., March 2013.

- Z. Ren and O. M. Ramahi, "Scattering from Spherical Particles with Negative Permeability," in *IEEE International Symposium on Antennas and Propagation*, Chicago, IL, U.S.A, July 2012.

- Z. Ren, M. S. Boybay, and O. M. Ramahi, "Near-Field Probes for Subsurface Detection Using Split-Ring Resonators," *IEEE Transactions on Microwave Theory and Techniques*, Vol. 59, No. 2, pp. 488-495, Feb. 2011.

- Z. Ren, M. S. Boybay, and O. M. Ramahi, "Near-Field Subsurface Detection using Metamaterial Inspired Probes, *Journal of Applied Physics A, Special Issue on Advances in Metamaterials and Photonics*, Vol. 103, No. 3, pp. 839-842, Jan. 2011.

- Z. Ren, M. S. Boybay, and O. M. Ramahi, "Metamaterial Inspired Probe for Noninvasive Nearfield Subsurface Sensing, *in Proc., 2010 IEEE International Symposium on Antennas and Propagation and CNC/USNC/URSI Radio Science Meeting*, Toronto, ON, Canada, July 2010.

APPENDICES

Appendix A

Full field solutions for scattering from magnetic spheres/coated spheres

Suppose that an x-polarized plane wave is incident on a homogeneous and isotropic sphere of radius a, as shown in Fig. A.1(a), or a coated sphere with inner radius a and outer radius b, as shown in Fig. A.1(b). Both particles are surrounded with certain media. The incident wave, $E_i = E_0 e^{ik_b z}$, can be expanded in an infinite series of vector spherical harmonics [56]. In this work, $+ik_b z$ represents wave propagating in the positive z direction. The notation M and N in (A.1)-(A.6) are the concise forms of spherical harmonics representing internal and scattered fields, E_1, E_2 and E_s, respectively.

$$E_1 = \sum_{n=1}^{\infty} E_n (c_n M_{o1n}^{(1)} - i d_n N_{e1n}^{(1)}) \tag{A.1}$$

$$H_1 = -\frac{k_1}{\omega_1} \sum_{n=1}^{\infty} E_n (d_n M_{e1n}^{(1)} + i c_n N_{o1n}^{(1)}) \tag{A.2}$$

$$E_2 = \sum_{n=1}^{\infty} E_n (f_n M_{o1n}^{(1)} - i g_n N_{e1n}^{(1)} + v_n M_{o1n}^{(2)} - i w_n N_{e1n}^{(2)}) \tag{A.3}$$

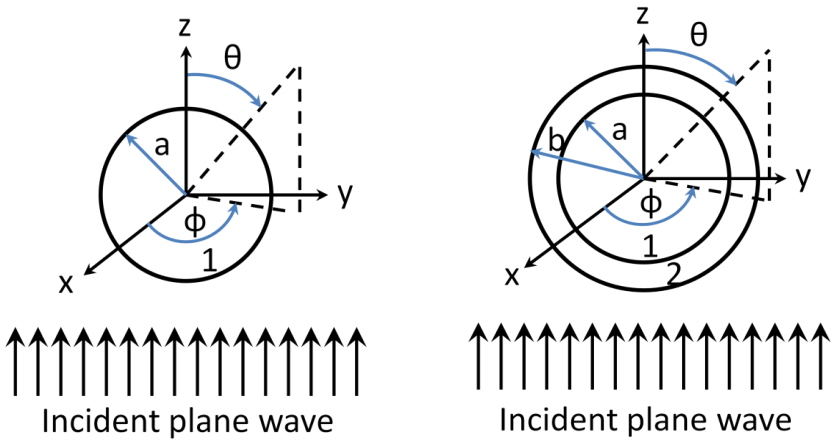

(a) (b)

Figure A.1: Spherical particle scattering. (a) Non-coated sphere. (b) Coated sphere. The scattering angle θ and ϕ are corresponding to vertical and horizontal angles.

$$H_2 = -\frac{k_2}{\omega\mu_2}\sum_{n=1}^{\infty} E_n(g_n M_{e1n}^{(1)} + if_n N_{o1n}^{(1)} + w_n M_{e1n}^{(2)} + iv_n N_{o1n}^{(2)}) \tag{A.4}$$

$$E_s = \sum_{n=1}^{\infty} E_n(ia_n N_{e1n}^{(3)} - b_n M_{o1n}^{(3)}) \tag{A.5}$$

$$H_s = \frac{k_b}{\omega\mu}\sum_{n=1}^{\infty} E_n(ib_n N_{o1n}^{(3)} + a_n M_{e1n}^{(3)}) \tag{A.6}$$

where $E_n = i^n E_0(2n+1)/[n(n+1)]$, k_b and μ_b are propagation constant and permeability of the surrounding medium, k and μ with subscripts 1 and 2 refer to values of inner core and coated layer, $M_{o,e1n}^{(1,2,3)}$ and $N_{o,e1n}^{(1,2,3)}$ are the vector spherical harmonics with the radical dependence of spherical Bessel function of the first kind (j_n), second kind (y_n), and spherical Hankel function of the first kind (h_n) in inner core, coated layer and surrounding medium labeled as superscripts 1, 2, and 3. Detailed expressions of the vector spherical harmonics are described in Ref. [56]. Applying the boundary condition $(E_2 - E_1)\times n = 0$ and $(H_2 - H_1)\times n = 0$ for non-coated sphere, the scattering and absorption coefficients can

$$a_n = \frac{-m_2\mu\psi_n'(y)[\psi_n(m_2y) - E_n^*\chi_n(m_2y)] + \mu_2\psi_n(y)[\psi_n'(m_2y) - E_n^*\chi_n'(m_2y)]}{-m_2\mu\xi_n'(y)[\psi_n(m_2y) - E_n^*\chi_n(m_2y)] + \mu_2\xi_n(y)[\psi_n'(m_2y) - E_n^*\chi_n'(m_2y)]} \tag{A.11}$$

$$b_n = \frac{m_2\mu\psi_n(y)[\psi_n'(m_2y) - F_n^*\chi_n'(m_2y)] - \mu_2\psi_n'(y)[\psi_n(m_2y) - F_n^*\chi_n(m_2y)]}{m_2\mu\xi_n(y)[\psi_n'(m_2y) - F_n^*\chi_n'(m_2y)] - \mu_2\xi_n'(y)[\psi_n(m_2y) - F_n^*\chi_n(m_2y)]} \tag{A.12}$$

---

then be expressed as

$$a_n = \frac{\mu_b m_1\psi_n(m_1x)\psi_n'(x) - \mu_1\psi_n(x)\psi_n'(m_1x)}{\mu_b m_1\psi_n(m_1x)\xi_n'(x) - \mu_1\xi_n(x)\psi_n'(m_1x)} \tag{A.7}$$

$$b_n = \frac{\mu_1\psi_n(m_1x)\psi_n'(x) - \mu_b m_1\psi_n(x)\psi_n'(m_1x)}{\mu_1\psi_n(m_1x)\xi_n'(x) - \mu_b m_1\xi_n(x)\psi_n'(m_1x)} \tag{A.8}$$

$$c_n = \frac{\mu_1 m_1 i}{\mu_1\psi_n(m_1x)\xi_n'(x) - \mu_b m_1\xi_n(x)\psi_n'(m_1x)} \tag{A.9}$$

$$d_n = \frac{\mu_1 m_1 i}{\mu_b m_1\psi_n(m_1x)\xi_n'(x) - \mu_1\xi_n(x)\psi_n'(m_1x)} \tag{A.10}$$

Applying the boundary condition $(E_s + E_i - E_2)\times n = 0$, and $(H_s + H_i - H_2)\times n = 0$ for the coated sphere, the scattering and absorption coefficients are expressed in (A.11)-(A.21).

$$E_n^* = \frac{m_1\mu_2\psi_n(m_1x)\psi_n'(m_2x) - m_2\mu_1\psi_n'(m_1x)\psi_n(m_2x)}{m_1\mu_2\psi_n(m_1x)\chi_n'(m_2x) - m_2\mu_1\psi_n'(m_1x)\chi_n(m_2x)} \tag{A.13}$$

$$F_n^* = \frac{m_1\mu_2\psi_n'(m_1x)\psi_n(m_2x) - m_2\mu_1\psi_n(m_1x)\psi_n'(m_2x)}{m_1\mu_2\psi_n'(m_1x)\chi_n(m_2x) - m_2\mu_1\psi_n(m_1x)\chi_n'(m_2x)} \tag{A.14}$$

$$D_n^* = \frac{m_1\psi_n'(m_2x) - m_2\psi_n'(m_1x)B_n^*}{m_1\chi_n'(m_2x)} \tag{A.15}$$

$$C_n^* = \frac{m_1\chi_n(m_2x) + m_2\psi_n(m_1x)A_n^*}{m_1\psi_n(m_2x)} \tag{A.16}$$

$$B_n^* = \frac{m_1\mu_1}{m_1\mu_2\psi_n(m_1x)\chi_n'(m_2x) - m_2\mu_1\psi_n'(m_1x)\chi_n(m_2x)} \tag{A.17}$$

$$A_n^* = \frac{m_1\mu_1}{m_2\mu_1\psi_n(m_1x)\psi_n'(m_2x) - m_1\mu_2\psi_n'(m_1x)\psi_n(m_2x)} \tag{A.18}$$

$$v_n = [\frac{\mu_2}{\mu_b}\psi_n(m_2y)\xi_n'(y) - m_2\xi_n(y)\psi_n'(m_2y)]b_n \\ -\frac{\mu_2}{\mu_b}m_2\psi_n'(y)\psi_n(m_2y) + \psi_n(y)\psi_n'(m_2y) \tag{A.19}$$

$$g_n = [m_2\chi_n(m_2y)\xi_n'(y) - \frac{\mu_2}{\mu_b}\xi_n(y)\chi_n'(m_2y)]a_n \\ +\frac{\mu_2}{\mu_b}\psi_n(y)\chi_n'(m_2y) - m_2\chi_n(m_2y)\psi_n'(y) \tag{A.20}$$

$$f_n = C_n^* v_n, w_n = D_n^* g_n, c_n = A_n^* v_n, d_n = B_n^* g_n \tag{A.21}$$

where $m_{1,2}$ is the refractive index, $x = k_b a$ and $y = k_b b$ are the size parameters, ψ_n, χ_n, and ξ_n are Riccati Bessel of the first kind, the second kind, and Ricatti Hankel function of the first kind, respectively. Superscript $'$ represent the corresponding derivative with respect to x or y.

To verify the formulations, simply setting equal permeabilities to all the layers, the same results can be obtained as those in Ref. [56]. The verification can be also confirmed by letting the properties of the coating the same as that of the core. The same results were obtained as previous non-coated sphere with the same permeability as the surrounding environment.

To analyze the possible requirements of magneto-static resonance that happens to spheres or coated spheres, the poles of the scattering coefficients or the coefficients of the internal wave were estimated, as at these poles the denominators of the coefficients can be very small. At the minina of the denominators, the wave can exhibit resonance [54]. From (A.7) and (A.8), using small argument approximation ($max\{m_1x, x\}$ is very small), the permeability dependence for magnetic resonance of a single sphere can be obtained as follows.

$$\mu_1 = -2\mu_b \tag{A.22}$$

Similarly, assuming $max\{m_1x, x, m_2y, y\}$ is very small, the permeability dependence for

magnetic resonance of a single sphere can be obtained as follows.

$$\mu_1 = \frac{2\mu_2[\beta^3(-2\mu_b - \mu_2) + (\mu_2 - \mu_b)]}{\beta^3(2\mu_b + \mu_2) + 2(\mu_2 - \mu_b)} \tag{A.23}$$

where $\beta = b/a$. This constraint provides three freedoms to manipulate and approaches to resonances. To successfully choose the values for resonances, One needs to ensure the arguments of Riccati functions are small enough as the resonances are very sensitive to these arguments.

Appendix B

LMSR conditions for isotropic ellipsoid or coated ellipsoid/anisotropic sphere or ellipsoid

LMSR conditions for electrically small isotropic/anisotropic ellipsoidal shapes and anisotropic spheres can be found from maximum magnetic polarizability using electrostatic theory due to EM duality [37, 56]. The shapes and their parameters are illustrated in Fig. B.1.

The LMSR condition electrically small isotropic ellipsoid shapes, which is permeability dependent, is expressed in B.1.

$$\mu_1 = \frac{L_i - 1}{L_i}\mu_b \tag{B.1}$$

where μ_b is the permeability of the surrounding medium, μ_1 represents the ellipsoid medium,

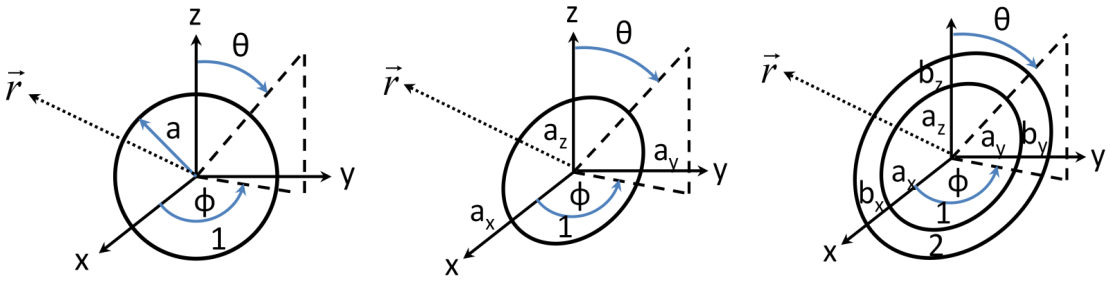

(a) (b) (c)

Figure B.1: Particle scattering. The definitions of scattering angle θ and ϕ are considered as the vertical and horizontal angles. Particle dimensions are denoted as a and b. The distance from observation point to origin is represented as vector $\vec{r}$. (a) Single sphere. (b) Single ellipsoid. (c) Coated ellipsoid.

and

$$L_i = \frac{a_x a_y a_z}{2} \int_0^\infty \frac{dq}{(a_i^2+q)\sqrt{(q+a_x^2)(q+a_y^2)(q+a_z^2)}} \tag{B.2}$$

where L_i is integrable function, subscript i represents x, y, and z direction, $Lx + Ly + Lz = 1$, $a_x \geq a_y \geq a_z$ are ellipsoid radius in x, y, z directions. Radius inequality yields $L_1 \leq L2 \leq L3$. Similarly, LMSR condition for coated ellipsoid can be also obtained as follows.

$$\mu_1 = \frac{\mu_2[\mu_b + (\mu_2 - \mu_b)L_i^{(2)}](L_i^{(1)} - fL_i^{(2)} - 1) + \mu_2^2 f L_i^{(2)}}{(L_i^{(1)} - fL_i^{(2)})[\mu_b + (\mu_2 - \mu_b)L_i^{(2)}] + fL_i^{(2)}\mu_2} \tag{B.3}$$

where

$$L_i^{(j)} = \frac{a_{jx} a_{jy} a_{jz}}{2} \int_0^\infty \frac{dq}{(a_{jz}^2+q)\sqrt{(q+a_{jx}^2)(q+a_{jy}^2)(q+a_{jz}^2)}} \tag{B.4}$$

$f = a_{1x}a_{1y}a_{1z}/(a_{2x}a_{2y}a_{2z})$ represents the ratio between the inner and outer volume, the superscript of L_i, $j = 1, 2$ refers to the inner and outer volume, and a_{ji} corresponds to the radius of the volume j in i direction.

Similarly, to sustain LMSR in anisotropic sphere and ellipsoid, Eq. (B.5) and Eq. (B.6) need to be satisfied.

$$\mu_{m,i} = -2\mu_b \tag{B.5}$$

where $i = x, y, z$ also indicates the direction of incidence, and m is the direction where the quasi-static approximation is applied. Eq. (B.5) is determined by the direction i of the applied magnetic field. From Eq. B.1, the LMSR condtion for anisotropic ellipsoid can be generalized in the following.

$$\mu_{m,i} = \frac{L_i - 1}{L_i}\mu_b \tag{B.6}$$

where L_i can be calculated using Eq. B.2.

Appendix C

Inductance variation due to presence of coaxially placed magnetic sphere

When the sphere is placed beyond the loop plane but still coaxial with the loop as seen in Fig. C.1. The self-inductance change due to presence of the magnetic sphere can be obtained by selecting the origin of the spherical coordinate at the center of the sphere. Assume the loop is located at $z = r_0$, the relative permeability of the sphere is μ_r, and the surrounding medium is vacuum. The magnetic vector potential due to the coaxial sphere is expressed as follows.

$$A_\phi + A_\phi^1 = \frac{\mu_0 I \sin\alpha}{2} \sum_{n=1}^{\infty} \left[\frac{1}{n(n+1)} \left(\frac{r}{a}\right)^n + A_n \left(\frac{b}{r}\right)^{n+1} \right] P_n^1(\cos\gamma) P_n^1(\cos\theta) \quad (b < r < a) \tag{C.1}$$

$$A_\phi + A_\phi^2 = \frac{\mu_0 I \sin\alpha}{2} \sum_{n=1}^{\infty} \left[\frac{1}{n(n+1)} \left(\frac{r}{a}\right)^n + B_n \left(\frac{r}{b}\right)^n \right] P_n^1(\cos\gamma) P_n^1(\cos\theta) \quad (r < b) \tag{C.2}$$

where

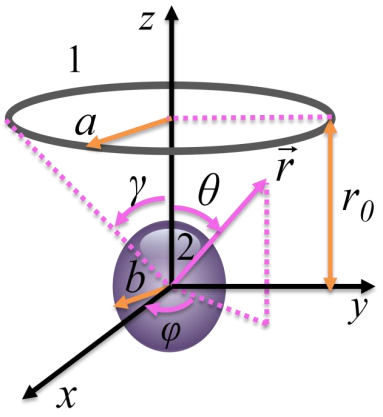

Figure C.1: Sphere coaxial with a circular loop. The radius of the sphere and the loop are b and a, respectively.

- A_ϕ : magnetic vector potential of circular loop at any point (r, θ, ϕ)
- A_ϕ^1 and A_ϕ^2 : magnetic vector potential of sphere at any point $(r > b, \theta, \phi)$ and $(r < b, \theta, \phi)$
- P_n^1 : legendre function of first order and degree n
- γ : describes the position where the circular loop is located. Since origin is at sphere center, $\cos\gamma = \frac{r_0}{\sqrt{r_0^2+a^2}}$
- a,b : radius of circular loop and sphere
- $\left(\frac{b}{r}\right)^{n+1}$ and $\left(\frac{r}{b}\right)^n$: term outside the sphere and term inside the sphere
- A_n and B_n : coefficients

From B.C I and II, the coefficients can be derived. The coefficient expressions are the same as Eq. 4.11. Hence, the increment of self-inductance due to the presence of the sphere

can be written as follows.

$$\Delta L = \frac{1}{I} 2\pi a A_{\phi}^{1} \Big|_{r=\sqrt{r_0^2+a^2}}^{\gamma=\theta=\frac{r_0}{\sqrt{r_0^2+a^2}}} \tag{C.3}$$

$$\Delta L = \pi\mu_0 \sum_{n=1}^{\infty} \frac{(\mu-1)}{n(n\mu+n+1)} \frac{b^{2n+1}}{a^{n-1}} \frac{\left[P_n^1(\frac{r_0}{\sqrt{r_0^2+a^2}})\right]^2}{(r_0^2+a^2)^{\frac{n+1}{2}}} \tag{C.4}$$

References

[1] L. Novotny, B. Hecht, and D. Pohl. Implications of high resolution to near-field optical microscopy. *Ultramicroscopy*, 71:341–343, 1998.

[2] S. M. Anlage, V. V. Talanov, and A. R. Schwartz. *Scanning Probe Microscopy*, volume 1, chapter Principles of Near-Field Microwave Microscopy. Springer, New York, 2007.

[3] Z. Frait. The use of high-frequency modulation in studying ferromagnetic resonance. *Czechosl. Journ. Phys.*, 3(9):403–404, 1959.

[4] R. F. Soohoo. A microwave magnetic microscope. *J. Appl. Phys. Suppl.*, 33(3):1276–1277, 1962.

[5] Björn T. Rosner and D. W. van der Weide. High-frequency near-field microscopy. *Rev. Sci. Instrum.*, 73(7):616, 2002.

[6] C. A. Bryant and J. B. Gunn. Noncontact technique of the local measurement of semiconductor resistivity. *Rev. Sci. Instrum.*, 36:1614–1617, 1965.

[7] E. A. Ash and G. Nicholls. Super-resolution aperture scanning microscope. *Nature*, 237:510–512, 1972.

[8] M. Fee, S. Chu, and T. W. Hänsch. Scanning electromagnetic transmission line microscope with sub-wavelength resolution. *Optics Comm.*, 3,4(69):449–452, 1989.

[9] T. Wei, X. D. Xianga, W. G. Wallace-Freedman, and P. G. Schultz. Scanning tip microwave near-field microscope. *Appl. Phys. Lett.*, 68(24):3506–3508, 1996.

[10] C. Gao, T. Wei, F. Duewer, Y. Lu, and X.-D. Xiang. High spatial resolution quantitative microwave impedance microscopy by a scanning tip microwave near-field microscope. *Appl. Phys. Lett.*, 71(12):1872–1874, 1997.

[11] M. Tabib-Azar, D. P. Su, A. Pohar, S.R. LeClair, and G. Ponchak. 0.4 μm spatial resolution with 1 ghz ($\lambda = 30cm$) evanescent microwave probe. *Rev. Sci. Instrum.*, 70(3):1725–1729, 1999.

[12] M. Tabib-Azar, J. L. Katz, and S. R. LeClair. Evanescent microwaves: a novel superresolution noncontact nondestructive imaging technique for biological applications. *IEEE. Trans. Instrum. Meas.*, 48(6):1111–1116, 1999.

[13] M. Tabib-Azar, P.S. Pathak, G. Ponchak, and S.R. LeClair.

[14] G. Q. Jiang, W. H. Wong, E. Y. Raskovich, and W. G. Clark. Open-ended coaxial-line technique for the measurement of the microwave dielectric constant for low-loss solids and liquids. *Rev. Sci. Instrum.*, 64(6):1614–1641, 1993.

[15] C. L. Pournaropoulos. *A study on the coaxial aperture electromagnetic sensor and its application in material characterization.* PhD thesis, University of Wisconsin, Milwaukee, Wisconsin, 1996.

[16] M. T. Ghasr, S. Kharkovsky, R. Zoughi, and R. Austin. Comparison of near-field millimeter-wave probes for detecting corrosion precursor pitting under paint. *IEEE. Trans. Instrum. Meas.*, 54(4):1497–1504, 2005.

[17] M. T. Ghasr, B. Carroll, S. Kharkovsky, R. Austin, and R. Zoughi. Millimeter-wave differential probe for nondestructive detection of corrosion precursor pitting. *IEEE. Trans. Instrum. Meas.*, 55(5):1620–1627, 2006.

[18] J. B. Pendry. Negative refraction makes a perfect lens. *Phys. Rev. lett.*, 85(18):3966–3969, 2000.

[19] D. R. Smith. Beating the diffraction limit. *Physics World*, 17(23):23–24, May 2004.

[20] N. Garcia and M. Nieto-Vesperinas. Left-handed materials do not make a perfect lens. *Phys. Rev. Lett.*, 88(20):207403, 2004.

[21] J. B. Pendry, D. Schurig, and D. R. Smith. Controlling electromagnetic fields. *Science*, 312:1780–1782, 2006.

[22] W. Cai, U. K. Chettiar, A. V. Kildishev, and V. M. Shalaev. Optical cloaking with metamaterials. *Nature Photonics*, 1:224–227, 2007.

[23] Engheta N. Circuits with light at nanoscales: Optical nanocircuits inspired by metamaterials. *Science*, 317:1698–1702, 2007.

[24] A. K. Sarychev, G. Shvets, and V. M. Shalaev. Magnetic plasmon resonance. *Phys. Rev. E*, 73:036609, 2006.

[25] V. G. Veselago. The electrodynamics of substances with simultaneously negative values of ϵ and μ. *Sov. Phys. Usp.*, 10(4):509–514, 1968.

[26] L.D. Landau and E.M. Lifshitz. *Electrodynamics of Continuous Media (Volume 8 of A Course of Theoretical Physics).* Pergamon Press, Pergamon, 1960.

[27] W. J. Padilla, D. N. Basov, and D. R. Smith. Negative refractive index metamaterials. *Materials Today*, 9:28–35, 2006.

[28] G. V. Eleftheriades, A. K. Iyer, and P. C. Kremer. Planar negative refractive index media using periodically lc loaded transmission lines. *IEEE Trans. Microw. Theory Techn.*, 50(12):2702–2712, 2002.

[29] N. Engheta, A. Alù, M. G. Silveirinha, A. Salandrino, and J. Li. Dng, sng, enz, and mnz metamaterials and their potential applications. In *IEEE MELECON*, pages 258–261, May 2006.

[30] B. M. Notaros. *Uniform Plane Electromagnetic Waves*. Prentice Hall, Boca Raton, 2011.

[31] P. A. M. Dirac. Quantised singularities in the electromagnetic field. *Proc. Roy. Soc.*, 133(60), 1931.

[32] W. J. Padilla, D. N. Basov, and D. R. Smith. Composite medium with simultaneously negative permeability and permittivity. *Phys. Rev. Lett.*, 84:4184–4187, 2000.

[33] J. Woodley and M. Mojahedi. On the signs of the imaginary parts of the effective permittivity and permeability in metamaterials. *J. Opt. Soc. Am. B*, 27(5):1016–1021, 2010.

[34] J. B. Pendry, A. J. Holden, D. J. Robbins, and W. J. Stewart. Magnetism from conductors and enhanced nonlinear phenomena. *IEEE Trans. Microwave Theory Tech.*, 47(11):2075–2084, 1999.

[35] A. Kabiri, O. M. Ramahi, and Larbi Talbi. Modeling of the magnetostatic resonances in small-size metamaterials. In *ICMAT11*, June 2011.

[36] A. Kabiri, L. Talbi, and O. M. Ramahi. Modeling of magnetostatic resonances in small-size metamaterials. *Appl. Phys. A*, (107):145–148, 2012.

[37] Y. Urzhumov, W. Chen, C. Bingham, W. Padilla, and D. R. Smith1. Magnetic levitation of metamaterial bodies enhanced with magnetostatic surface resonances. *Phys. Rev. B*, 85:054430, 2012.

[38] A. Boardman. Pioneers in metamaterials: John pendry and victor veselago. *J. Opt.*, 13(2):020401, 2011.

[39] J. Pendry. New electromagnetic materials emphasize the negative. *Phys. World*, pages 1–5, 2001.

[40] L. Yousefi and O. M. Ramahi. Artificial magnetic materialsusing fractal hilbert curves. *IEEE Trans. Ant. Prop.*, 58:2614 – 2622, 2010.

[41] L. Yousefi and O. M. Ramahi. New artificial magnetic materials based on fractal hilbert curves. In *IWAT07.*, pages 237–240, March 2007.

[42] A. Kabiri and O. M. Ramahi. nth order rose curve as a generic candidate for rf artificial magnetic material. *J. Appl. Phys. A.*, 103(3):831–834, 2011.

[43] F. Falcone, T. Lopetegi, J. D. Baena, R. Marques, F. Martin, and M. Sorolla. Effective negative-ϵ stopband microstrip lines based on complementary split ring resonators. *IEEE Microw. Wireless. Compon. Lett.*, 14:280–282, 2004.

[44] F. Falcone, T. Lopetegi, M. A. G. Laso, J. D. Baena, J. Bonache, M. Beruete, R. Marqués, F. Martín, and M. Sorolla. Babinet principle applied to the design of metasurfaces and metamaterials. *Phys. Rev. Lett.*, 93(19):197401, 2004.

[45] R. Marqués, J. Martel, F. Mesa, , and F. Medina. Left-handed-media simulation and transmission of em waves in subwavelength split-ring-resonator-loaded metallic waveguides. *Phys. Rev. Lett.*, 89:183901, 2002.

[46] Aycan Erentok, Richard W. Ziolkowski, J. A. Nielsen, R. B. Greegor, C. G. Parazzoli, M. H. Tanielian, Steven A. Cummer, Bogdan-Ioan Popa, Thomas Hand, D. C. Vier, and S. Schultz. Low frequency lumped element-based negative index metamaterial. *Appl. Phys. Lett.*, 91:184104, November 2007.

[47] H. Němec, C. Kadlec, F. Kadlec, P. Kužel, R. Yahiaoui, U.-C. Chung, C. Elissalde, M. Maglione, and P. Mounaix. Resonant magnetic response of tio2 microspheres at terahertz frequencies. *Appl. Phys. Lett.*, 100:061117, 2012.

[48] F. Capolino, editor. *Self-Assembly and Nanochemistry Techniques for the Fabrication of Metamaterials*. CRC Press, Boca Raton, 2009.

[49] J. Valentine, S. Zhang, T. Zentgraf, E. Ulin-Avila, D. A. Genov, G. Bartal, and X. Zhang. Three-dimensional optical metamaterial with a negative refractive index. *Nature*, 455(7211):376–379, 2008.

[50] A. Alù, A. Salandrino, and N. Engheta. Negative effective permeability and left-handed materials at optical frequencies. *Opt. Express*, 14(4):1557–1567, 2006.

[51] David R. Smith, David Schurig, Marshall Rosenbluth, and Sheldon Schultz. Limitations on subdiffraction imaging with a negative refractive index slab. *Appl. Phys. Lett.*, 82(10):1506–1508, 2003.

[52] M. S. Boybay and O. M. Ramahi. Near-field probes using double and single negative media. *Phys. Rev. E*, 79(1):016602, 2009.

[53] M. S. Boybay and O. M. Ramahi. Experimental and numerical study of sensitivity improvement in near-field probes using single-negative media. *IEEE Trans. Microw. Theory Tech.*, 57(12):3427–3433, 2009.

[54] Michael Quinten. *Optical Properties of Nanoparticle systems: Mie and Beyond*. Wiley-VCH, 2011.

[55] Y. Chen and R. P. Lipton. Resonance and double negative behavior in metamaterials. *Arch. Rational Mech. Anal.*, 2013.

[56] C. F. Bohren and D. R. Huffman. *Absorption and Scattering of Light by Small Particles*. Wiley, 1983.

[57] H. Fröhlich. *Theory of Dielectrics:Dielectric Constant and Dielectric Loss*. Clarendon Press, Oxford, 1949.

[58] R. H. Ritchie. Plasma losses by fast electrons in thin films. *Phys. Rev.*, 106(5):874, 1957.

[59] K. N. Rozanova, Z. W. Li, L. F. Chen, and M. Y. Koledintseva. Microwave permeability of co_2z composites. *J. Appl. Phys.*, 97:013905, 2005.

[60] S. L. Oliveira and S. C. Rand. Intense nonlinear magnetic dipole radiation at optical frequencies: Molecular scattering in a dielectric liquid. *Phys. Rev. Lett.*, 98:093901, 2007.

[61] S. C. Rand, W. M. Fisher, and S. L. Oliveira. Optically induced magnetization in homogeneous,undoped dielectric media. *J. Opt. Soc. Am. B*, 25(7):1106–1117, 2008.

[62] Hongjie Zhao, Ji Zhou, Qian Zhao, Bo Li, and Lei Kang. Magnetotunable left-handed material consisting of yttrium iron garnet slab and metallic wires. *Appl. Phys. Lett.*, 91:131107, 2007.

[63] Takanori Tsutaoka, Teruhiro Kasagi, and Kenichi Hatakeyama. Permeability spectra of yttrium iron garnet and its granular composite materials under dc magnetic field. *J. Appl. Phys.*, 110:053909, 2011.

[64] B. Yang, R. S. Donnan, R. Dubrovka, and W. Tang. Negative permeability characterization of gyrotropic hexaferrite in the millimeter wave band for engineering of double-negative devices. *J. Appl. Phys.*, 109:104505, 2011.

[65] V. G. Harris, A. Geiler, Y. Chen, S. D. Yoon, M. Wu, A. Yang, Z. Chen, P. He, P. V. Parimi, X. Zuo, C. E. Patton, M. Abe, O. Acher, and C. Vittoria. Recent advances in processing and applications of microwave ferrites. *J. Magn. Magn. Mater.*, 321:2035–2047, 2009.

[66] K. Buell, H. Mosallaei, and K. Sarabandi. A substrate for small patch antennas providing tunable miniaturization factors. *IEEE Trans. Microw. Theory Tech.*, 54(1):135–146, 2006.

[67] N. Matsushita, C. P. Chong, T. Mizutani, and M. Abe. Ni-zn ferrite films with high permeability ($\mu' = 30$, $\mu'' = 30$) at 1 ghz prepared at 90°c. *J. Appl. Phys.*, 91(10):7376–7378, 2002.

[68] G. Dewar. A thin wire array and magnetic host structure with n ¡ 0. *J. Appl. Phys.*, 97:10Q101, 2005.

[69] S. T. Chui and Liangbin Hu. Theoretical investigation on the possibility of preparing left-handed materials in metallic magnetic granular composites. *Phys. Rev. B*, 65:144407, Mar 2002.

[70] J. Chen, B. Zhang, D. Tang, Y. Yang, W. Xu, and H. Lu. Possible existence of a new type of left-handed materials in coupled ferromagnetic bilayer films. *J. Magn. Magn. Mater.*, 302:368–374, 2006.

[71] R. V. Mikhaylovskiy, E. Hendry, and V. V. Kruglyak. Negative permeability due to exchange spin-wave resonances in thin magnetic films with surface pinning. *Phys. Rev. B*, 82:195446, 2010.

[72] J. H. E. Griffiths. Anomalous high-frequency resistance of ferromagnetic metals. *Nature*, 158:670–671, 1946.

[73] Charles Kittel. On the theory of ferromagnetic resonance absorption. *Phys. Rev.*, 73:155161, 1948.

[74] A. G. Gurevich and Gennadii A. Melkov. *Magnetization Oscillations and Waves*. CRC Press, New York, 1996.

[75] L. R. Walker. Magnetostatic modes in ferromagnetic resonance. *Phys. Rev.*, 105(2):390–399, 1957.

[76] J. F. Dillon and Jr. Magnetostatic modes in ferrimagnetic spheres. *Phys. Rev.*, 112(1):59–63, 1958.

[77] P. C. Fletcher and R. O. Bell. Ferrimagnetic resonance modes in spheres. *J. Appl. Phys.*, 30(5):687–698, 1959.

[78] J. R. Eshbach and R. W. Damon. Surface magnetostatic modes and surface spin waves. *Phys. Rev.*, 118:12081210, 1960.

[79] J. F. Dillon. Magnetostatic modes in disks and rods. *J. Appl. Phys.*, 31(9):1605–1614, 1960.

[80] E. O. Kamenetskii. Handedness of magnetic-dipolar modes in ferrite disks. *J. Magn. Magn. Mater.*, 302:137–155, 2005.

[81] E. O. Kamenetskii. Helical-mode magnetostatic resonances in small ferrite particles and singular metamaterials. *J. Phys.: Condens. Matter*, 22(48):486005, 2010.

[82] Z. Frait, V. Kambersky, Z. Malek, and M. Ondris. Local variations of uniaxial anisotropy in thin films. *Czeck. J. Phys. B*, 10(8):616–617, 1960.

[83] M. Tabib-Azar, N. S. Shoemaker, and S. Harris. Non-destructive characterization of materials by evanescent microwaves. *Meas. Sci. Technol.*, 4(5):583–590, 1993.

[84] M. S. Boybay and O. Ramahi. Experimental verification of sensitivity improvement in near field probes using single negative metamaterials. In *IEEE MTTS Int. Symp. Dig.*, pages 1677–1680, Jun 2009.

[85] L. Yousefi. *Theory, Design and Development of Artificial Magnetic Materials*. PhD thesis, University of Waterloo, Waterloo,Canada, September 2009.

[86] Z. Ren, M. S. Boybay, and O. M. Ramahi. Near-field probes for sub-surface detection using split-ring resonators. *IEEE Trans. Microw. Theory Techn.*, 59(2):488, 2011.

[87] L. Zhang, J.G. Lyng, N. Brunton, D. Morgan, and B. McKenna. Dielectric and thermophysical properties of meat batters over a temperature range of 5-85°c. *Meat Science*, 68(2):173–184, 2004.

[88] L. V. Wang, Xuemei Zhao, Haitao Sun, and Geng Ku. Microwave-induced acoustic imaging of biological tissues. *Rev. Sci. Instrum.*, 70(9):3744–3748, 1999.

[89] R. Marqués, F. Medina, and R. Rafii-El-Idrissi. Role of bianisotropy in negative permeability and left-handed metamaterials. *Phys. Rev. B*, 65(144440):1–6, 2001.

[90] G. Bindu and K. T. Mathew. Characterization of benign and malignant breast tissues using 2-d microwave tomographic imaging. *Microw. Opt. Technol. Lett.*, 49(10):2341–2345, 2007.

[91] L. Robledo, M. Carrasco, and D. Merya. A survey of land mine detection technology. *Int. J. Remote Sens.*, 30(9):2399–2410, 2009.

[92] Y. J. Kim. *Development of electromagnetic imaging technology for damage detection*. PhD thesis, University of california, Irvine,U.S., 2002.

[93] L. A. Klein and C. T. Swift. An improved model for the dielectric constant of sea water at microwave frequencies. *IEEE. Trans. Ant. Prop*, 25(1):104–111, 1977.

[94] David M. Pozar. *Microwave Engineering*. John Wiley and Sons, 2007.

[95] D. E. Steinhauer, C. P. Vlahacos, S. K. Dutta, F. C. Wellstood, and Steven M. Anlage. Surface resistance imaging with a scanning near-field microwave microscope. *Appl. Phys. Lett.*, 71(12):1736–1738, 1997.

[96] William C. Fitzgerald, Michael N. Davis, James L. Blackshire, John F. Maguire, and David B. Mast. Evanescent microwave sensor scanning for detection of sub-coating corrosion. *J. Corrosion Sci. Eng.*, 3:15–22, 2002.

[97] A. Kraszewski and M. A. Stuchly. Ana calibration method for measurement of dielectric properties. *IEEE. Trans. Instrum. Meas.*, 32(2):385–387, 1983.

[98] D. K. Misra and D. Eungdamrong. Coaxial aperture electrical sensor and its application : A tutorial overview. In *Circuits and Systems ISCAS, 2001*, volume 2, pages 449–452, May 2001.

[99] American Cancer Society. Cancer facts and figures 2010. *Atlanta: American Cancer Society*, 2010.

[100] American Cancer Society. Breast cancer facts & figures 2009-2010. *Atlanta: American Cancer Society*, 2010.

[101] R. A. Smith, D. Saslow, K. A. Sawyer, W. Burke, M. E. Costanza, W. P. Evans, R. S. Foster, E. Hendrick, H. J. Eyre, and S. Sener. American cancer society guidelines for breast cancer screening: Update 2003. *CA Cancer J. Clin.*, 53:141–169, 2003.

[102] L. Brooks and M. Morley. Mammography may increase breast cancer risk in some high-risk women. *RSNA News*, Dec 2009.

[103] F. Delbary, M. Brignone, G. Bozza, R. Aramini, and M. Piana. Microwave tomography: review of the progress towards clinical applications. *Phil. Trans. R. Soc. A*, 367(1900):3021–3042, 2009.

[104] E. J. Bond, X. Li, S. C. Hagness, and B. D. Van Veen. Microwave imaging via space-time beamforming for early detection of breast cancer. *IEEE Trans. Ant. Prop.*, 51(8):1690– 1705, 2003.

[105] M. Elsdon, M. Leach, S. Skobelev, and D. Smith. In *2007 International Symposium on Microwave, Antenna, Propagation and EMC Technologies for Wireless Communications*, pages 966–969.

[106] E. Zastrow, S. K. Davis, and S. C. Hagness. Safety assessment of breast cancer detection via ultrawideband microwave radar operating in pulsed-radiation mode. *Microw. Opt. Technol. Lett.*, 49(1):221–225, 2007.

[107] D. W. Winters, E. J. Bond, B. D. Van Veen, and S. C. Hagness. Estimation of the frequency-dependent average dielectric properties of breast tissue using a time-domain inverse scattering technique. *IEEE Trans. Ant. Prop.*, 54(11):3517 – 3528, 2009.

[108] F. Delbary, M. Brignone, G. Bozza, R. Aramini, and M. Piana. A visualization method for breast cancer detection using microwaves. *SIAM J. Appl. Math.*, 70(7):2509–2533, 2010.

[109] Y. Guo, H. W. Ko, and D. M. White. 3-d localization of buried objects by nearfield electromagnetic holography. *Geophysics*, 63(3):880–889, 1998.

[110] M. S. Zhdanov, P. Traynin, and J. Booker. Underground imaging by frequency domain electromagnetic migration. *Geophysics*, 61(3):666–682, 1996.

[111] E. C. Fear, X. Li, S. C. Hagness, and M. A. Stuchly. Confocal microwave imaging for breast cancer detection: localization of tumors in three dimensions. *IEEE Trans. Biomed. Eng.*, 49:812–822, 2002.

[112] J. M. Sill and E. C. Fear. Tissue sensing adaptive radar for breast cancer detection-experimental investigation of simple tumor models. *IEEE Trans. Microw. Theory Tech.*, 53(11):3312–3319, 2005.

[113] E. C. Fear, J. M. Sill, and M. A. Stuchly. Experimental feasibility study of confocal microwave imaging for breast tumor detection. *IEEE Trans. Microw. Theory Tech.*, 51(3):887– 892, 2003.

[114] M. Cheney, D. Isaacson, and J. C. Newell. Electrical impedance tomography. *SIAM Rev.*, 41(1):85–101, 1999.

[115] E. S. Day, J. G. Morton, and J. L. West. Nanoparticles for thermal cancer therapy. *J. Biomech. Eng.*, 074001(131):1–5, 2009.

[116] S. K. Davis, H. Tandradinata, S. C. Hagness, and B. D. Van Veen. Ultrawideband microwave breast cancer detection: a detection-theoretic approach using the generalized likelihood ratio test. *IEEE Trans. Biomed. Eng.*, 52(7):1237–1250, 2005.

[117] E. Zastrow, S. K. Davis, M. Lazebnik, F. Kelcz, B. D. Van Veen, and S. C. Hagness. Development of anatomically realistic numerical breast phantoms with accurate dielectric properties for modeling microwave interactions with the human breast. *IEEE Trans. Biomed. Eng.*, 55(12):2792–2800, 2007.

[118] A. Sabouni, S. Noghanian, and S. Pistorius. Effects of tissue composition on the accuracy of microwave breasttumour imaging. In R. Magjarevic and J. H. Nagel, editors, *World Congress on Medical Physics and Biomedical Engineering 2006*, volume 14 of *IFMBE Proceedings*, pages 1489–1493. Springer Berlin Heidelberg, 2007.

[119] A. Hassan, I. Elabyed, J. Mallow, T. Herrmann, J. Bernarding, and A. Omar. Optimal geometry and capacitors distribution of 7t mri surface coils. In *EuMC 2010, European Microwave Conference*, pages 1437 –1440, Sep 2010.

[120] P. Gonord, S. Kan, and A. Leroy-Willig. Parallel-plate split-conductor surface coil: Analysis and design. *Magn. Reson. Med.*, 6:353–358, 1988.

[121] J. Ugelstad, W. S. Prestvik, P. Stenstad andL. Kilaas., and G. Kvalheim. *Magnetism in Medicine*. Wiley-VCH, Berlin, 1998.

[122] K. K. Kim and D. W. Pack. *Microspheres for Drug Delivery*, pages 19–50. Springer, Berlin, 2006.

[123] M. Browne and R. C. Semelka. Wiley, New York, 1999.

[124] Q. A. Pankhurst, J. Connolly, S. K. Jones, and J. Dobson. Applications of magnetic nanoparticles in biomedicine. *J. Phys. D: Appl. Phys.*, 36:R167–R181, 2003.

[125] R. Hergt, S. Dutz, R. Müller, and M. Zeisberger. Magnetic particle hyperthermia: nanoparticle magnetism and materials development for cancer therapy. *J. Phys.: Condens. Matter*, 18:S2919–S2934, 2006.

[126] P. W. Anderson and J. M. Rowell. Probable observation of the josephson superconducting tunneling effect. *Phys. Rev. Lett.*, 10:230–232, 1963.

[127] J. Clarke and A. I. Braginski. *The SQUID Handbook: Fundamentals and Technology of SQUIDs and SQUID Systems*. Wiley-VCH, Weinheim, 1 edition, 2004.

[128] R. C. Jaklevic, John Lambe, A. H. Silver, and J. E. Mercereau. Quantum interference effects in josephson tunneling. *Phys. Rev. Lett.*, 12:159, 1964.

[129] Michael J. Caruso, Carl H. Smith, Tamara Bratland, and Robert Schneider. A new perspective on magnetic field sensing, 1998.

[130] Edward Ramsden. *Hall-Effect Sensors: Theory and Application.* Elsevier, New York, 2 edition, 2006.

[131] P. P. Freitas, R. Ferreira, S. Cardoso, and F. Cardoso. Magnetoresistive sensors. *J. Phys.: Condens. Matter*, 19(16):165221, 2007.

[132] M. Mück and C. Heiden. Planar microwave biased rf-squids in niobium technology. *Appl. Phys. A*, 54:475, 1992.

[133] F. Primdahl, O.V. Nielsen, J.R. Petersen, and P. Ripka. High frequency fluxgate sensor noise. *Electron. Lett.*, 30(6):481, 1994.

[134] W. R. Smythe. *Static and Dynamic Electricity.* McGraw-Hill, New York, 1968.

[135] A. Pimenov, A. Loidl, P. Przyslupski, and B. Dabrowski. Negative refraction in ferromagnet-superconductor superlattices. *Phys. Rev. Lett.*, 95:247009, 2005.

[136] A.M. Nicolson and G.F. Ross. Measurement of the intrinsic properties of materials by time domain techniques. *IEEE Trans. Instrum. Meas.*, 19:377–382, 1970.